

SYNTHESIS OF BORON AND ZIRCONIUM CO-DOPED TITANIUM
DIOXIDE NANOPOWDERS BY SOL-GEL TECHNIQUE

A THESIS SUBMITTED TO
THE GRADUATE SCHOOL OF NATURAL AND APPLIED SCIENCES
OF
MIDDLE EAST TECHNICAL UNIVERSITY

BY

LÜTFİ AĞARTAN

IN PARTIAL FULLFILLMENT OF THE REQUIREMENTS
FOR
THE DEGREE OF MASTER OF SCIENCE
IN
METALLURGICAL AND MATERIALS ENGINEERING

JUNE 2014

Approval of the thesis:

**SYNTHESIS OF BORON AND ZIRCONIUM CO-DOPED TITANIA
NANOPOWDERS BY SOL-GEL TECHNIQUE**

submitted by **LÜTFİ AĞARTAN** in partial fulfillment of the requirements for
the degree of **Master of Science in Metallurgical and Materials Engineering**
Department, Middle East Technical University by,

Prof. Dr. Canan Özgen _____
Dean, Graduate School of **Natural and Applied Sciences**

Prof. Dr. Cemil Hakan Gür _____
Head of Department, **Metallurgical and Materials Engineering**

Prof. Dr. Abdullah Öztürk _____
Supervisor, **Metallurgical and Materials Eng. Dept., METU**

Assoc. Prof. Dr. Jongee Park _____
Co-Supervisor, **Metallurgical and Materials Eng. Dept., Atılım University**

Examining Committee Members:

Prof. Dr. Macit Özenbaş _____
Metallurgical and Materials Engineering Dept., METU

Prof. Dr. Abdullah Öztürk _____
Metallurgical and Materials Engineering Dept., METU

Assoc. Prof. Dr. Jongee Park _____
Metallurgical and Materials Engineering Dept., Atılım University

Assoc. Prof. Dr. Caner Durucan _____
Metallurgical and Materials Engineering Dept., METU

Assist. Prof. Dr. Yunus Eren Kalay _____
Metallurgical and Materials Engineering Dept., METU

Date:

I hereby declare that all information in this document has been obtained and presented in accordance with academic rules and ethical conduct. I also declare that, as required by these rules and conduct, I have fully cited and referenced all material and results that are not original to this work.

Name, Last Name : Lütfi Ağartan

Signature :

ABSTRACT

SYNTHESIS OF BORON AND ZIRCONIUM CO-DOPED TITANIUM DIOXIDE NANOPOWDERS BY THE SOL-GEL TECHNIQUE

AĞARTAN, Lütfi

M.Sc., Department of Metallurgical and Materials Engineering

Supervisor: Prof. Dr. Abdullah ÖZTÜRK

Co-Supervisor: Assoc. Prof. Dr. Jongee PARK

June 2014, 181 pages

Effects of water/Ti precursor molar ratio (R ratio) and calcination regime on the photocatalytic properties of undoped, boron (B) doped, zirconium (Zr) doped, and B and Zr co-doped TiO₂ powders synthesized by sol-gel process were researched. Undoped powders were synthesized for R ratio of 1, 3, 5, 10, 30, and 50 while doped and co-doped powders were synthesized for R ratio of 50. Undoped powders were calcined at 300, 400, and 500°C for 1, 2, and 3 h while doped and co-doped powders were calcined at 300 and 500°C for 1 h. X-ray diffraction analysis indicated that doped and undoped powders composed of only anatase crystals, except the undoped powders synthesized for low R ratio calcined at 500°C. Rietveld analyses suggested that B and Zr were successfully doped into the crystal structure of TiO₂ and changed the lattice parameters. Scanning electron microscopy investigations revealed that all powders were in the range of 15 to 40 nm in size and were highly agglomerated. Diffuse

reflectance spectroscopy measurements showed that all powders had band gap energy of around 3.2 eV and their reflectance could be shifted to visible light region of the electromagnetic spectrum. Upon B and Zr co-doping better methylene blue degradation was achieved in UV light and daylight. The improvement in photocatalytic performance due to co-doping was attributed to the changes in structural and morphological features.

Keywords: Synthesis, boron, zirconium, TiO₂, sol-gel, nanopowder, photocatalysis.

ÖZ

BOR VE ZİRKONYUM KATKILANMIŞ TİTANYUM DİOKSİT NANOTOZLARIN SOL-JEL TEKNİĞİYLE SENTEZİ

AĞARTAN, Lütfi

Yüksek Lisans, Metalurji ve Malzeme Mühendisliği Bölümü

Tez Yöneticisi: Prof. Dr. Abdullah ÖZTÜRK

Ortak Tez Yöneticisi: Doç. Dr. Jongee PARK

Haziran 2014, 181 sayfa

Su/Ti prekürsör mol oranı (R oranı) ve kalsinasyon koşullarının sol-jel tekniğiyle sentezlenmiş katkısız, bor (B) katkılı, zirkonyum (Zr) katkılı, ve B ve Zr çift-katkılı TiO_2 tozlarının fotokatalitik özelliklere etkisi araştırıldı. Katkısız tozlar R oranı 1, 3, 5, 10, 30, ve 50; katkılı ve çift-katkılı tozlar ise R oranı 50 olarak sentezlendi. Katkısız tozlar 300, 400, ve 500°C de 1, 2, ve 3 saat, katkılı ve çift-katkılı tozlar ise 300 ve 500°C de 1 saat kalsine edildi. X-ışını kırınımı analizleri düşük R değeri ve 500°C kalsine edilerek sentezlenmiş katkısız tozlar haricindeki katkısız ve katkılı tozların sadece anataz kristallerinden oluştuğunu gösterdi. Rietveld analizleri B ve Zr' un TiO_2 kristal yapısına başarıyla katkılındığını ve latis parametrelerini değiştirdiğini önerdi. Taramalı elektron mikroskop çalışmaları bütün tozların partikül boyutlarının 15 ile 40 nm arasında değiştiğini ve oldukça topaklanmış olduklarını açığa çıkardı. Difüze reflektör spektroskopisi ölçümleri bütün tozların enerji kuşak aralığının 3.2 eV civarında

olduđunu ve emilimin elektromanyetik spektrumun grnr ışık kısmına dođru kaydırıldıđını gsterdi. ift katkılamaya nedeniyle fotokatalitik performanstaki iyileşme yapısal ve morfolojik zelliklerdeki deđişimlere atfedildi.

Anahter Kelimeler: Sentez, bor, zirkonyum, TiO₂, sol-jel, nanotoz, fotokataliz.

To my beloved family

ACKNOWLEDGEMENTS

I would like to tell my sincere gratitude to my advisor Prof. Dr. Abdullah Öztürk for his guidance, support and patience throughout the whole time of this thesis study. Also, I would like to thank him for the freedom that he has given me during the whole thesis study in laboratory.

I would like to thank my co-advisor Assoc. Prof. Dr. Jongee Park for his guidance through the thesis study.

I would like to thank my old and current lab-mates from Photocatalytic Materials Laboratory Basak Aysin, Nursev Bilgin, Esra Corapci, Derya Kapusuz, Tolga Tokmakci for their infinite support and friendship for all the time that we have shared. I would like to give my special thanks to Mertcan Baskan and Berk Dogu, to whom I owe much for always being supportive and entertaining friends. Lastly, Ozgun Acar, Günseli Akcay, Baris Alkan, Ezgi Butev, Tolga Erturk, Serif Kaya, Kivanc Korkmaz, Mustafacan Kutsal, Yelda Meyva, Recai Onal, Burcu Sari, Mehmet Hazar Seren, Suha Tirkes, Simge Tulbez, Burcu Tolunguc, and Koray Yurtisik, and whom I thank, so much and hope to be in touch for the rest of my life. I appreciate all the people that I have known in Metallurgical and Materials Engineering Department, METU for the contributions, they have done in last few years of my life.

Finally, I would like to thank my parents Nesrin and Ali, my sister Elif, my brother-in-law Caner for their never ending love, support and patience and for all the things and time that you have sacrificed, during my thesis study and before, for the last 20 years. Thank you for making me, know that you will always be there for me.

TABLE OF CONTENTS

ABSTRACT	v
ÖZ.....	vii
ACKNOWLEDGEMENTS	x
TABLE OF CONTENTS	xi
LIST OF FIGURES	xvii
LIST OF TABLES	xxv
CHAPTERS	
1. INTRODUCTION.....	1
2. LITERATURE REVIEW.....	5
2.1. Photocatalysis.....	5
2.2. Factors Affecting The Photocatalytic Efficiency	9
2.3. TiO ₂ Photocatalyst.....	10
2.3.1. TiO ₂ Semi-Conductor.....	10
2.3.2. Polymorphs of TiO ₂ Semi-Conductor	12
2.3.3. Application Areas of TiO ₂ (Anatase) Photocatalyst.....	17
2.4. Routes To Improve TiO ₂ Photocatalysis Efficiency And Making TiO ₂ Visible Light Active	18

2.4.1. Physical Approach to Improve the Photocatalytic Efficiency of Anatase	19
2.4.1.1. Particle Size Reduction	19
2.4.2. Chemical Approaches to Improve the Photocatalytic Efficiency of Anatase	19
2.4.2.1. Dye Sensitization.....	19
2.4.2.2. Semi-Conductor Coupling.....	21
2.4.2.3. Doping	22
2.4.2.3.1. Rare Earth Doping.....	22
2.4.2.3.2. Noble Metal Doping.....	23
2.4.2.3.3. Transition Metal Doping	23
2.4.2.3.3.1. Zr Doping	24
2.4.2.3.4. Non-metal Doping.....	25
2.4.2.3.4.1. B Doping	25
2.4.2.3.5. B and Zr Co-Doping.....	26
2.5. Preparation Of TiO ₂ Nanoparticles	26
2.5.1. Ball Milling	26
2.5.2. Hydrothermal Synthesis	27
2.5.3. Sol-Gel Processing	28
2.5.3.1. Factors affecting powder synthesis in sol-gel process	31
2.5.3.1.1. pH.....	31

2.5.3.1.2. Solvent.....	31
2.5.3.1.3. Acid	32
2.5.3.1.4. Water/Metal Alkoxide (Metal precursor) Ratio (R Ratio)..	32
2.5.3.1.5. Drying Conditions	33
2.5.3.1.6. Calcination Regime	34
3. EXPERIMENTAL PROCEDURE	35
3.1. Powder Synthesis	35
3.1.1. Synthesis of Undoped TiO ₂ Powders	36
3.1.2. Synthesis of Doped TiO ₂ Powders	41
3.1.2.1. Synthesis of B Doped TiO ₂ Powders	41
3.1.2.2. Synthesis of Zr Doped TiO ₂ Powders	44
3.1.2.3. Synthesis of B and Zr Co-Doped TiO ₂ Powders.....	47
3.2. Powder Characterization	51
3.2.1. pH Measurement	51
3.2.2. Viscosity Measurement	51
3.2.3. X-Ray Diffraction (XRD) Analysis	51
3.2.4. Scanning Electron Microscope (SEM) Analysis.....	52
3.2.5. Diffuse Reflectance Spectra (DRS) Analysis.....	53
3.3. PHOTOCATALYTIC ACTIVITY MEASUREMENT.....	53
4. RESULTS AND DISCUSSION	57

4.1. General Remarks	57
4.2. Synthesis Of Undoped TiO ₂ Powders	57
4.3. Characterization Of Undoped TiO ₂ Powders	61
4.3.1. pH Measurement	61
4.3.2. Viscosity Measurement	62
4.3.3. X-Ray Diffraction (XRD) Analysis	64
4.3.4. Scanning Electron Microscopy (SEM) Analysis.....	85
4.3.5. Diffuse Reflectance Spectroscopy (DRS)	89
4.4. Photocatalytic Activity Of Undoped TiO ₂ Powders.....	95
4.4.1. Methylene Blue Degradation.....	95
4.4.2. Apparent rate constants	111
4.5. Determination Of Best R Ratio And Calcination Regime.....	115
4.6. Synthesis Of Doped TiO ₂ Powders	117
4.7. Characterization Of Doped TiO ₂ Powders	117
4.7.1. pH Measurements.....	117
4.7.2. Viscosity Measurements.....	118
4.7.3. X-Ray Diffraction (XRD)	119
4.7.4. Scanning Electron Microscopy (SEM).....	140
4.7.5. Diffuse Reflectance Spectroscopy (DRS)	146
4.8. Photocatalytic Activity	148

4.8.1. Methylene Blue Degradation	148
4.8.2. Apparent Rate Constant	157
4.9. Determination Of Best Water Content And Doping Content.....	160
5. CONCLUSIONS	163
REFERENCES	167

LIST OF FIGURES

FIGURES

Figure 1.1. Application areas of TiO ₂ photocatalyst.....	2
Figure 2.1. Schematic diagram of processes occurring during photocatalytic oxidation of acetaldehyde on an illuminated TiO ₂ particle.....	7
Figure 2.2. Degradation pathway of methylene blue molecule.....	8
Figure 2.3. Valence and conduction band positions for some semi-conductors in aqueous electrolytes at pH=1	10
Figure 2.4. Unitcell structures of rutile, anatase and brookite.....	13
Figure 2.5. Crystal structure of titania polymorphs constructed from octahedrons; (a) anatase, (b) rutile, (c) brookite	15
Figure 2.6. Visible light activation of a wide band gap semi-conductor by dye sensitization [LUMO (lowest unoccupied molecular orbital), HOMO (highest occupied molecular orbital)]	20
Figure 2.7. Photoexcitation of TiO ₂ (by visible light) by coupling with a narrow band gap semi-conductor	22
Figure.2.8. Vertical view of a conventional ball mill.....	27
Figure 3.1. Schematic heat treatment procedure	37
Figure 3.2. Flowchart showing the experimental procedure for the synthesis of undoped TiO ₂ powder for R ratio of 10.	38

Figure 3.3. Flowchart showing the experimental procedure for the synthesis of the 3% B doped TiO ₂ powder.....	43
Figure 3.4. Flowchart showing the experimental procedure for the synthesis of the 10 wt% Zr doped TiO ₂ powder.....	46
Figure 3.5. Flowchart showing the experimental procedure for the synthesis of the 3 wt% B and 10 wt% Zr co-doped TiO ₂ powder for R ratio of 10.....	50
Figure 3.6. The flowchart showing the experimental procedure for the MB degradation measurement of the powders.	55
Figure 4.1. Viscosity vs time graph for the solutions prepared for different R ratio.....	62
Figure 4.2. XRD patterns of the undoped TiO ₂ powders in as-dried form.....	65
Figure 4.3. XRD patterns of the 301 series of the undoped TiO ₂ powders.....	67
Figure 4.4. XRD patterns of the 302 series of the undoped TiO ₂ powders.....	67
Figure 4.5. XRD patterns of the 303 series of the undoped TiO ₂ powders.....	68
Figure 4.6. XRD patterns of the 401 series of the undoped TiO ₂ powders.....	69
Figure 4.7. XRD patterns of the 402 series of the undoped TiO ₂ powders.....	69
Figure 4.8. XRD patterns of the 403 series of the undoped TiO ₂ powders.....	70
Figure 4.9. XRD patterns of the 501 series of the undoped TiO ₂ powders.....	71
Figure 4.10. XRD patterns of the 502 series of the undoped TiO ₂ powders.....	71
Figure 4.11. XRD patterns of the 503 series of the undoped TiO ₂ powders.....	72
Figure 4.12. Crystal structure of anatase phase of R50 501. (Blue atoms are titanium, red atoms are oxygen).	76

Figure 4.13. Crystal structure of rutile phase R3 502. (Blue atoms are titanium, red atoms are oxygen).	76
Figure 4.14. Crystallite size of the undoped TiO ₂ powders calcined in different calcination regimes.....	79
Figure 4.15. Well and poor Rietveld refinement fittings for powder R1.	83
Figure 4.16. Well and poor Rietveld refinement fittings for powder R3.	83
Figure 4.17. Well and poor Rietveld refinement fittings for powder R5.	83
Figure 4.18. Well and poor Rietveld refinement fittings for powder R10.	84
Figure 4.19. Well and poor Rietveld refinement fittings for powder R30.	84
Figure 4.20. Well and poor Rietveld refinement fittings for powder R50.	84
Figure 4.21. SEM images of a. powder R1 as-dried and b. powder R1 503.....	85
Figure 4.22. SEM images of a. powder R3 as-dried and b. powder R3 503.....	86
Figure 4.23. SEM images of a. powder R5 as-dried and b. powder R5 503.....	86
Figure 4.24. SEM images of a. powder R10 as-dried and b. powder R10 503..	86
Figure 4.25. SEM images of a. powder R30 as-dried and b. powder R30 503..	87
Figure 4.26. SEM images of a. powder R50 as-dried and b. powder R50 503..	87
Figure 4.27. SEM images of powders a. R1 401, b. R1 501, c. R3 401, d. R5 302, e. R10 302, f. R10 403, g. R30 401, h. R50 402, and i. R50 502.....	88
Figure 4.28. Diffuse reflectance spectra of powder R1 with respect to wavelength for different calcination regimes.	90
Figure 4.29. Diffuse reflectance spectra of powder R3 with respect to wavelength for different calcination regimes.	90

Figure 4.30. Diffuse reflectance spectra of powder R5 with respect to wavelength for different calcination regimes.....	91
Figure 4.31. Diffuse reflectance spectra of powder R10 with respect to wavelength for different calcination regimes.....	91
Figure 4.32. Diffuse reflectance spectra of powder R30 with respect to wavelength for different calcination regimes.....	92
Figure 4.33. Diffuse reflectance spectra of powder R50 with respect to wavelength for different calcination regimes.....	92
Figure 4.34. Percentage of MB degradation with UV light illumination time for all powders in as-dried form.....	99
Figure 4.35. Percentage of MB degradation with UV light illumination time for all of the powders after calcination at 300°C for 1 h.....	100
Figure 4.36. Variation in MB degradation with R ratio for the 300 series of powders.....	101
Figure 4.37. Variation in MB degradation with R ratio for the 400 series of powders.....	102
Figure 4.38. Variation in MB degradation with R ratio for the 500 series of powders.....	102
Figure 4.39. Percentage of MB degradation with UV light illumination time for powder R1 for different calcination regimes.....	104
Figure 4.40. Percentage of MB degradation with UV light illumination time for powder R10 for different calcination regimes.....	106
Figure 4.41. Percentage of MB degradation with UV light illumination time for powder R50 for different calcination regimes.....	107
Figure 4.42. Schematic illustration of TiO ₂ photocatalysis mechanism.....	109

Figure 4.43. Rate constant of powder R1 with respect to UV light illumination time for different calcination regimes.	112
Figure 4.44. Rate constant of powder R50 with respect to UV light illumination time for different calcination regimes.	112
Figure 4.45. Rate constant values calculated from MB degradation test of the powders in daylight for 24 h.	114
Figure 4.46. Comparison of rate constant values calculated from MB degradation tests of the powders in UV light and in daylight.	114
Figure 4.47. XRD patterns of B-doped TiO ₂ powders in as-dried form.	120
Figure 4.48. XRD patterns of Zr-doped as-dried TiO ₂ powders.	121
Figure 4.49. Rietveld fittings of a. R50 As-Dried, b. R50-2B, c. R50-3B, d. R50-4B.	123
Figure 4.50. XRD patterns of B-doped 301 TiO ₂ powders.	124
Figure 4.51. XRD patterns of Zr-doped 301 TiO ₂ powders.	125
Figure 4.52. Rietveld fittings of a. R50 301, b. R50-3B-301.	127
Figure 4.53. XRD patterns of B-doped 501 TiO ₂ powders.	128
Figure 4.54. Interstitial doping of B to the lattice structure (Geng, et al., 2006).	128
Figure 4.55. Rietveld fittings of a. R50 501, b. R50-2B-501, c. R50-3B-501, d. R50-4B-501.	130
Figure 4.56. Constructed crystal structure of R50-3B-501 according to Rietveld refinement results (Blue atoms are titanium, red atoms are oxygen and grey atoms are boron).	131
Figure 4.57. XRD patterns of Zr-doped 501 TiO ₂ powders.	133

Figure 4.58. Rietveld fittings of a. R50 501, b. R50-5Zr-501, c. R50-10Zr-501, d. R50-15Zr-501.....	135
Figure 4.59. Constructed crystal structure of R50-10Zr-501 according to Rietveld refinement results (Blue atoms are titanium, red atoms are oxygen and green atoms are zirconium).	136
Figure 4.60. XRD patterns of R50 at undoped and co-doped case for as-dried, 301 and 501 calcination conditions.	137
Figure 4.61. Rietveld fittings of a. R50 501, b. R50-3B-10Zr-501.	140
Figure 4.62. Constructed crystal structures of R50-3B-10Zr-501 according to Rietveld refinement results (Blue atoms are titanium, red atoms are oxygen, grey atoms are boron, and green atoms are zirconium).....	140
Figure 4.63. SEM images of a. R50 As-Dried (160000x), b. R50 501 (200000x), c. R50 As-Dried (30000x), d. R50 501 (25000x) powders.	142
Figure 4.64. SEM images of a. R50-3B (200000x), b. R50-3B-501 (200000x), c. R50-3B (25000x), d. R50-3B-501 (25000x) powders.	143
Figure 4.65. SEM images of; a. R50-10Zr (200000x), b. R50-10Zr-501 (200000x), c. R50-10Zr (25000x), d. R50-10Zr-501 (25000x) powders..	144
Figure 4.66. SEM images of; a. R50-3B-10Zr (200000x), b. R50-3B-10Zr-501 (200000x), c. R50-3B-10Zr (25000x), d. R50-3B-10Zr-501 (25000x) powders.	145
Figure 4.67. Diffuse reflectance spectra of undoped, B-doped, Zr-Doped, B and Zr Co-Doped powders with 501 calcination condition applied.....	147
Figure.4.68. Visible light range of electromagnetic spectrum	148
Figure 4.69. Adsorption of MB molecule in a (001) surface of TiO ₂ crystal...	150

Figure 4.70. Schematic illustration of B doped TiO ₂ powder's photocatalysis mechanism.....	151
Figure 4.71. Schematic illustration of Zr doped TiO ₂ powder's photocatalysis mechanism.....	152
Figure 4.72. Schematic illustration of B and Zr co-doped TiO ₂ powder's photocatalysis mechanism.....	153
Figure 4.73. Methylene blue degradation graph of the undoped, doped and co-doped powders with composition for powders of R50 that are calcined at 500° C for 1 h, UV-light illumination for 90 min.....	154
Figure 4.74. Rate constant values of R50 in undoped, doped and co-doped conditions, calcined at 500° C for 1 h, after 90 min UV-light illumination.	157
Figure 4.75. Rate constant values of R10 and R50 at undoped, doped and co-doped conditions, calcined at 500° C for 1 hour, after 24 h's of daylight test.	158
Figure 4.76. Rate constant value comparison of R10 and R50 at undoped, doped and co-doped conditions, calcined at 500° C for 1 hour, after 90 minutes of UV-light and 24 h's of daylight illumination test.	159

LIST OF TABLES

TABLES

Table 2.1. Commonly used semi-conductors and their band gap energy values.	11
Table 2.2. Ionic, covalent, atomic, and metallic radius values of B, O, Ti, and Zr. (Candero, et al., 2008; Clementi, et al., 1967; Greenwood and Earnshaw, 1997; Shannon, 1976)	13
Table 2.3. Crystal structure properties of anatase, brookite and rutile phases (Diebold, 2003; Gupta and Tripathi, 2011; Hu, et al., 2003).....	14
Table 2.4. Band gap energies and density values of titania polymorphs (Diebold, 2003; Gupta and Tripathi, 2011).	14
Table 2.5. Ti-Ti and Ti-O bond lengths for anatase and rutile phases (Linsebigler, et al., 1995)	16
Table 3.1. Amount of chemicals needed for the preparation of mother solutions used for the synthesis of the undoped TiO ₂ powders.	36
Table 3.2. The label name of the undoped TiO ₂ powders, their R ratio and calcination regime.	39
Table 3.3. Amount of chemicals needed for the preparation of the solutions used for the synthesis of B doped TiO ₂ powders.....	42
Table 3.4. Labelling of the B doped TiO ₂ powders and their calcination regime.	44

Table 3.5. Amount of chemicals needed for the preparation of the solutions used for the synthesis of Zr doped TiO ₂ powders.....	45
Table 3.6. Labelling of the Zr doped TiO ₂ powders and their calcination regime.	47
Table 3.7. Amount of chemicals needed for the preparation of the solutions used for the synthesis of B and Zr co-doped TiO ₂ powders.	48
Table 3.8. Labelling of the the B and Zr co-doped TiO ₂ powders and their calcination regime.	50
Table 3.9. Initial rietveld fitting parameters and constant parameters	52
Table 4.1. pH values of the initial solutions for different R ratio.....	61
Table 4.2. Percentage of crystallinity of the undoped TiO ₂ powders in as-dried form.	66
Table 4.3. Rutile percentage in selected R1 and R3 powders.....	73
Table 4.4. Fixed variables for Rietveld refinement.	75
Table 4.5. Lattice parameters and cell volume of anatase phase in undoped TiO ₂ powders.	77
Table 4.6. Lattice parameter and cell volume of rutile phase in selected undoped TiO ₂ powders.....	78
Table 4.7. The χ^2 , Rp, and wRp values of the best and worst fitting for the powders calcined in different calcination regimes.	82
Table 4.8. Band gap energy of the undoped TiO ₂ powders synthesized.	93
Table 4.9. MB degradation values of the powders after UV light illumination.	96
Table 4.10. MB degradation and rate constant of the selected powders in daylight.....	113

Table 4.11. pH values of the doped solutions.....	117
Table 4.12. Viscosity values of B or Zr doped and B and Zr co-doped powder solutions for R50 compositions.....	118
Table 4.13. %Crystallinity values of undoped and B doped and Zr doped as-dried TiO ₂ powders with compositions of R50.....	122
Table 4.14. Rietveld refinement results of undoped and B-doped TiO ₂ powders in as-dried condition.....	122
Table.4.15. %Crystallinity values of R10 and R50 powders in undoped, B doped, and Zr doped 301 form.	124
Table.4.16. Rietveld refinement results of undoped and B-doped TiO ₂ powders in 301 condition.....	126
Table 4.17. Rietveld refinement results of undoped and B-doped TiO ₂ powders in 501 condition for R50 composition.....	129
Table.4.18. Rietveld refinement results of undoped and Zr-doped TiO ₂ powders in 501 condition for R50 composition.....	134
Table 4.19. Rietveld refinement results of undoped and B and Zr co-doped TiO ₂ powders in 501 condition.	138
Table 4.20. Band gap energies of the synthesized undoped, doped and co-doped TiO ₂ powders with 501 calcination condition.....	147
Table 4.21. Physical adsorption percentages of R50 calcined at 501 under undoped, doped and co-doped conditions.	150
Table 4.22. % Degradation values of the powders under UV-light illumination.	155
Table 4.23. % Degradation values of powders under daylight illumination. ...	156

Table 4.24. Daylight rate constant/UV-light rate constant values of undoped, doped and co-doped, R10 and R50 powders, calcined at 500°C for 1h. ... 159

CHAPTER 1

INTRODUCTION

In today's world, getting rid of the industrial wastes and pollutants is a crucial issue for environmental concerns. Pollutants emitted from various sources result in severe ecological problems such as pollution of air, water, or soil (Chatterjee and Dasgupta, 2005). Several ways are researched to recycle or to make the wastes and pollutants less hazardous for the living environment. Conventional methods did not result in a satisfactory performance in solving hazardous issues caused by industrial byproducts (Kuo and Ho, 2001; Yao and Wang, 2010). Therefore, new techniques -such as heterogeneous photocatalysis- generally called "Advanced Oxidation Processes" (Chen and Dionysiou, 2008; Houas, et al., 2001) have been developed. The photocatalysis concept has been studied for the last fifty years in order to prevent the damages of the pollution from the organic substances (Heller, 1981), and seems to be more effective than the conventional chemical oxidation methods for the decomposition of toxic wastes to non-hazardous products (Legrini, et al., 1993).

TiO₂ has been the most commonly used semiconductor photocatalyst in heterogeneous photocatalysis applications due to its superior properties such as high oxidizing capability, chemical inertness, low price, nontoxicity, and high availability in the market (Ichihashi, et al., 1997; Gupta and Tripathi, 2011; Seabra, et al., 2011). The highly desirable properties of TiO₂ enabled it to be remarkably commercialized in the market all over the world (Nakata, et al., 2012). TiO₂ photocatalyst has a wide range of industrial applications that are categorized under environmental and energy related branches as shown in Figure 1.1 (Nakata and Fujishima, 2012).



Figure 1.1. Application areas of TiO₂ photocatalyst (Nakata and Fujishima, 2012)

High band gap energy (e.i. 3.2 eV for anatase), low photoquantum energy, and high recombination rate of electron-hole pairs limit the applications of TiO₂ photocatalyst (Etacheri, et al., 2011; Zhang, et al., 1998; Pelaez, et al., 2012; Colmenares, et al., 2006). Studies related to TiO₂ photocatalyst are mainly focused on the improvement of its photocatalytic efficiency since TiO₂ photocatalyst show low photocatalytic activity at daylight because of its wide energy band gap (Zhang and Liu 2008; Kapusuz, et al., 2011). Three different strategies i.e., semi-conductor coupling, dye sensitization, and doping were developed for the improvement of the photocatalytic efficiency of TiO₂ (Rehman, et al., 2009). The most commonly and the most easily applied strategy is doping with other elements (Kapusuz, et al., 2013) via decreasing band gap energy required (Stengl, et al., 2009), and decreasing the electron-hole recombination rate (Colmenares, et al., 2006).

Doping of TiO₂ has been tried by rare earths such as gadolinium [Gd]; neodymium [Nd], cerium [Ce], holmium [Ho], lanthanum [La], erbium [Er], praseodymium [Pr], samarium [Sm], terbium [Tb], europium [Eu], yttrium [Y], transition metals such as iron [Fe], cobalt [Co], copper [Cu], vanadium [V], tungsten [W], nickel [Ni], manganese [Mn], chromium [Cr], molybdenum [Mo], niobium [Nb], zinc [Zn], zirconium [Zr], palladium [Pd], gold [Au], platinum [Pt], silver [Ag], and non-metals such as nitrogen [N], boron [B], fluorine [F], carbon [C], sulphur [S], silicon [Si], germanium [Ge], arsenic [As], antimony [Sb],

tellurium [Te], polonium [Po], chlorine [Cl] (Akpan and Hameed, 2010; Rehman, et al., 2009; Gupta and Tripathi, 2011; Teh and Mohamed, 2011; Pelaez, et al., 2012; Bian, et al., 2009; Patil, 2008). Co-doping is another approach of doping at which two elements are doped to TiO₂ at the same time. Some of the element couples used for this purpose are: boron and zirconium (Kapusuz, et al., 2013); boron and iron (Stengl, et al., 2009); nitrogen and sulphur, nitrogen and fluorine, nitrogen and boron (Rehman, et al., 2009); boron, nickel and cerium, nitrogen and cerium, iron and holmium, iron and zinc (Akpan and Hameed, 2010).

Various chemical and physical production techniques including solvothermal, ball milling, and sol-gel were applied for the TiO₂ synthesis as well as doping and co-doping (Patil, 2008; Ramaswamy, et al., 2008; Su, et al., 2004; Akpan and Hameed 2010; Guillen-Santiago, et al., 2010). Among these techniques sol-gel is one of the most widely used process since it offers the advantages like high purity, low temperature processing, high control over morphology, crystalline phases, nucleation and growth kinetics, and homogeneity (Wright and Sommerdijk, 2001; Pierre, 1998). In sol-gel processing, the pH and viscosity of the initial solution, type or concentration of precursor, water content, solvent, aging conditions, and drying and calcination temperatures are among the parameters affecting the powder morphology and properties (Lee and Gouma 2012). Although several studies were conducted on the synthesis of undoped and doped TiO₂ powders by sol-gel process, studies related to the initial composition and effect of water content on the properties of the solution and morphology of the powder are rare and scarce. (Chen, et al., 2009; Lee and Gouma, 2012; Yoldas, 1986)

The purpose of this study were two fold; to understand the effect of water content of initial solution and calcination regime (time and temperature) on the morphology and photocatalytic properties of sol-gel derived TiO₂ powder, and to improve its photocatalytic efficiency through B or Zr doping, and B and Zr co-doping with respect to undoped TiO₂ powder. The ultimate aim was to improve photocatalytic properties of TiO₂ up to a point at which visible light can activate

it at high photoefficiency. On the one hand, B was chosen for doping because it could easily enter the lattice due to its small ionic size (0.41 Å) relative to size of TiO₂ lattice and decreases the band gap (Rehman, et al., 2009; Zhang and Liu, 2008). On the other hand, large ionic size of Zr (0.86 Å) decreases electron-hole recombination rate, meanwhile increases the anatase to rutile transformation temperature (Lukac, et al., 2007; Kapusuz, et al., 2013). The doped and undoped TiO₂ powders were characterized by using a rheometry, pH meter, X-Ray Powder Diffraction (XRD), Scanning Electron Microscopy (SEM). Photocatalytic performance were evaluated by the degradation of methylene blue (MB) solution under UV light and daylight irradiation. Further investigation was done by Diffuse Reflectance Spectroscopy (DRS) for calculation of the band gap energy of the powders synthesized.

CHAPTER 2

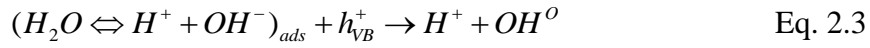
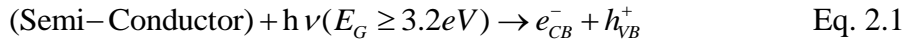
LITERATURE REVIEW

2.1. Photocatalysis

Pollution and industrial wastes are among the biggest environmental concerns nowadays. Several techniques are applied for the removal of wastes and pollutants from air, water, and soil. Physical [adsorption (Dejohn and Hutchins, 1976)], biological [biodegradation (Patil and Shinde 1988; Moore, et al., 1989)], and chemical [chlorination, and ozonation (Slokar and Le Marechal, 1998)] methods have been tried for water decontamination but have not resulted in satisfactory efficiency. They also form secondary pollutants (Yao and Wang, 2010; Kuo and Ho, 2001). Therefore, Advanced Oxidation Processes (AOPs) were introduced (Houas, et al., 2001; Kuo and Ho, 2001; Chen and Dionysiou, 2008). Among AOPs heterogeneous photocatalysis showed the best efficiency at the total mineralization of organics (Hermann, 1999; Hoffmann, et al., 1995).

Photocatalytic reaction is described as reaction catalyzed by photons. The most common example of photocatalytic reactions is photosynthesis reactions. At photosynthesis, chlorophylls adsorb light, H_2O , and CO_2 . Then, starch and O_2 are formed. The required energy for the reaction is taken from incoming photons. Principles of photocatalytic reactions that take place on the surface of TiO_2 are almost the same with photosynthesis. Though, reactions are different from each other. Incoming photons are adsorbed at the surface of semi-conductor (Eq. 2.1). The photons -with energies equal or higher than energy band gap of semi-conductor- excite electrons (e^-) from valance band to conduction band. As a result, electrons being excited are promoted to conduction band, leaving a hole (h^+) at valance band. Hole in the valance band reacts either with a water

molecule or hydroxide ion (OH^-) and forms hydroxyl radical ($\cdot\text{OH}$) (Eq. 2.2). Electron being promoted to conduction band reacts with oxygen molecule and form superoxide radical anion ($\text{O}_2^{\cdot-}$) (Eq. 2.3) (Pelaez, et al., 2012). Since oxygen molecule is supplied as electron acceptor, it prolongs the recombination of electron-hole pairs during photocatalytic oxidation reaction (Kuo and Ho, 2001). Protons neutralize superoxide radicals (HO_2^{\cdot}) (Eq. 2.4). Neutralized superoxide radicals decompose into hydrogen peroxide (H_2O_2) and oxygen (O_2) (Eq. 2.5). Hydrogen peroxide decomposes to (OH^{\cdot}) and (OH^-) via accepting an electron (Eq. 2.6). OH^{\cdot} reacts with organic reactant and oxidizes it and forms H_2O (Eq. 2.7). Another decomposition procedure that takes place is direct oxidation by reacting with holes (Eq. 2.8) (Houas, et al., 2001; Patil, 2008; Seabra, et al., 2011; Lee and Gouma, 2012; Kuo and Ho, 2001).



Schematic diagram of processes occurring during photocatalytic oxidation of acetaldehyde on an illuminated TiO_2 particle is illustrated in Figure 2.1.

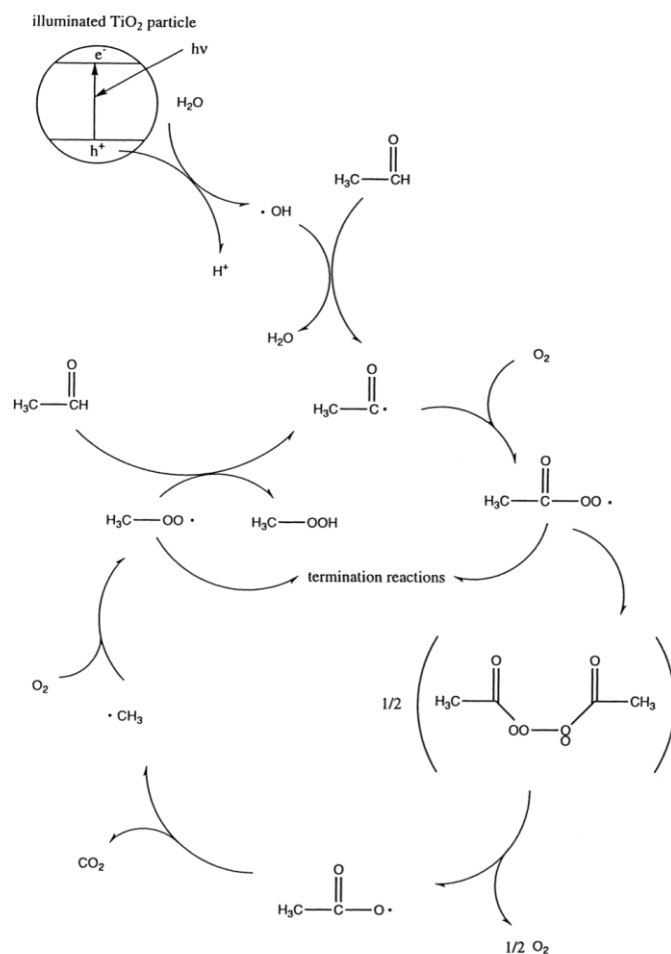


Figure 2.1. Schematic diagram of processes occurring during photocatalytic oxidation of acetaldehyde on an illuminated TiO₂ particle (Fujishima and Tryk, 1999)

MB degradation process is schematically given in Figure 2.2. The procedure is as follows; Cl⁻ is the first ion to detach from the structure upon dissolution of MB. N-CH₃ has the lowest bond dissociation energy (BDE) in the MB structure. It is the first broken bond upon the attack of the radicals. -CH₃ gets oxidized into HCHO or HCOOH. C-N and C-S are the most active parts of the remaining structure. So, during the attack of ·OH and O₃, these bonds are broken easily. Meanwhile, phenyl thiophene formation takes place. In the latter periods, abundance of radical species in the MB solution is generated. These radicals

oxidize organic molecular structures until they turn into one of the following inorganic molecules such as, CO_2 , H_2O , Cl^- , SO_4^{2-} , and NO_3^- (Huang, et al., 2010).

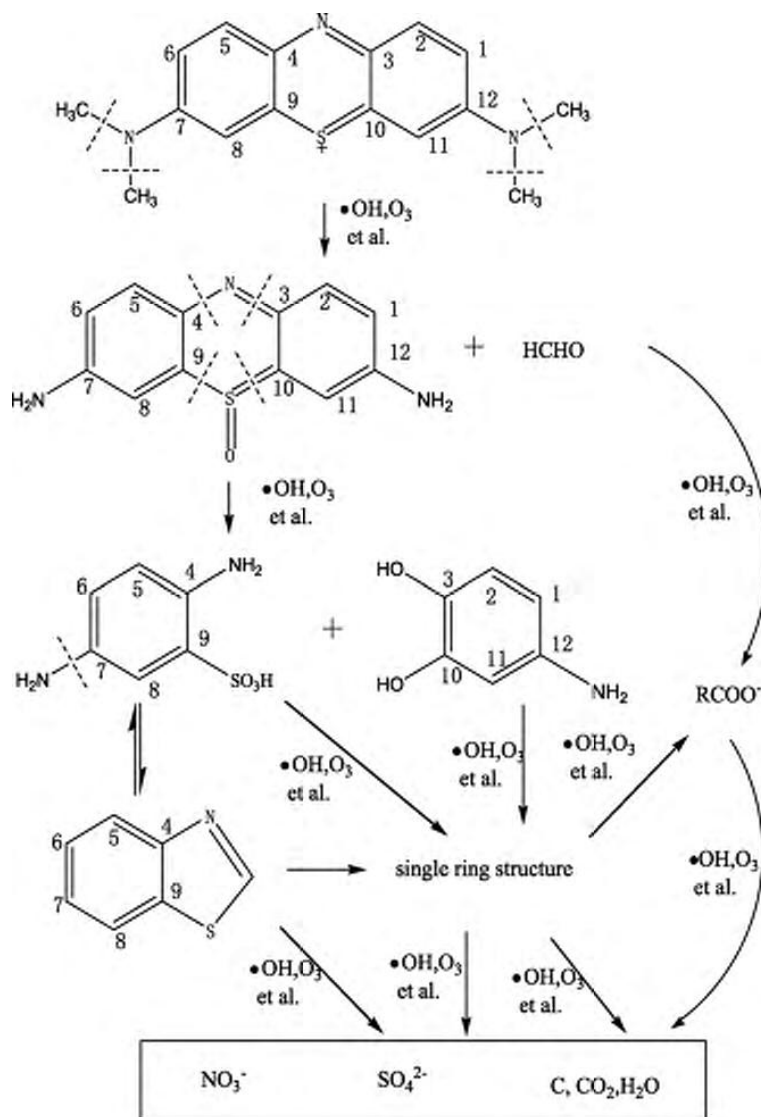


Figure 2.2. Degradation pathway of methylene blue molecule (Huang, et al., 2010).

Final products of a photocatalytic oxidation reaction are CO_2 and H_2O . Semiconductors are found to be the best candidate materials branch for photocatalysis

(Lakshmi, et al., 1995). Among a lot of candidates, best semi-conductor must be chosen for the photocatalytic reaction to take place. The most commonly used semi-conductors are seen in Table 2.1, which are generally metal oxides (e.g. TiO₂, ZnO...), and chalcogenides (e.g. CdS, ZnS, GaAs, ZnSe...) (Lee and Gouma, 2012).

2.2. Factors Affecting The Photocatalytic Efficiency

Heterogeneous photocatalysis is a surface phenomenon (Jung, et al., 2005). So, other than electronic properties it depends on surface properties too. Factors, which affect photocatalytic efficiency of TiO₂ semi-conductor, can be listed as follows:

- Particle size (Pelaez, et al., 2012; Zhang, et al., 1998; Binitha, et al., 2010),
- Crystallite size (Etacheri, et al., 2011; Pelaez, et al., 2012; Colmenares, et al., 2006),
- e⁻/h⁺ recombination rate (Pelaez, et al., 2012; Zhang, et al., 1998; Seabra, et al., 2011),
- Type and amount of doping (Etacheri, et al., 2011; Vereb, et al., 2013; Akpan and Hameed, 2010),
- Powder morphology (Zhang, et al., 2012; Seabra, et al., 2011),
- % Crystallinity (Pelaez, et al., 2012; Binitha, et al., 2010; Colmenares, et al., 2006),
- Specific surface area (Etacheri, et al., 2011; Pelaez, et al., 2012; Binitha, et al., 2010),
- Calcination temperature and time (Lee and Gouma, 2012; Jung, et al., 2005; Zaleska, et al., 2009),
- Band gap (Gorska, et al., 2008; Rehman, et al., 2009; Vorontsov, et al., 2001),
- Present phases and their amounts (Etacheri, et al., 2011; Binitha, et al., 2010; Seabra, et al., 2011),

2.3. TiO₂ Photocatalyst

2.3.1. TiO₂ Semi-Conductor

The primary requirement from an efficient semi-conductor photocatalyst is to have a redox potential of the charged couple lying within the band gap domain of the photocatalyst. Reducing ability of photoelectrons are determined by energy level at the bottom of the conduction band while, oxidizing ability of photoelectrons are determined by top of the valance band (Carp, et al., 2004; Rehman, et al., 2009). Valence and conduction band positions for some semi-conductors in aqueous electrolytes at pH=1 is shown in Figure 2.3.

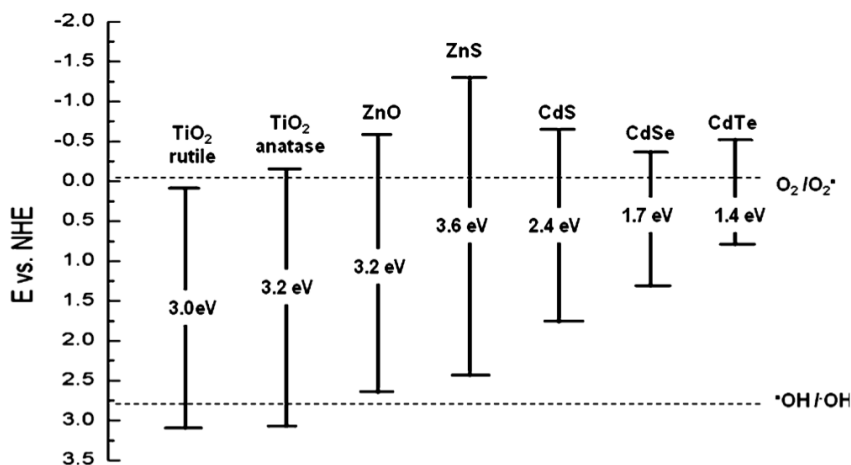


Figure 2.3. Valence and conduction band positions for some semi-conductors in aqueous electrolytes at pH=1 (Lee and Gouma, 2012)

Table 2.1. Commonly used semi-conductors and their band gap energy values.

Semi-Conductor	Band Gap Energy (eV)	Reference
CeO ₂	3.00	Tokmakci, 2013
Fe ₂ O ₃	2.30	Ersoz, 2009; Rehman, et al., 2009
Ga ₂ O ₃	4.60	Tokmakci, 2013
SnO ₂	3.80	Ersoz, 2009; Gupta and Tripathi, 2011
TiO ₂ (Anatase)	3.20	Ersoz, 2009
TiO ₂ (Rutile)	3.00	Ersoz, 2009
WO ₃	3.20	Zhao and Yang, 2003
ZnO	3.20	Lee and Gouma, 2012; Zhao and Yang, 2003
GaAs	1.40	Rehman, et al., 2009;
GaAsP	2.25	Gupta and Tripathi, 2011
SiC	3.00	Gupta and Tripathi, 2011
GaP	2.23	Gupta and Tripathi, 2011
CdS	2.50	Lee and Gouma, 2012
ZnS	3.60	Zhao and Yang, 2003
CdSe	1.70	Gupta and Tripathi, 2011
CdTe	1.40	Lee and Gouma, 2012
SrTiO ₃	3.20	Zhao and Yang, 2003

Besides having suitable band gap energy, there are some other properties, which are expected to be satisfied by an ideal semi-conductor. These properties are being easy to produce and use, cost effectiveness, photostability, nonhazardous for humans and environment, effective activation by solar light, and catalyzing reaction efficiently (Carp, et al., 2004; Rehman, et al., 2009; Lee and Gouma, 2012). Most of the semi-conductors given in Table 2.1 have some limitations. That is, GaAs, PbS, and CdS are not stable enough for aqueous catalysis since they are toxic and undergo photocorrosion (Mills and Hunt, 1997). ZnO is unstable, since it dissolves in water and forms $Zn(OH)_2$ on ZnO particle surface that inactivates the catalyst by passing time (Bahnemann, et al., 1987). Fe_2O_3 , SnO_2 , WO_3 show a conduction band edge at an energy level that is below reversible hydrogen potential, thus systems that use these materials need external electrical potential for completing the water splitting reaction (Sivula, et al., 2009).

Being cheap, available on market, photostability in solutions, chemical inertness (even in hot acids), thermal stability, nontoxicity, having holes with high oxidizing capability are the properties that make the TiO_2 semi-conductor almost the ideal photocatalyst (Lakshmi, et al., 1995; Seabra, et al., 2011; Rehman, et al., 2009; Gupta and Tripathi, 2011; Lee and Gouma, 2012). However, it has a major drawback of not being able to absorb solar light for photocatalysis purposes (Gupta and Tripathi, 2011).

2.3.2. Polymorphs of TiO_2 Semi-Conductor

Titania (TiO_2) is a naturally occurring oxide of titanium metal. In nature it can be found in five different crystal forms namely: anatase, brookite, rutile, monoclinic TiO_2 , and orthorhombic TiO_2 (Teh and Mohamed, 2011). Monoclinic and orthorhombic TiO_2 phases are only found in Ries crater in Germany in the form of granit gneisses (El Goresy, et al., 2001; Carp, et al., 2004). Anatase, brookite, and rutile are the phases to be considered for photocatalysis applications (Li, et al., 2004; Ramaswamy, et al., 2008). Unit cell structures of rutile, anatase and brookite are illustrated in Figure 2.4.

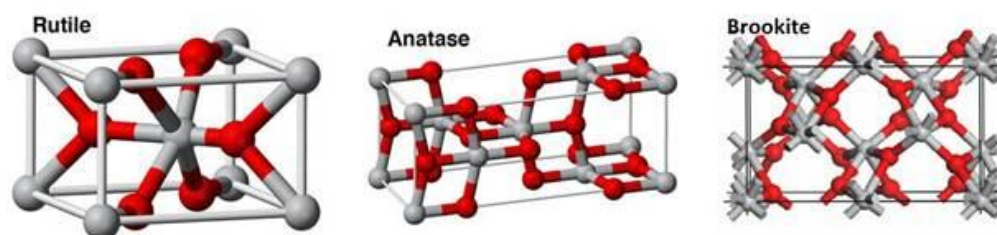


Figure 2.4. Unitcell structures of rutile, anatase and brookite (Shannon, 2012)

Three polymorphs of titania show difference in crystal structure, physical properties, and electronic properties. Ionic, covalent, atomic, and metallic radius values of boron, oxygen, titanium, and zirconium were tabulated in Table 2.2. Knowing the ionic and atomic radius lattice structure of the powders can be imagined much easily, and mechanism of how doping takes place is understood in a more solid way.

Table 2.2. Ionic, covalent, atomic, and metallic radius values of B, O, Ti, and Zr. (Candero, et al., 2008; Clementi, et al., 1967; Greenwood and Earnshaw, 1997; Shannon, 1976)

Radius Type (pm)	B		O		Ti		Zr	
Ionic	B³⁺	41	O²⁻	126	Ti⁴⁺	74.5	Zr⁴⁺	86
Covalent	84		66		168		175	
Atomic	87		48		176		206	
Metallic	-		-		147		160	

Crystal structure properties of the polymorphs of titania are given in Table 2.3. The values given below will have a very important task during rietveld refinement of the samples.

Table 2.3. Crystal structure properties of anatase, brookite and rutile phases (Diebold, 2003; Gupta and Tripathi, 2011; Hu, et al., 2003)

Phase	Crystal System	Space Group	Lattice Constants (nm)			
			a	b	c	c/a
Anatase	Tetragonal	I4 ₁ /amd	0.3733	-	0.9370	2.510
Brookite	Rhombohedral	Pbca	0.5436	0.9166	0.5135	0.944
Rutile	Tetragonal	P4 ₂ /mnm	0.4584	-	0.2953	0.644

Band gap energies and density values of the polymorphs of titania is presented in Table 2.4. to show the difference between their band gaps and densities. Those values enable us to understand the effect of crystal structural differences in macro scale. For example, density differences are related to the connection types of octahedras that formed both three phases.

Table 2.4. Band gap energies and density values of titania polymorphs (Diebold, 2003; Gupta and Tripathi, 2011).

Phase	Band gap (eV)	Density (g/cm ³)
Anatase	3.2	3.79
Brookite	2.96	3.99
Rutile	3.0	4.13

When photocatalytic reactions are the case, brookite is not studied much, since it does not show significant photocatalytic activity as anatase and rutile does (Etacheri, et al., 2011; Gupta and Tripathi, 2011). Therefore, comparison

between phases is made generally between anatase and rutile for photocatalytic reactions. Thermodynamically anatase is a metastable phase with respect to rutile in macroscale (Gouma and Mills, 2001). But, in nanoscale the phase stability of TiO₂ polymorphs depend on the size of the powder (Fujishima, et al., 2008; Gupta and Tripathi, 2011). For particles larger than 35 nm, rutile is the most stable phase. For particles smaller than 11 nm, anatase is found to be the most stable phase. For particles ranging from 11 to 35 nm brookite is the most stable phase.

Crystal structures of all phases are composed of TiO₆ octahedras that were connected variously by corners and edges as seen in Figure 2.5. Both structures of anatase and rutile are the distorted forms of octahedras, which are connected via corners and edges. (Li, et al., 2004). In these structures each Ti⁴⁺ ion has six O²⁻ ions as neighbors in octahedral. Octahedrons that form rutile are not regular. They show slight distortion through orthorhombic structure. Octahedrons at anatase structure are significantly distorted. As a result, their symmetry is lower than orthorhombic.

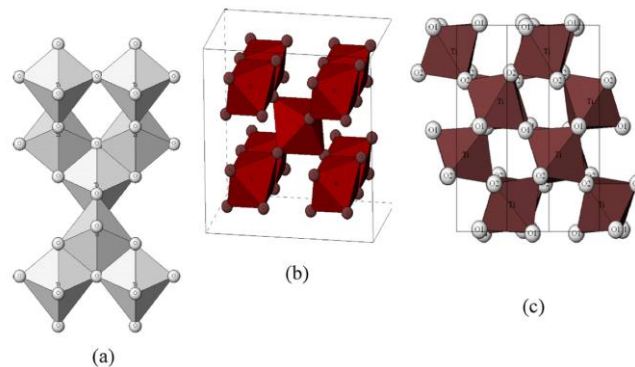


Figure 2.5. Crystal structure of titania polymorphs constructed from octahedrons; (a) anatase, (b) rutile, (c) brookite (Pelaez, et al., 2012)

The bond lengths of Ti-Ti and Ti-O differ between anatase and rutile too. Ti-Ti bond length is higher and Ti-O bond length is smaller in anatase than rutile as seen in Table 2.3. At rutile structure each octahedron has ten neighboring octahedrons (two shares edge oxygen pairs and eight shares corner oxygen atoms). Meanwhile, this number is eight (four shares edge and other four shares corner) for anatase structure (see Figure 2.5). The different band gap and density values are the results of these differences in lattice structure of the titania polymorphs (Linsebigler, et al., 1995).

Table 2.5. Ti-Ti and Ti-O bond lengths for anatase and rutile phases (Linsebigler, et al., 1995)

Phase	Ti-Ti Bond Length (Å)		Ti-O Bond Length (Å)	
Anatase	3.79	3.04	1.934	1.980
Rutile	3.57	2.96	1.949	1.980

At first sight, rutile seems to be a better candidate than anatase due to its lower band gap energy value. Nevertheless, too high electron-hole recombination rate causes rutile to preserve a lower photocatalytic activity than anatase. Also, anatase shows better chemical and photon characteristics because of its superior adsorptive affinity for organic compounds (Seabra, et al., 2011). Furthermore, anatase has higher charge-carrier mobility, lower density, and higher density of surface hydroxyl groups leading to a better photocatalytic activity (Patil, 2008; Etacheri, et al., 2011).

The major drawback of TiO₂ for photocatalytic applications is that it cannot adsorb visible light, which limits its commercial usage (Gupta and Tripathi, 2011). Consequently, studies are focused on the improvement of the visible light absorption capability of TiO₂ and having higher carrier lifetime (Patil, 2008). Several chemical and physical routes for instance; dye sensitization, doping,

semi-conductor coupling, particle and crystallite size reduction were suggested for the improvement of the photocatalytic activity and making anatase crystal visible light active (Gupta and Tripathi, 2011; Rehman, et al., 2009; Ramaswamy, et al., 2008; Grabowska, et al., 2009).

2.3.3. Application Areas of TiO₂ (Anatase) Photocatalyst

TiO₂ photocatalyst has a huge spectrum of application areas as indicated in Figure 1.1. Because of the increased number of the wastewater amount, applications have been generally focused on waste water treatment (Lakshmi, et al., 1995) since Fujishima and Honda first published the water splitting ability of TiO₂ photocatalyst in 1972. TiO₂ containing paper (Fujishima, et al., 2000), microporous textured TiO₂ films (Fujishima, et al., 2000), self-cleaning TiO₂-coated glass (Fujishima, et al., 2000; Mohammadi, et al., 2008; Zaleska, et al., 2009; Etacheri, et al., 2011), water purification (Fujishima, et al., 2000; Byrappa and Adschiri, 2007; Zaleska, et al., 2009; Lakshmi, et al., 1995; Guillen-Santiago, et al., 2010), photocatalytic sterilization (Fujishima, et al., 2000), cancer treatment (Fujishima, et al., 2000; Etacheri, et al., 2011), pigments in paints (Colmenares, et al., 2006; Mohammadi, et al., 2008; Suresh, et al., 1998; Ramaswamy, et al., 2008; Akpan and Hameed 2010), solar cells (Colmenares, et al., 2006; Mohammadi, et al., 2008; Xu, et al., 1999; Su, et al., 2004; Akpan and Hameed, 2010), air purification (Byrappa and Adschiri, 2007; Vorontsov, et al., 2001; Zaleska, et al., 2009; Guillen-Santiago, et al., 2010), anti-bacterial applications (Namratha and Byrappa 2012; Zaleska, et al., 2009; Vereb, et al., 2013; Aysin, et al., 2013; Xue, et al., 2013), anti-reflection coating (Mohammadi, et al., 2008; Wang, et al., 1997), sensing film for gas sensors (Mohammadi, et al., 2008; Suresh, et al., 1998; Ramaswamy, et al., 2008), generation of H₂ gas (Kasuga, et al., 1997; Zaleska, et al., 2009), storage (Su, et al., 2004), and CO₂ photoconversion to methane and low hydrocarbons (Zhang, et al., 2012) are some of the major application areas of TiO₂.

Not being able to adsorb visible light is a problem that still awaits for a solution.

2.4. Routes To Improve TiO₂ Photocatalysis Efficiency And Making TiO₂ Visible Light Active

Since band gap energy of anatase TiO₂ (3.2 eV) is equal to a light with a wavelength of 387.5 nm, the wavelength of the incoming light must be equal to or smaller than 387.5 nm to activate anatase TiO₂ photocatalytically. Therefore, photocatalytic activity is limited in UV light since only ≈5-7% of the solar spectrum is UV light (Binitha, et al., 2010) that decreases the photocatalytic efficiency of anatase much. It is possible to get better efficiency for the lights with smaller wavelengths in electromagnetic spectrum. Analysis of the rest of the solar spectrum results showed that 46% is visible light and 47% is infrared radiation. If band gap can be decreased (shifting the wavelength of the light which is capable of activating the anatase photocatalytically) amount of the light that can activate the reactions will increase which will result in a direct increase at photocatalytic efficiency of titania powders (Rehman, et al., 2009).

In order to increase photocatalytic activity three enhancements are considered. First, inhibition of recombination by increased charge separation. Second, enabling a photo response for a wider range of solar spectrum. Last, changing the selectivity or yield of a particular product (Linsebigler, et al., 1995; Lee and Gouma, 2012).

Several approaches were developed and categorized under two branches; physical and chemical. Physical approach suggests making particles (crystallite size) with smaller sizes (Pelaez, et al., 2012). Dye sensitization, semi-conductor coupling, and doping are the chemical approaches applied to improve photoefficiency of anatase (Rehman, et al., 2009; Gupta and Tripathi, 2011).

2.4.1. Physical Approach to Improve the Photocatalytic Efficiency of Anatase

2.4.1.1. Particle Size Reduction

Relationship between photocatalytic performance and morphological properties (shape, size, and surface area) is an important aspect. Moreover, the medium in which TiO₂ is being used affects the photocatalytic activity (Maldotti, et al. 2003). High absorption cross section, fast carrier diffusion on the interface that, in principle, can reduce electron hole recombination rate, and high surface area to volume ratio (higher specific surface area) are the advantages that were obtained by using nanostructured semi-conductors (Lee and Gouma, 2012). An experimental study conducted by Maira, et al. in 2001 on photo-oxidation of toluene with small and large particles confirmed that smaller particle size leads to better photocatalytic activity.

2.4.2. Chemical Approaches to Improve the Photocatalytic Efficiency of Anatase

2.4.2.1. Dye Sensitization

Dye sensitization of TiO₂ via physisorbed or chemisorbed dyes can improve the efficiency of the excitation process. It might finalize with an expansion at wavelength range of the excitation for the photocatalyst. Most commonly used dyes are erythrosine B, thionine, and tris ruthenium (II)(RuL₃⁴⁺) (Lee and Gouma, 2012).

If the oxidative energy level of excited state of the conduction band of the dye is more negative than that of the semi-conductor, excited electron of the dye will be transferred to the conduction band of the semi-conductor. Transferred electrons jump over to the surface of titania where they are scavenged by molecular oxygen to form superoxide radical O₂^{•-} and hydrogen peroxide radical [•]OHH as illustrated in Figure 2.6. Organic molecules are mineralized with a reaction with

the formed radicals. Since, the electron promotion to the conduction band of semi-conductor is done from valence band of the dye, no hole formation takes place at the valence band of the semi-conductor. During the dye sensitization procedure, as long as pollutants are in the solution, self-degradation of the dyes is not favorable. However, after pollutants are degraded, dyes themselves are attacked by the active species (Rehman, et al., 2009).

Interfacial electron transfer between dye and semi-conductor depends on nature of the sensitizer, semi-conductor, and their interactions (Pelaez, et al., 2012). Electron injection times may vary from femto seconds to pico seconds, just by changing the semi-conductor for the same case (Asbury, et al., 2001).

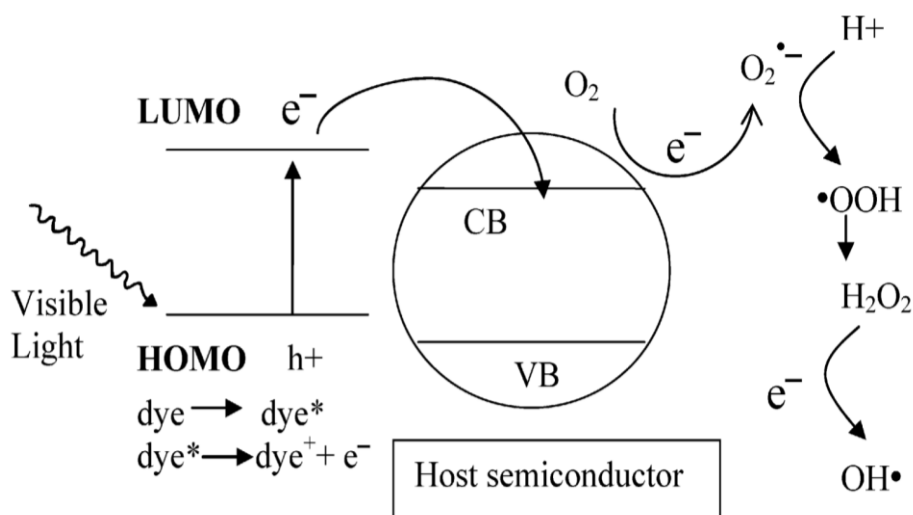


Figure 2.6. Visible light activation of a wide band gap semi-conductor by dye sensitization [LUMO (lowest unoccupied molecular orbital), HOMO (highest occupied molecular orbital)] (Rehman, et al., 2009)

Quantity of the adsorbed dye is the parameter that mostly determines the efficiency of the process that depends on the initial dye concentration, nature of the dye, surface area of the photocatalyst, and pH of the solution. Surface charge

of the solution is determined by its pH. Dye adsorption is minimum at zero surface charge, which is observed at isoelectric point of the catalyst. Above isoelectric point, surface of the catalyst is positively, below it negatively charged. Effect of the charge depends on the nature of the dye being used. For example, acidic dyes favor pH below isoelectric point. Surface area is another important parameter for having higher number of adsorption sites. Since, as it gets higher, number of adsorption sites gets higher too (Rehman, et al., 2009).

2.4.2.2. Semi-Conductor Coupling

Semi-conductor coupling increases photocatalytic activity by decreasing the recombination rate and expanding the energy range of photoexcitation for the system (Lee and Gouma, 2012). ZnO/TiO₂, CdS/TiO₂, Bi₂O₃/TiO₂ are some of the most commonly used couples (Pelaez, et al., 2012). CdS/TiO₂ couple will be used for the explanation of the process. CdS can be activated by visible light but, it cannot be used for photocatalytic applications since prone to photo-anodic corrosion in aqueous environments. It has a stability problem and low photocatalytic activity. Coupling it with TiO₂ increases its both stability in aqueous environments and photocatalytic activity (Pelaez, et al., 2012).

The energy of the visible light is not high enough to excite TiO₂, but is large enough for CdS ($E_{\text{gap}}=2.5$ eV). Upon excitation of the semi-conductor, a hole is formed at valance band of CdS. However, electron transfers from the valance band of CdS to the conduction band of TiO₂, which increases charge separation and efficiency of the system. Photoexcitation of TiO₂ by coupling with a narrow band gap semi-conductor is seen in Figure 2.7. The separated electron and hole are free to undergo electron transfer with adsorbates on the surface (Linsebigler, et al., 1995).

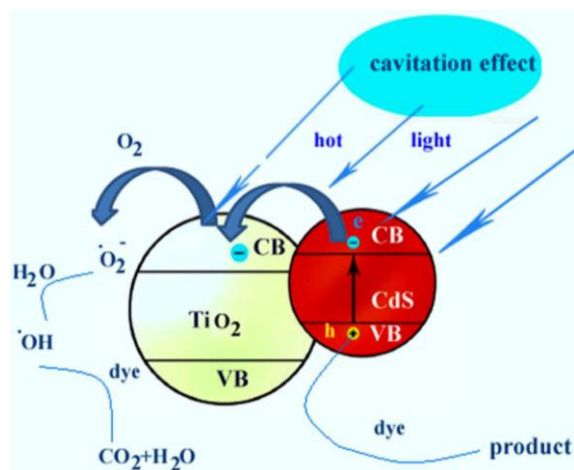


Figure 2.7. Photoexcitation of TiO_2 (by visible light) by coupling with a narrow band gap semi-conductor (Ghows and Entezari, 2011)

Finally, there is one last point that has a direct effect on photoefficiency of these systems. It is the geometry of the particles, contact surface between particles and the particle size. These parameters depend on the manner with which the couples are prepared (Pelaez, et al., 2012).

2.4.2.3. Doping

Doping is occupied for the improvement of photoresponse of TiO_2 . To do so, noble metals, transition metals, rare earths, and non-metals are used (Pelaez, et al., 2012). Doping decreases the recombination rate of electrons and holes. Ions used for doping act as electron traps. Also, they decrease the band gap energy (Hoffmann, et al., 1995).

2.4.2.3.1. Rare Earth Doping

Rare earth elements, scandium (Sc), yttrium (Y) and 15 lanthanoid elements, have incompletely filled 4f orbitals and empty 5d orbitals. They often serve as

catalyst. As a result, incorporation of these elements with TiO₂ results in an improved photocatalytic activity. Photoactivity improvement is generally due to the transition of 4f electrons in rare earth ions, which led to the enforcement of optical adsorption of the photocatalysts and supported the separation of photogenerated electron-hole pairs. Another observed effect is the inhibition of grain growth that results in a smaller crystallite size and higher specific surface area (Teh and Mohamed, 2011).

2.4.2.3.2. Noble Metal Doping

Noble metal doping changes photocatalytic properties by changing the surface properties. Fermi levels of the noble metals are lower than that of TiO₂. Therefore, photoexcited electrons are transferred from the conduction band of TiO₂ to metal particles that are deposited on the surface of TiO₂, while photogenerated holes remain in the valence band of TiO₂. This electron transfer decreases the possibility of electron-hole recombination that results in higher photocatalytic activity and efficient separation. In other words, noble metal doping radically changes electron distribution. Photocatalytic properties are not affected by geometry or morphology of the system or dopant. However, dopant amount has the upmost importance because after a certain concentration photon adsorption begins to decrease and these metal particles became electron-hole recombination centers (Gupta and Tripathi, 2011; Linsebigler, et al., 1995).

2.4.2.3.3. Transition Metal Doping

Transition metal ions provide extra energy levels within the band gap of a semiconductor. The energy required from one of these levels to the conduction band is lower than photon energy required for the situation of unmodified TiO₂. In other words, doping decreases the band gap (Teh and Mohamed, 2011).

Another benefit of transition metal doping is the improved trapping of electrons to inhibit electron-hole recombination during illumination. Amount of dopant has a profound effect on photocatalytic activity. Very small concentrations are beneficial for the process; but large concentrations are detrimental for the photocatalytic activity of TiO₂ (Linsebigler, et al., 1995).

For a photocatalytic reaction to occur electrons and holes must be transferred to the surface of the photocatalyst. Thus, dopants should be near the surface of photocatalyst for efficient charge transfer (Gupta and Tripathi, 2011).

2.4.2.3.3.1. Zr Doping

Zr acts as a stabilizing agent of anatase by shifting the anatase to rutile transformation temperature to higher values. Also, doping with cations having valance smaller than +4 accelerate the transformation due to the provision of a charge compensation mechanism by which the vacancies -that enhance the atom transportation in the system- are formed. On the other hand, cations with valance higher than +4 hinder ionic transformation with formation of Ti³⁺ cations that results with suppression of the transformation (Lukac, et al., 2007; Kapusuz, et al., 2011). Zr suppresses anatase to rutile transformation by two main mechanisms. Zr doping increases the strain energy by substituting the Ti⁴⁺ in anatase structure. For phase transformation to take place firstly, strain energy must be overcome to initiate the phase transformation (Kingery, et al., 1976). Also, formation of Ti-Zr-O bond shifts the transformation temperature to higher values by decreasing the mobility of Ti atoms (Reidy, et al., 2006; Yang and Ferreira, 1998).

Zr doping decreases the recombination rate of electrons-holes by trapping electrons (Kapusuz, et al., 2013). Ionic radius of Zr⁴⁺ (0.86 Å) are bigger than that of Ti⁴⁺ (0.745 Å) (Shannon and Prewitt, 1969). Consequently, with a successive doping an expansion at the lattice is expected. Structure tries to compensate this energy by forming defects (Hirano, et al., 2003).

2.4.2.3.4. Non-metal Doping

Non-metal doping results with the mixing of the “p” orbitals of the non-metal doping (N, S, C or B) with the O 2p orbitals, which results in the upward shifting of the valence band and narrowing of the band gap energy of TiO₂. Contrary to metal doping, non-metal doping do not form recombination centers on the surface of TiO₂. Therefore, non-metal doping enhances photocatalytic activity more effectively (Gupta and Tripathi, 2011). The number of generated electrons and holes are more than other doping (transition metals, noble metals, rare earth elements) systems (Teh and Mohamed, 2011).

2.4.2.3.4.1. B Doping

Boron doping is confirmed to improve photocatalytic activity of TiO₂. Doped boron atoms are found in three different positions in the TiO₂ lattice structure. They may enter the lattice interstitially, replace oxygen atom in the lattice, or may form B₂O₃ compound (Rehman, et al., 2009). After certain amount of doping, B begins to form B₂O₃ in the structure. B₂O₃ formation causes a decrease at photocatalytic performance of anatase crystal (Zaleska, et al., 2008) due to its band gap energy of 6.3 eV (Rehman, et al., 2009). As B replaces O in the structure it forms bonds with two oxygens and two titanium atoms, which causes formation of a midgap that eventually decreases the band gap energy of the system (Teh and Mohamed, 2011).

Radius of B³⁺ is 41 pm and that of Ti⁴⁺ is 74.5 pm (Shannon, 1976). For this reason, it is difficult for B³⁺ to replace Ti⁴⁺. Rather than replacing titanium ion, boron ion enters the lattice interstitially. Boron occupied interstitial sites have great role for improving the microstructural parameters such as high specific surface area and pore volume that enables higher photocatalytic activity (Stengl, et al., 2009).

Boron atoms causes very low crystallite sizes and oxygen vacancies in the structure, that leads to lower recombination rates – which is good for photocatalytic activity- by leading holes to the surface and forming electron traps (Kapusuz, et al., 2013). Lowering of the recombination rate enables visible light activation of TiO₂ (Teh and Mohamed, 2011). B atoms also inhibit the grain growth by promoting the anatase to rutile transformation (Zaleska, et al., 2008).

2.4.2.3.5. B and Zr Co-Doping

Co-doping is used as an effective way of improving the charge separation. Generally, a remarkable improvement of visible light efficiency is seen at co-doped samples when compared with undoped and single doped TiO₂ as a result of the synergetic effect of the elements (Rehman, et al., 2009; Gupta and Tripathi, 2011).

Analysis of boron at co-doped systems revealed that it has a very high impact on the photocatalytic efficiency of TiO₂ (Akpan and Hameed, 2010). Boron decreases band gap to values whose equivalent is the light in the visible range of electromagnetic spectrum. Therefore, with the addition of recombination rate lowering property of Zr the photocatalysis reaction of B and Zr Co-Doped powder will be more efficient than those of both undoped, B doped, Zr doped powders. (Rehman, et al., 2009; Kapusuz, et al., 2013). Furthermore, boron doping favors anatase to rutile transformation though Zr inhibits it, neutralizing each other at that case (Zaleska, et al., 2008; Lukac, et al., 2007).

2.5. Preparation Of TiO₂ Nanoparticles

2.5.1. Ball Milling

Ball milling has been proven to be an effective and simple method for large-scale production of nanopowders (Zhang and Liu, 2008). Powders and crashing

balls are put in the container and it starts its rotation at constant rpm as shown in Figure 2.8. Two mechanical events are observed during this procedure; cold-welding and fragmentation. Cold-welding is the agglomeration of the colliding powders resulting in increased average particle size. But then, at fragmentation process these agglomerated powders began to break up (Salah, et al., 2011).

Milling container, milling speed, milling time, ball-to-powder weight ratio, milling atmosphere and temperature of milling to achieve desired microstructure of product are the parameters that need optimization during powder production (Suryanarayana, 2001).

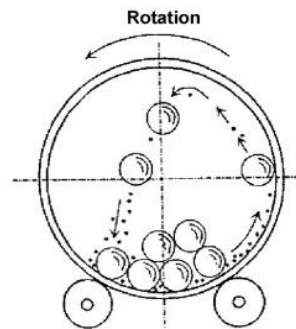


Figure.2.8. Vertical view of a conventional ball mill (Suryanarayana, 2001)

TiO₂ source, doping agent, some organics, and balls are put in the container. Then, milling is done at a constant rpm for required amount of time. Obtained powders are dried in an oven to get rid of remaining organics, water, and alcohol. The powders are calcined to have crystalline TiO₂ (Aysin, et al., 2013).

2.5.2. Hydrothermal Synthesis

Hydrothermal process has been one of the mostly occupied production techniques for the production of TiO₂ powder because it offers high control over

diffusion kinetics, phase purity, crystal symmetry, narrow particle size distribution, lower energy requirement, fast reaction time, and lower sintering temperature (Namratha and Byrappa, 2012; Byrappa and Adschiri, 2007). Behavior of the system depends on processing parameters like pH, viscosity, density, and coefficient of expansion with respect to pressure and temperature (Namratha and Byrappa, 2012). Generally, increasing pH results in higher percentage of anatase and decreasing pH results in more rutile phase. Increasing temperature increases the alkali titanate formation affinity. If pH gets closer to 12 amorphous materials are obtained. Also, increasing processing time and temperature results in faceted grains with bigger sizes (Byrappa and Adschiri, 2007).

Required chemicals are added into the container, then autoclave is started for a given time, temperature, and pressure. Obtained powders are washed with HCl or deionized water and dried at furnace. Generally, no further calcination is required for the powders produced by this technique.

2.5.3. Sol-Gel Processing

The term “Sol-Gel” refers to the first stage of materials transformation from a “liquid-like” sol to a “solid-like” gel. Sol-gel can be categorized as room temperature wet chemistry-based formation of solid inorganic materials from molecular precursor. Sol-gel is used for production of wide range of materials such as nanoceramics, electronic ceramics, photovoltaic ceramics, corrosion and abrasion films, and membranes. Sol-gel enables the low temperature synthesis of the nanoceramics and it is important due to the following reasons:

1. Low temperature processing allows wider selection of support materials such as plastic, wood or cotton that cannot withstand high temperature.
2. Low temperature is beneficial for controlling the size of crystal and to obtain fine nanocrystals.

3. A low temperature approach saves energy consumed in the production steps, by decreasing the overall costs (Chen, et al., 2009).

Sol-gel is the most commonly occupied technique for production of TiO₂ nanopowders because it offers several advantages those makes it a better candidate than other techniques for several applications. First of all, process and the equipment used are very simple. Good mixing is easily achieved at multicomponent systems. Precise particle size, shape control, high homogeneity, control over surface morphology, high specific surface area, small crystallite size, high control over crystallinity and phase structure can be achieved at low temperatures. Sol-gel is a reversible process, which enables recycling of the products. Monoliths, powders, spheres, fibers, and thin coatings can be produced. There are a lot of parameters that can be manipulated to achieve required material with satisfactory properties. Solution viscosity, type or concentration of precursor, pH, water content, solvent, aging conditions, calcination temperature are some of the important parameters. Sol-gel has a few disadvantages. For instance, volumetric change is very high, residual carbon can be found, porosity amount may be high (can be beneficial according to the requirements of the application to be used in) (Chen and Dionysiou, 2008; Woolfrey and Bartlett, 1998; Yoldas, 1986; Lee and Gouma, 2012).

A typical sol-gel process is composed of four steps namely; hydrolysis, condensation, oxopolymers, and oxide network. The reactions involved in these steps are shown in Eq 2.9 through Eq 2.12. (Su, et al., 2004; Lee and Gouma, 2012). Sol-gel reactions have two main branches according to the type of precursor consumed during the synthesis of the product. Those routes were named as non-alkoxide route (also known as particulate sol-gel) and alkoxide route (also known as polymeric sol-gel) (Carp, et al., 2004). Non-alkoxide route proceeds with consumption of inorganic salts (such as nitrides, chlorides, etc.). The powders synthesized via this route must be washed for the removal of the inorganic anions. Watson et al., 2003, published that surface hydroxyl groups are removed upon washing of the sol-gel synthesized TiO₂ powders, which is not good for photocatalytic performance of the powder. On the other hand, alkoxide

sol-gel employs metal alkoxide precursors; from which, sols, gels and precipitates are formed via hydrolysis and condensation reactions (Carp, et al., 2004).

Hydrolysis

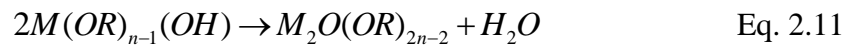


Condensation

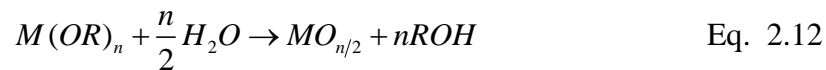
Dehydration



Dealcoholation



Net Reaction



Having high control over the evolution of morphology can be achieved by separation of hydrolysis and condensation stages (Livage et al., 1988). This separation can be achieved by acid-base catalysis. It has been found out that acid catalysis increases hydrolysis rates and highly crystalline powders are formed from total hydrolysis of the alkoxide precursor. Base catalysis, on the other hand, promotes condensation; upon that amorphous powders with unhydrolyzed alkoxide ligands are formed (Carp, et al., 2004).

2.5.3.1. Factors affecting powder synthesis in sol-gel process

2.5.3.1.1. pH

Solid oxides in aqueous suspensions may have electrical charge due to amphoteric dissociation of surface hydroxyl groups, adsorption of H^+/OH^- ions, or metal hydroxo compounds from the hydrolysis of solid materials (Lee and Gouma, 2012). Resultant surface charge depends on pH. Strong repulsive forces among charged particles reduce the probability of coalescence and thus more stable sols can be formed in acidic or alkaline media (Zhang and Banfield, 1998). Isoelectric point of TiO_2 is between pH values of 5-6. In order to decrease agglomeration, pH must be above or below these values for decreasing the electrostatic attraction (Woolfrey and Bartlett, 1998).

Decreasing pH results in larger crystallite sizes that causes significant decrease in specific surface area. Increasing pH, decreases the atomic mobility that favors the anatase phase and inhibits the anatase to rutile transformation (Venz, et al., 1998). If pH is greater than 8, amorphous phase becomes favorable (Hu, et al., 2003; Lee and Gouma, 2012).

2.5.3.1.2. Solvent

Alcohol is used as a solvent in sol-gel system to dissolve the titanium alkoxide, that increases the condensation reaction efficiency by increasing the equivalent oxide content (equivalent oxide content = $n_{TiO_2}/n_{Ti(OR)_4}$). Further studies covered the effect of the type of alcohol to be used. Using lower chain of alcohols (i.e. ethanol rather than butanol) yields higher equivalent oxide content because of higher degree of the polymerization (Yoldas, 1986).

Ethanol content of alkoxide solution has major influence on kinetics of hydrolysis, propagation and nucleation reaction. Using excess ethanol results in a decreased alkoxide concentration that causes a decrease in the rate of these chemical reactions, which finalizes with production of close-packed

agglomerates with lower open porosity. Moreover, highly cross-linked particles with a spherical shape are produced. Decreasing the ethanol content increases the rates of both hydrolysis (monomer formation) and condensation (polymer formation) reactions and gives more open porosities. Also, products are open and linear structures with low skeletal densities (Bartlett, et al., 1990).

2.5.3.1.3. Acid

Acetic acid addition directly affects the reactivity of the metal alkoxide, which covers the rate of condensation reaction. Moreover, the rate of crystallization of anatase is determined by the acetic acid addition, since it is added as a nucleating agent to the solution (Venz, et al., 1998).

2.5.3.1.4. Water/Metal Alkoxide (Metal precursor) Ratio (R Ratio)

At sol-gel process, rate of the reactions are limited by the diffusion of the atoms. As water/metal oxide ratio increases, atomic mobility increases (Yoldas, 1986). Reduction in the gelation time is observed with increasing R ratio (Li, et al., 2004). In addition, high water content means more space for $[\text{TiO}_6]^{n+}$ units to have more regular arrangement which enables long range ordered structure (Chen, et al., 2009).

Increase of the R ratio results in a decrease in brookite content; and a decrease in anatase particle size and crystallite size (Isley and Penn, 2008). High R ratios mainly promote the hydrolysis reactions, which favor the nucleation rather than particle growth (Wang and Ying, 1999). Furthermore, in high water content, macromolecular networks form too fast that result in low interconnectivity between. In low water content network formation is slow and structure is more close-packed and denser (Lee and Gouma, 2012).

Effect of viscosity on the nucleation kinetics of the particles is expressed with Equations 2.13- 2.16.

$$\Delta G^* = 16\pi\gamma^3 / 3\Delta G_v^2 \quad \text{Eq. 2.13.}$$

$$D = kT / 3\pi r\eta = \omega r^2 \quad \text{Eq. 2.14.}$$

$$N = \omega C_0 \exp\{-\Delta G^* / kT\} \quad \text{Eq. 2.15.}$$

$$N = kTC_0 \exp\{-(16\pi\gamma^3 / 3\Delta G_v^2) / kT\} / 3\pi r^3 \eta \quad \text{Eq. 2.16.}$$

Free energy necessary for a nuclei formation, ΔG^* , is given in Equation 2.13 where γ is surface energy of the crystal, ΔG_v is the free energy required per unit volume from liquid to newly formed solid particle formation. Diffusivity of the atoms in solution is given in Equation 2.14 where k is Boltzmann constant, r is the radius of spherical particle, η is the viscosity of the medium (for sol-gel process viscosity of the solution), ω is the jumping frequency. C_0 in Equation 2.15 stands for the density of molecules. N is the nucleation rate in Equation 2.15. A new equation (Equation 2.16) can be derived with the combination of all these three equations at which k , T , π , and γ are the constants while C_0 , ΔG_v , r , ω , and η are variables.

2.5.3.1.5. Drying Conditions

Drying temperature has an effect on TiO_2 nanopowders. Removal of remaining water and alcohols take place at drying stage. As the drying temperature decreases, energy required for anatase to rutile transformation increases, which leads to hindering of this transformation. Final crystallite sizes become smaller. Also, drying temperature can affect the preferred growth orientation of anatase and rutile (Mohammadi, et al., 2008).

2.5.3.1.6. Calcination Regime

Removal of organics and finalization of crystallization take place at this stage. Calcination also, affects the agglomeration, phase transformation, and microstructure (Su, et al., 2004). Below 500°C rutile phase does not seen and crystals do not grow rapidly. However, after 500°C rutile phase is observed and crystals grow faster. Since the energy required for atoms to leave the matrix and attach itself to a growing phase is high, these mechanisms are not too active below 500°C (Li, et al., 2004). However, there are some other parameters that increase the transformation affinity such as particle size and specific surface area (Hu, et al., 2003). All of the parameters must be optimized to have the best photocatalytic activity in the system.

In this thesis work, R ratio and calcination regime for sol-gel synthesis were taken as variable parameters for the synthesis of TiO₂ powders. Then, the optimized conditions were used for the B and Zr doped TiO₂ powders.

CHAPTER 3

EXPERIMENTAL PROCEDURE

3.1. Powder Synthesis

Undoped, B doped, Zr doped, B and Zr co-doped TiO₂ powders were synthesized through sol-gel process. Tetraethyl orthotitanate (TEOT, [Ti(OC₂H₅)₄]) supplied from Merck was used as titanium precursor for all of powders. Glacial acetic acid supplied from Merck was used as catalyst. Boric acid (H₃BO₃) was used as boron source while zirconium acetylacetonate [Zr(C₅H₇O₂)₃] was used as zirconium source for doping purpose. Both chemicals were supplied from Sigma-Aldrich. Ethanol (99.5% pure) purchased from Sigma-Aldrich was used as a solvent. Water was distilled water provided from a water distiller (Progard TS2, Millipore S.A.S. Water Purification Systems). All of the chemicals were analytical grade and used in the form they were received without any further purification.

During powder preparation of undoped TiO₂ powders, a beaker of 400 ml was used for mixing medium of the chemicals of appropriate amount. A magnetic stirrer bar stirred the chemicals magnetically during mixing. Stirring was done at a speed of 500 rpm for 15 min for each sample. In the preparation of B or Zr doped powders two beakers were occupied. One was for titanium precursor, the other one is for the precursor of doping agent. Again, magnetic stirring was applied for mixing the chemicals at 500 rpm for 15 min for each sample. B and Zr co-doped powders were prepared by using three beakers. One is for titanium precursor, second one was for boron precursor, and the third one was for zirconium precursor. Magnetic stirring was applied for mixing the chemicals at 500 rpm for 15 min for each sample. Synthesis of undoped, B doped, Zr doped,

B and Zr co-doped TiO₂ powders are explained in detail in the following subsections.

3.1.1. Synthesis of Undoped TiO₂ Powders

Synthesis of undoped TiO₂ powders by sol-gel process began through preparation of different mother solutions according to mole of water / mole of TEOT ratio. Hereafter, water/TEOT mole ratio is named as R ratio. The mother solutions for R ratio of 1, 3, 5, 10, 30, and 50 were prepared by mixing certain amounts of TEOT, glacial acetic acid, ethanol, and water. The amount of chemicals needed for the preparation of mother solutions used for the synthesis of the undoped TiO₂ powders is presented in Table 3.1.

Table 3.1. Amount of chemicals needed for the preparation of mother solutions used for the synthesis of the undoped TiO₂ powders.

Solution Name	R ratio	TEOT (g)	Ethanol (ml)	Water (g)	Glacial Acetic Acid (ml)
R1	1	29.65	39.00	2.34	13.00
R3	3	27.37	36.00	6.48	12.00
R5	5	25.09	33.00	9.90	11.00
R10	10	22.81	30.00	18.00	10.00
R30	30	20.53	27.00	48.60	9.00
R50	50	15.97	21.00	63.00	7.00

The preparation of the mother solutions began first by pouring the necessary amount of ethanol into the beaker. Then, the necessary amount of TEOT was added onto ethanol dropwise using a burette while continuous magnetic stirring.

Next, required amount of distilled water was added to establish certain value of R ratio in the solution. After that, glacial acetic acid was added while magnetic stirring continues. Finally, with addition of all ingredients the solution was magnetically stirred at 500 rpm continuously for 15 min in order to obtain a homogeneous mother solution. After magnetic stirring, the pH and viscosity of the mother solution were measured and noted. The mother solutions prepared for R ratio of 1, 3, 5, and 10 turned into sols that were kept standing in the room temperature until they set to gels. The mother solutions prepared for R ratio of 30 and 50 did not form gels when they were kept standing in the room temperature for a few days. They formed colloidal suspensions from which particles precipitated and collected at the bottom of the beaker. The viscosity of the sols and suspensions were measured for few more times during standing in the room temperature. The xerogels and precipitates were transferred to an oven at 80°C and held there for 24 h for drying. After drying the xerogels and precipitates TiO₂ powders were obtained. The dried powders were calcined through a regulated heat treatment shown in Figure 3.1 at temperatures of 300, 400, and 500°C for 1, 2, and 3 h for the crystallization. The calcination was performed at the heating rate of 5°C/min up to maximum temperature. Flowchart of experimental procedure for the synthesis of undoped TiO₂ powders produced with R ratio of 10 is shown in Figure 3.2.

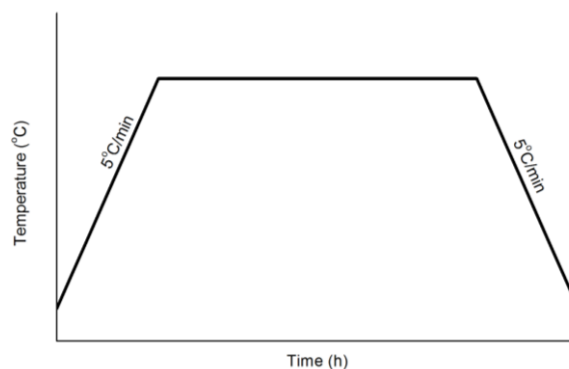


Figure 3.1. Schematic heat treatment procedure

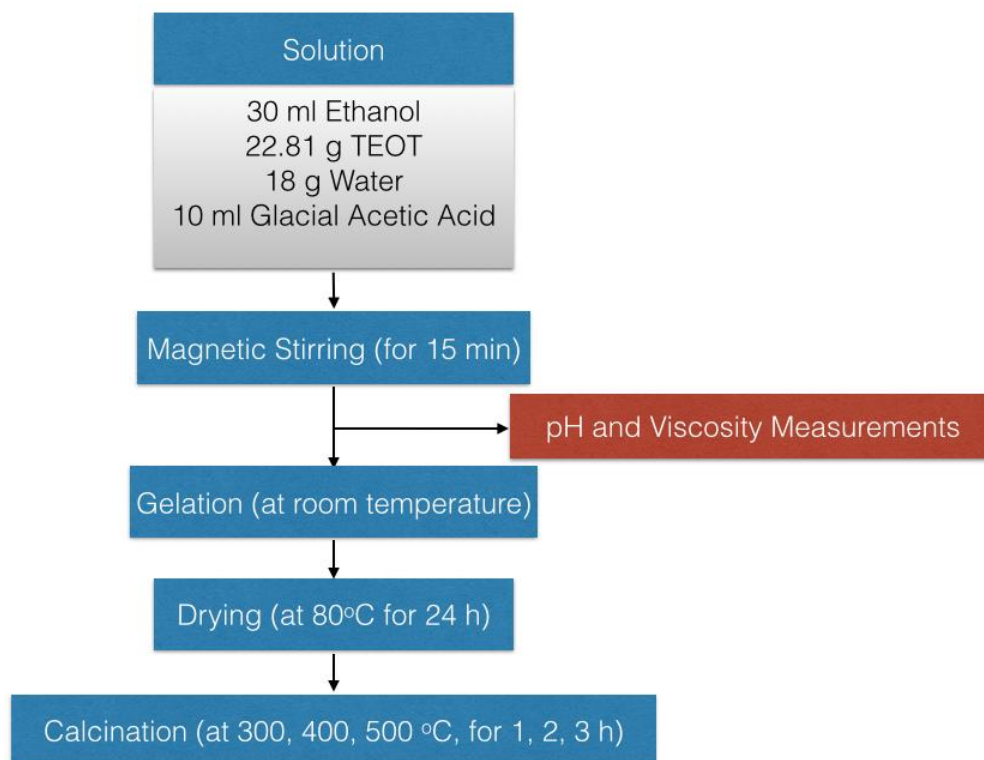


Figure 3.2. Flowchart showing the experimental procedure for the synthesis of undoped TiO_2 powder for R ratio of 10.

The synthesized TiO_2 powders were named regarding the R ratio, calcination temperature, and calcination time as $R_x T_0t$. Where x is for the numerical value of R ratio, T is for the first integer of the calcination temperature in degree celcius ($^{\circ}\text{C}$), and t is the calcination time in hour. For instance, the powder synthesized for R ratio of 1 and calcined at 400°C for 1 h was labelled R1 401. The label name of the undoped TiO_2 powders and their R ratio, calcination temperature, and calcination time are given in Table 3.2.

Table 3.2. The label name of the undoped TiO₂ powders, their R ratio and calcination regime.

Undoped TiO₂ Powder	R ratio	Calcination Temperature (°C)	Calcination Time (h)
R1	1	As-dried	-
R3	3	As-dried	-
R5	5	As-dried	-
R10	10	As-dried	-
R30	30	As-dried	-
R50	50	As-dried	-
R1 301	1	300	1
R1 302	1	300	2
R1 303	1	300	3
R3 301	3	300	1
R3 302	3	300	2
R3 303	3	300	3
R5 301	5	300	1
R5 302	5	300	2
R5 303	5	300	3
R10 301	10	300	1
R10 302	10	300	2
R10 303	10	300	3
R30 301	30	300	1
R30 302	30	300	2
R30 303	30	300	3
R50 301	50	300	1
R50 302	50	300	2
R50 303	50	300	3
R1 401	1	400	1
R1 402	1	400	2
R1 403	1	400	3
R3 401	3	400	1
R3 402	3	400	2

Table 3.2. (cont'd)

R3 403	3	400	3
R5 401	5	400	1
R5 402	5	400	2
R5 403	5	400	3
R10 401	10	400	1
R10 402	10	400	2
R10 403	10	400	3
R30 401	30	400	1
R30 402	30	400	2
R30 403	30	400	3
R50 401	50	400	1
R50 402	50	400	2
R50 403	50	400	3
R1 501	1	500	1
R1 502	1	500	2
R1 503	1	500	3
R3 501	3	500	1
R3 502	3	500	2
R3 503	3	500	3
R5 501	5	500	1
R5 502	5	500	2
R5 503	5	500	3
R10 501	10	500	1
R10 502	10	500	2
R10 503	10	500	3
R30 501	30	500	1
R30 502	30	500	2
R30 503	30	500	3
R50 501	50	500	1
R50 502	50	500	2
R50 503	50	500	3

3.1.2. Synthesis of Doped TiO₂ Powders

The B doped, Zr doped, and B and Zr co-doped TiO₂ powders were synthesized for R ratios of 50 while B and Zr doping additions were changed. All of the doped TiO₂ powders were calcined at temperatures of 300 and 500°C for 1 h.

3.1.2.1. Synthesis of B Doped TiO₂ Powders

The B doped TiO₂ powders were synthesized by adding 2, 3, and 4 weight percentage (wt%) of B through addition of necessary amount of boric acid to the mother solution. In the synthesis process of B doped TiO₂ powders, initially two solutions (Solution A and Solution B) were prepared separately. The amount of chemicals needed for the preparation of the solutions used for the synthesis of the B doped TiO₂ powders is presented in Table 3.3.

Solution A was prepared for R ratio of 50 through the procedure described in Section 3.1.1 with an exception that glacial acetic acid was not added. Solution B was prepared first by pouring 15.00 ml of ethanol to a beaker. Then, necessary amount of boric acid was added onto ethanol while continuous magnetic stirring. Next, 10.00 ml of glacial acetic acid was added dropwise using a burette while stirred. This solution was magnetically stirred for 15 min for the homogenization of the solution. Finally, Solution A and Solution B were mixed and magnetically stirred at 500 rpm continuously for 15 min in order to obtain a homogeneous solution from which B doped TiO₂ powders could be synthesized.

Table 3.3. Amount of chemicals needed for the preparation of the solutions used for the synthesis of B doped TiO₂ powders.

Chemicals		B doped TiO ₂ powder solution		
		R50-2B	R50-3B	R50-4B
Solution A	TEOT (g)	11.41	11.41	11.41
	Ethanol (ml)	15.00	15.00	15.00
	Water (g)	45.04	45.04	45.04
Solution B	Ethanol (ml)	15.00	15.00	15.00
	Glacial Acetic Acid (ml)	10.00	10.00	10.00
	Boric Acid (g)	0.94	1.42	1.90

After magnetic stirring, the pH and viscosity of the final solution were measured and noted. This solution did not form gel when it was kept standing in the room temperature for a few days. Instead, it formed colloidal suspension form which particles precipitated and collected at the bottom of the beaker. The viscosity of the suspension was measured during standing in the room temperature. The precipitates were transferred to an oven at 80°C and held there for 24 h for drying. After drying B doped TiO₂ powders were aimed to obtain. The dried powders were calcined at 300 and 500°C for 1 h for the crystallization. Flowchart of experimental procedure for the synthesis of 3 wt% B doped TiO₂ powder is shown in Figure 3.3.

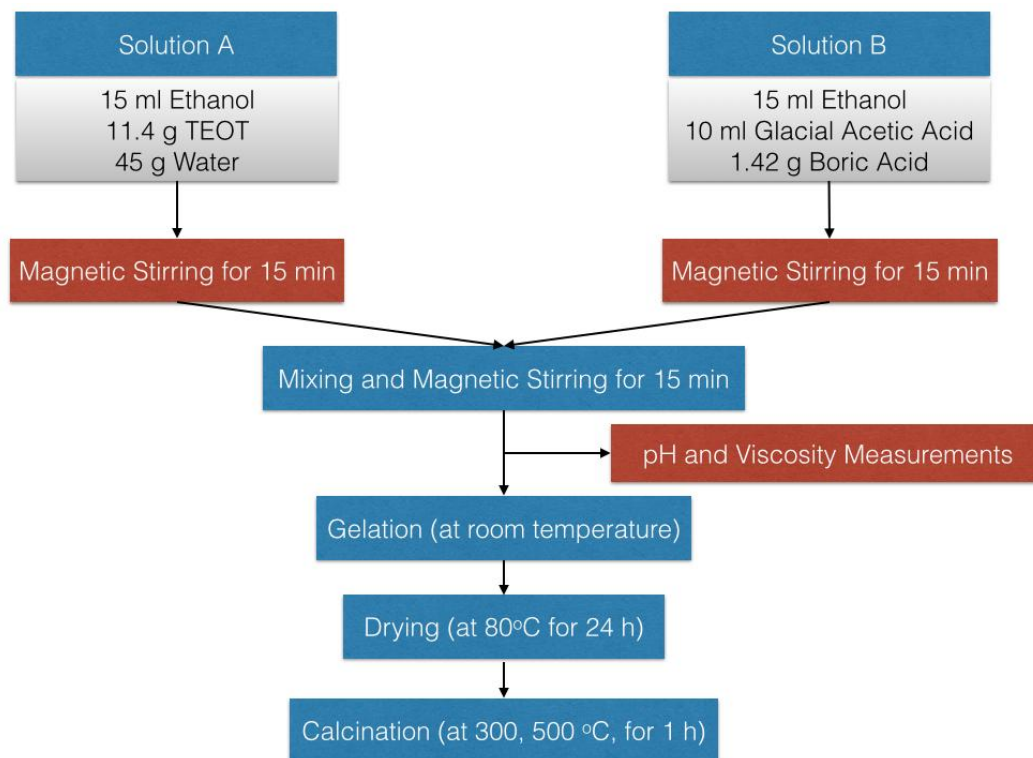


Figure 3.3. Flowchart showing the experimental procedure for the synthesis of the 3% B doped TiO_2 powder.

The B doped TiO_2 powders synthesized were named regarding the R ratio, calcination temperature, and calcination time as R50-yB-T0t. Where; y is the amount of boron doping in wt%, T is for the first integer of the calcination temperature in degree celcius, and t is the calcination time in h. For instance, label R50-2B-501 represents the powder synthesized by doping 2 wt% B doping for R ratio of 50, and calcined at 500 for 1 h. The label name of the B doped TiO_2 powders and their synthesis conditions are given in Table 3.4.

Table 3.4. Labelling of the B doped TiO₂ powders and their calcination regime.

B Doped TiO₂ Powder	R ratio	Boron Doping (wt%)	Calcination Temperature (°C)	Calcination Time (h)
R50-2B	50	2	As-dried	-
R50-3B	50	3	As-dried	-
R50-4B	50	4	As-dried	-
R50-3B-301	50	3	300	1
R50-2B-501	50	2	500	1
R50-3B-501	50	3	500	1
R50-4B-501	50	4	500	1

3.1.2.2. Synthesis of Zr Doped TiO₂ Powders

The Zr doped TiO₂ powders were synthesized by adding 5, 10, and 15 wt% Zr through addition of zirconium acetylacetonate to the mother solution. In the synthesis process of Zr doped TiO₂ powders, initially two solutions (Solution A and Solution C) were prepared separately. The amount of chemicals needed for the preparation of the solutions used for the synthesis of the Zr doped TiO₂ powders are presented in Table 3.5.

Solution A was prepared for R ratio of 50 through the procedure described in Section 3.1.1 with an exception that glacial acetic acid was not added. Solution C was prepared first by pouring 15.00 ml of ethanol to a beaker. Then, necessary amount of zirconium acetylacetonate was added onto ethanol while continuous magnetic stirring. Next, 10.00 ml of glacial acetic acid was added dropwise using a burette while stirred. This solution was magnetically stirred for 15 min for the homogenization of the solution. Finally, Solution A and Solution C were mixed and magnetically stirred at 500 rpm continuously for 15 min in order to obtain a homogeneous solution from which Zr doped TiO₂ powders could be synthesized.

Table 3.5. Amount of chemicals needed for the preparation of the solutions used for the synthesis of Zr doped TiO₂ powders.

Chemicals		Zr doped TiO ₂ powder solution		
		R50-5Zr	R50-10Zr	R50-15Zr
Solution A	TEOT (g)	11.41	11.41	11.41
	Ethanol (ml)	15.00	15.00	15.00
	Water (g)	45.04	45.04	45.04
Solution C	Ethanol (ml)	15.00	15.00	15.00
	Glacial Acetic Acid (ml)	10.00	10.00	10.00
	Zirconium Acetylacetonate (g)	2.24	4.74	7.54

After magnetic stirring, the pH and viscosity of the final solution were measured and noted. This solution did not form gel when it was kept standing in the room temperature for a few days. Instead, it formed colloidal suspension form which particles precipitated and collected at the bottom of the beaker. The viscosity of the suspension was measured for few more times during standing in the room temperature. The precipitates were transferred to an oven at 80°C and held there for 24 h for drying. After drying Zr doped TiO₂ powders were aimed to obtain. The dried powders were calcined at 300 and 500°C for 1 h for the crystallization. Flowchart of experimental procedure for the synthesis of 10 wt% Zr doped TiO₂ powder is shown in Figure 3.4.

The Zr doped TiO₂ powders synthesized were named regarding the R ratio, calcination temperature, and calcination time as R50-zZr-T0t. Where; z is the amount of zirconium doping in wt%, T is for the first integer of the calcination temperature in °C, and t is the calcination time in h. For instance, label R50-5Zr-501 represents the powder synthesized by doping 5 wt% Zr for R ratio of 50, and

calcined at 500°C for 1 h. The label name of the Zr doped TiO₂ powders and their synthesis conditions are given in Table 3.6.

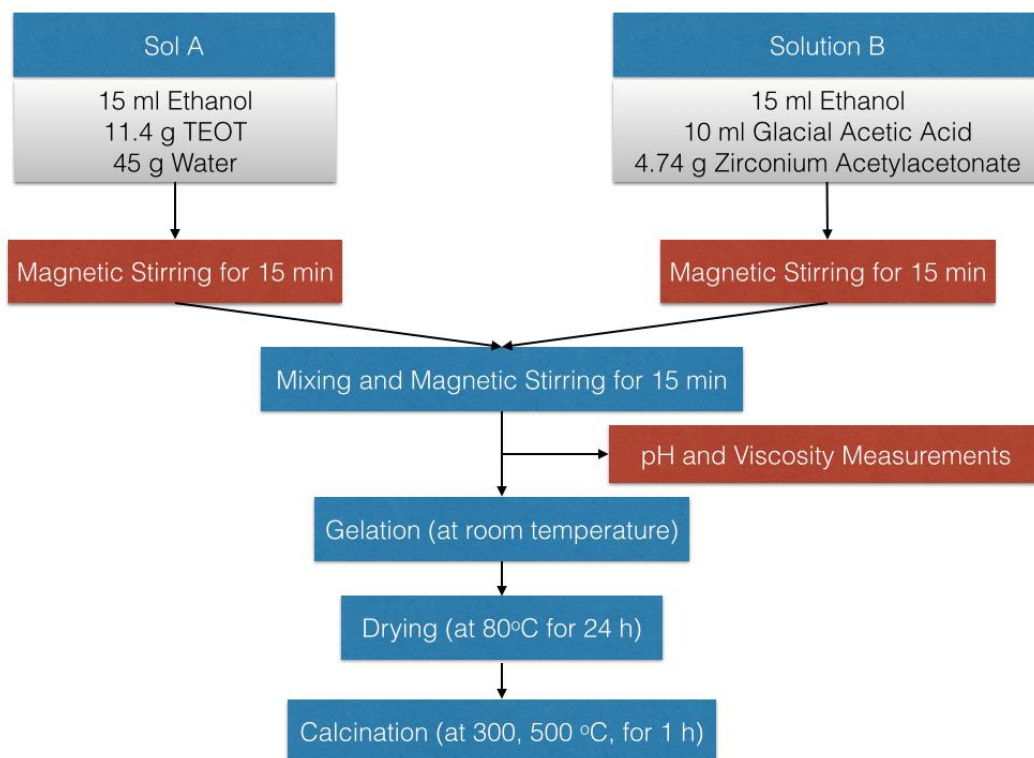


Figure 3.4. Flowchart showing the experimental procedure for the synthesis of the 10 wt% Zr doped TiO₂ powder.

Table 3.6. Labelling of the Zr doped TiO₂ powders and their calcination regime.

Zr Doped TiO₂ Powder	R ratio	Zirconium Doping (wt%)	Calcination Temperature (°C)	Calcination Time (h)
R50-5Zr	50	5	As-dried	-
R50-10Zr	50	10	As-dried	-
R50-15Zr	50	15	As-dried	-
R50-10Zr-301	50	10	300	1
R50-5Zr-501	50	5	500	1
R50-10Zr-501	50	10	500	1
R50-15Zr-501	50	15	500	1

3.1.2.3. Synthesis of B and Zr Co-Doped TiO₂ Powders

The B and Zr co-doped TiO₂ powders were synthesized by adding 3 wt% B with addition of boric acid and 10 wt% Zr with addition of zirconium acetylacetonate to the mother solution. The selected percentage of the dopants was the percentage that each powder exhibited photocatalytically better performance relative to the other powders in each group. In the synthesis process of B and Zr co-doped TiO₂ powders, initially three solutions (Solution A, Solution B, Solution C) were prepared separately. The amount of chemicals needed for the preparation of the solutions used for the synthesis of the B and Zr co-doped TiO₂ powders is presented in Table 3.7.

Table 3.7. Amount of chemicals needed for the preparation of the solutions used for the synthesis of B and Zr co-doped TiO₂ powders.

Chemicals		B and Zr co-doped TiO ₂ powder solution
		R50-3B-10Zr
Solution A	TEOT (g)	11.41
	Ethanol (ml)	15.00
	Water (g)	45.04
Solution B	Ethanol (ml)	15.00
	Glacial Acetic Acid (ml)	10.00
	Boric Acid (g)	1.42
Solution C	Ethanol (ml)	7.50
	Glacial Acetic Acid (ml)	5.00
	Zirconium Acetylacetonate (g)	2.37

Solution A was prepared for R ratio of 50 through the procedure described in Section 3.1.1 with an exception that glacial acetic acid was not added. Solution B was prepared through the procedure described in Section 3.1.2.1. This solution was magnetically stirred for 15 min for the homogenization before it is added onto Solution A. Solution C was prepared through the procedure described in Section 3.1.2.2. This solution was magnetically stirred for 15 min for the homogenization before it is added onto Solution A. Finally, the resultant solution obtained by mixing Solution A, Solution B, and Solution C, was mixed and magnetically stirred at 500 rpm continuously for 15 min in order to obtain a

homogeneous solution from which B and Zr co-doped TiO₂ powders could be synthesized.

After magnetic stirring, the pH and viscosity of the final solution were measured and noted. This solution did not form gel when it was kept standing in the room temperature for a few days. Instead, it formed colloidal suspension form which particles precipitated and collected at the bottom of the beaker. The viscosity of the suspension was measured for few more times during standing in the room temperature. The precipitates were transferred to an oven at 80°C and held there for 24 h for drying. After drying B and Zr co-doped TiO₂ powders were aimed to obtain. The dried powders were calcined at 300 and 500°C for 1 h for the crystallization. Flowchart of experimental procedure for the synthesis of B and Zr co-doped TiO₂ powders is shown in Figure 3.5.

The B and Zr co-doped TiO₂ powders synthesized were named regarding the calcination temperature, and calcination time as R50-3B-10Zr-T0t. Where T is for the first integer of the calcination temperature in °C, and t is the calcination time in h. For instance, label R50-2B-10Zr-501 represents the powder synthesized by doping 2 wt% B and 10 wt% Zr for R ratio of 50, and calcined at 500 for 1 h. The label name of the B and Zr co-doped TiO₂ powders and their synthesis conditions are given in Table 3.8.

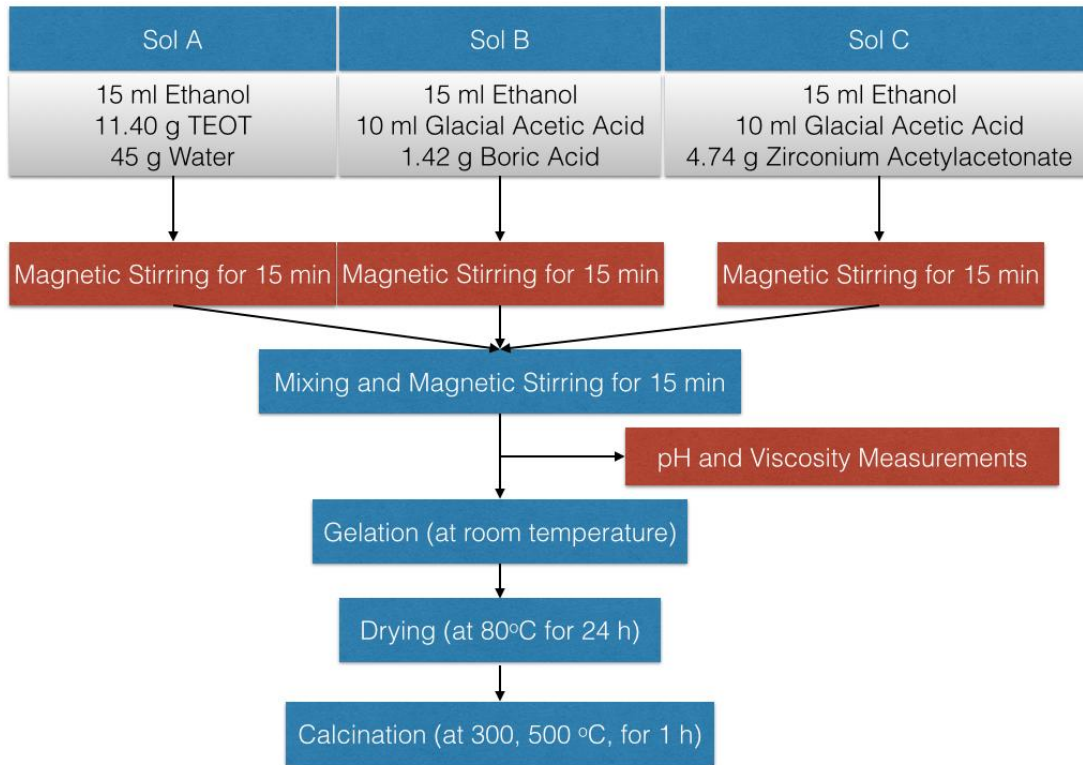


Figure 3.5. Flowchart showing the experimental procedure for the synthesis of the 3 wt% B and 10 wt% Zr co-doped TiO₂ powder for R ratio of 10.

Table 3.8. Labelling of the the B and Zr co-doped TiO₂ powders and their calcination regime.

B and Zr co-doped TiO₂ Powder	R ratio	Boron Doping (wt%)	Zirconia Doping (wt%)	Calcination Temperature (°C)	Calcination Time (h)
R50-3B-10Zr	50	3	10	As-dried	-
R50-3B-10Zr-301	50	3	10	300	1
R50-3B-10Zr-501	50	3	10	500	1

3.2. Powder Characterization

3.2.1. pH Measurement

The pH of the mother solutions was measured after homogenization via 15 min of magnetic stirring. The measurement was done by using universal pH-indicator strips in the pH range of 0 – 14. The strips were supplied from Merck.

3.2.2. Viscosity Measurement

Viscosity of the initial mother solutions and sols acquired from the mother solutions was measured occasionally for a few times during gelation until total gelation was attained. Brookfield DV-III Ultra Rheometer was employed for viscosity measurements. Viscosity values were read when torque percentage is around $50 \pm 2\%$.

3.2.3. X-Ray Diffraction (XRD) Analysis

X-Ray diffraction analyses were made to confirm the amorphous state of the gels, to identify the crystalline species occasionally precipitated during aging of the gels, and to identify the crystalline phases developed during heat-treatment of the undoped, B doped, Zr doped, B and Zr co-doped TiO_2 powders. A Rigaku-Geigerflex D/MAK/B X-ray diffractometer was employed to get XRD data. Cu K_α radiation with a wavelength of 1.54056 \AA was used for the x-ray source. Each powder was scanned in a 2θ range from 15° to 75° with $2^\circ/\text{min}$ rate continuously with an accelerating voltage of 40 kV and applied current of 40 mA. XRD data was analyzed by using Rigaku 4.2 Qualitative Analyses program.

Diffractograms and histograms were constructed by CMPR (developed by B. Toby, NIST, 2005). Rietveld Analysis was done by GSAS (General Structure Analysis System [developed by R.B. von Dreele and A.C. Larson, University of California, 2001]) for the Rietveld Refinement of lattice parameter, atomic

position determination and crystallite size calculations. The parameters used for the refinement are tabulated in Table 3.9.

Table 3.9. Initial rietveld fitting parameters and constant parameters

Crystal Structure	Tetragonal	
Space Group (Hahn, 2005)	I4 ₁ /amd	
Instrumental Broadening	GU	33.54
	GV	-17.90
	GW	11.41
Atomic Positions (Manik, et al., 2003)	Ti	(0.0000, 0.7500, 0.1250)
	O	(0.0000, 0.7500, 0.3333)
	Zr	(0.0000, 0.7500, 0.1250)
	B	(0.0000, 0.7500, 0.3333)
Lattice Parameter (Weirich, et al., 2000)	a=b (Å)	3.7867
	c (Å)	9.5149

Linear parts of the characteristic peak were interpolated to the background of the XRD diffractogram. The area of the formed triangle was calculated and divided to the area of the characteristic peak. The result was multiplied with 100 crystallinity percentage of the synthesized powders were calculated.

3.2.4. Scanning Electron Microscope (SEM) Analysis

Nova NANOSEM 430 was occupied for surface morphology examination and qualitative particle size analysis of the powders. A 15 kV accelerating voltage and 3.5 spot size were applied during imaging of the powder samples. Imaging was done at low (2500 – 20000), medium (20000- 80000), and high (\geq 80000) magnifications. Prepared samples were coated with platinum (Pt) of 8-10 nm thickness.

3.2.5. Diffuse Reflectance Spectra (DRS) Analysis

Diffuse reflector apparatus of UV-Vis Spectrophotometer (Scinco S-3100) was used for the diffuse reflectance measurements. DRS analyses were done to see whether visible light activity in powders was achieved or not. White blank measurement was done according to USRS-99-010 standard. The percent reflection versus wavelength graph was transformed by Kubelka-Munk method to $[eV]^{(1/2)}$ vs $[eV]$ graph by using Equations 3.1-3.3. Band gap energy of the powder was calculated by extrapolating the mid-section of the graph –that was obtained after transformation- to x-axis.

$$K = \left\{ (1-R)^2 \right\} / 2R \quad \text{Eq. 3.1.}$$

$$\text{Energy}[eV]^{(1/2)} = (K * h * g)^{(1/2)} \quad \text{Eq. 3.2.}$$

$$\text{Energy}(x\text{axis}) [eV] = h * c / \lambda \quad \text{Eq. 3.3.}$$

3.3. PHOTOCATALYTIC ACTIVITY MEASUREMENT

The photocatalytic activity of the TiO₂ powders was evaluated in terms of the degradation of aqueous methylene blue (MB) solution under ultraviolet (UV) light illumination. A fully dark wooden box preventing the passage of daylight through the suspension prepared by mixing the MB solution and TiO₂ powder was used for the photocatalytic activity tests. MB aqueous solution was prepared by dissolving 0.01 g MB powder in 1 l of deionized water. Initial concentration of MB solution was 10 mg/l. A 50 ml of MB solution was mixed with 50 mg of TiO₂ powder to prepare the suspension. Prior to the test, the suspension was stirred magnetically at 500 rpm for 30 min in dark to reach adsorption/desorption equilibrium of MB. At the end of first 30 min, a sample of 4 mL was taken from the suspension by means of syringe filters (Millex Millipore, 0.22 μm). Then, a clear powder free solution of MB was transferred to UV-Vis Spectrophotometer

(Scinco S-3100) to measure the photocatalytic activity at the wavelength of 664 nm. After the first measurement, the UV lamp was turned on and changes in absorption under UV light were measured. A 100W UV lamp (UVP Co.) was used for the UV light source at the wavelength of 365 nm. Same procedure was applied after 30, 60, and 90 min UV light illumination of the suspension. UV-Vis absorption was measured between 200-800 nm. The absorption changes and absorption percentage were calculated with respect to illumination time using Equation 3.4.

$$\text{Degradation Ratio (\%)} = [(I_{\text{dark}} - I) * 100] / I_{\text{dark}} \quad \text{Eq. 3.4.}$$

Where;

I= Intensity at 664 nm at 30, 60, and 90 min UV radiation time.

I_{dark}= Intensity at 664 nm after adsorption/desorption equilibrium (30 min in dark).

The flowchart showing the photocatalytic activity measurement procedure of the TiO₂ powders is given in Figure 3.6.

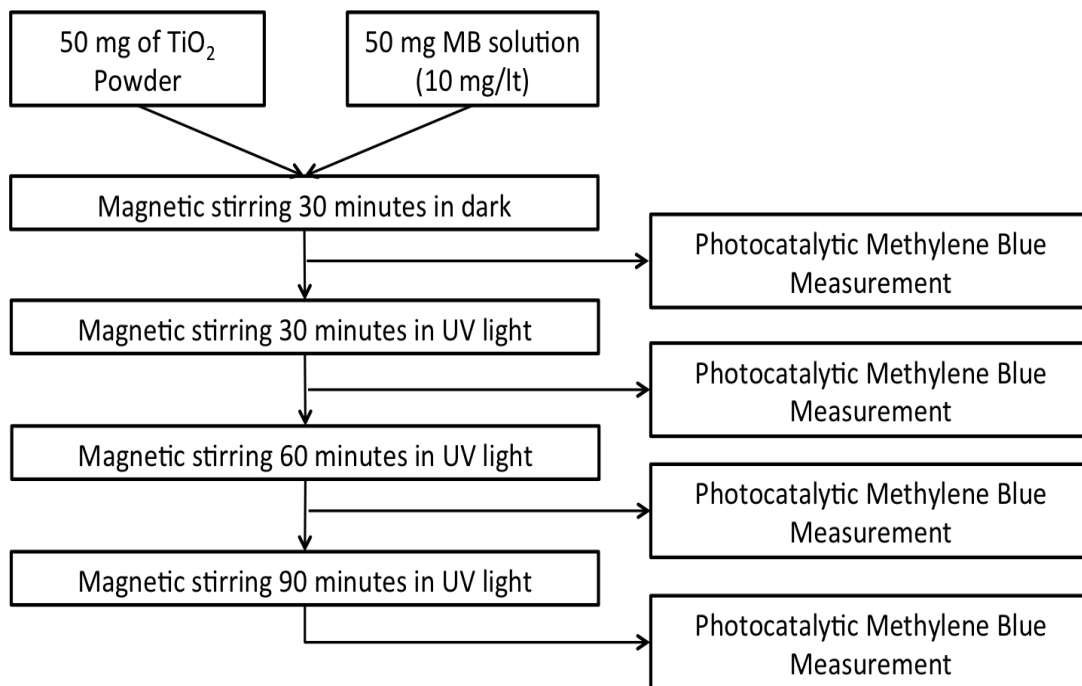


Figure 3.6. The flowchart showing the experimental procedure for the MB degradation measurement of the powders.

The TiO₂ powders with optimum structural, morphological, band gap energy features, and highest MB degradation were tested in daylight. Three measurements were done for each undoped, doped, and co-doped samples. At first MB solution was tested before the powders were added and the others were after exposing the MB solution to daylight for 24 and 48 h.

CHAPTER 4

RESULTS AND DISCUSSION

4.1. General Remarks

In this part of the thesis, the data gathered from the experimental study were presented and the results were discussed.

Six different (1, 3, 5, 10, 30, and 50) initial solution compositions with respect to R ratio ($R = n_{\text{water}}/n_{\text{TEOT}}$) and three different calcination temperatures (300, 400, and 500 °C) for three different calcination times (1, 2, and 3 h) were applied for the synthesis of undoped TiO₂ powders. For the B doped and Zr doped TiO₂ powders, R ratio of 50 and two different calcination temperatures (300 and 500 °C) were applied. Sintering time was kept constant for 1 h. B doping was done for 2, 3, and 4 weight percentage (wt%) while Zr doping was done for 5, 10, and 15 wt%. Lastly, for the B and Zr co-doped TiO₂ powders, R ratio of 50 and two different calcination temperatures (300 and 500 °C) for 1 h were applied. B doping was done only for 3 wt% B while Zr doping was done only for 10 wt% in the B and Zr co-doped TiO₂ powders.

4.2. Synthesis Of Undoped TiO₂ Powders

The undoped TiO₂ powders were synthesized through the experimental procedure described in Section 3.1.1. The undoped TiO₂ powders appeared in white color before (in as-dried form) and after calcinations (in calcined form), except for powders R1 and R3 calcined at 300°C. Dark yellowish and light brownish colors were observed in 300 series of powders R1 and R3. Gorska, et al., 2008 and Colmenares, et al., 2006 reported such coloring in undoped TiO₂

powders calcined at low temperatures. Obtained powders showed liquid like flow upon shaking the container.

The mother solutions prepared for R ratio equal to or smaller than 10 formed gels after aging. In contrast, solutions having R equal to or greater than 30 did not form gel when they were kept standing in the room temperature for a few days. They formed colloidal suspensions from which particles precipitated. The observed behavior is in agreement with that reported by Carp, et al., 2004 and Watson, et al., 2003 who stated that utilization of metal alkoxides as starting material involves the formation of a TiO_2 sols or gels or precipitates by hydrolysis and condensation (with polymer formation) of titanium alkoxides. The reason why two different powders synthesization routes was comprehended upon increasing water content was attributed to the changes in pH and viscosity of the initial mother solution.

Increasing water content in the initial mother solution decreases the concentration of the H_3O^+ and OH^- ions and leads pH to decrease. Carp et al., 2004 and Livage et al., 1988 confirmed that with increasing acidity hence decreasing pH hydrolysis rates increases. In other words, solutions with low pH values show almost no condensation stage at all. Then, polymerization does not happen, so does gelation. Yoldas, 1986 and Su et al., 2004 emphasized the importance of having partial hydrolysis for condensation to take place and concluded that condensation is a necessity for the polymerization stage to take place. Gel formation occurs upon aging of the polymerized structure.

The increase in water content of the solution decreases the viscosity, which results in a higher atomic mobility that finalizes with easier development of crystalline structure in the system by increasing nucleation rate (Busch et. al. 1998). The lower viscosity allows better mobility of the atoms in the solution hence helps diffusion that favors crystallization process rather than gelation process. Wang and Ying, 1999, reported that as water amount in the solution increases nucleation begins to suppress growth mechanism, which is probably

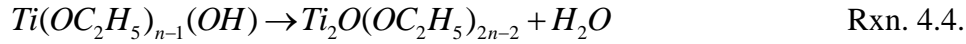
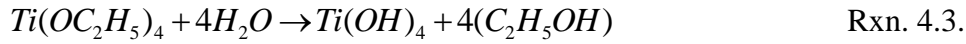
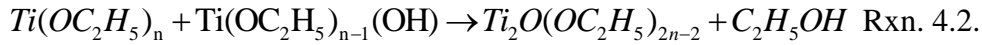
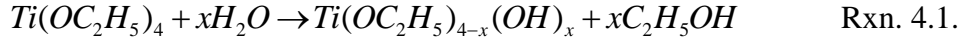
the result of the increasing number of possible nucleation sites for TiO_2 molecules.

As stated in Section 2.5.3.1.4 amount of water affects all the nucleation and growth variables directly. Minimum and maximum R ratios in the solutions prepared are 1 and 50, respectively. A large disparity in water content will cause changes in all these variables as well as in viscosity of the solution. However, the other variables would not have that much effect over the system as viscosity would. In other words, effects of the other variables on the nucleation kinetics of the particles due to the change in water content might be disregarded as compared to changes resulted by viscosity difference.

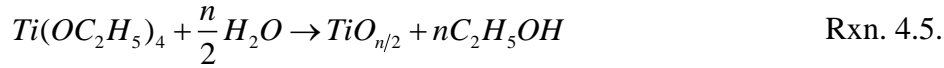
Partial crystallization took place in powders R5, R10, R30, and R50 in as-dried form because the atomic mobility in the mother solutions having R ratio greater than 5 is much higher than the solutions having R ratio of 1 and 3. Also, the number of free bonds in these solutions is lesser than that in solutions R1 or R3. Therefore crystal growth is more difficult for the powders having R ratio greater than 5. Moreover, the powders having R ratio greater than 5 are thermodynamically much more stable as compared to those having R ratio 1 and 3. The instability will take a role as driving force for crystallization upon application of heat externally.

In the light of the information given above and direct observations of the solutions to form gels via alkoxide sol-gel process, the gelation stage of titanium precursor (TEOT) in ethanol solution could be interpreted as follows. At first, TEOT reacts with either residual water in ethanol or humidity in the air and partially hydrolyses to form $\text{Ti}(\text{OC}_2\text{H}_5)_{4-x}(\text{OH})_x$ species. Then, TEOT reacts with added water and further hydrolyses. Hydrolysis of TEOT leads to the formation of Ti-OH bonds and $\text{Ti}_2\text{O}(\text{OC}_2\text{H}_5)_3$ species. This process happens very rapid and almost finalizes after the mixing process. In the gelation stage, polymerization (condensation dehydration and dealcoholation) reactions occur. The OC_2H_5 group is removed easily from the precursor than OH group due to its higher activity for water. These reactions continue until $\text{Ti}(\text{OH})_4$ is formed. Finally,

condensation pulls the particles together into a compact form and build up the TiO₂ crystals (Chen, et al., 2009; Dogu, 2012; Li, et al., 2004; Yoldas, 1986). The reactions leading to the formation of the TiO₂ powders via polymeric sol-gel process is given below.



The overall reaction is assumed to take place as the one given below.



In the case of high water content, that is R equal to or greater than 30 in the initial mother solution, the gelation stage does not happen because of the rapid hydrolysis and absence of condensation stage. Instead precipitation of TiO₂ particles occurs. The formation of the TiO₂ powders via precipitation is believed to occur according to Reaction 4.5 given above.

4.3. Characterization Of Undoped TiO₂ Powders

4.3.1. pH Measurement

The results of the pH measurements of the initial solutions for different R ratios were listed in Table 4.1.

Table 4.1. pH values of the initial solutions for different R ratio.

Solution name	pH
R1	4~5
R3	4
R5	4
R10	3
R30	3
R50	3

It is apparent that increasing water content in the solution resulted in a slight decrease in pH value. The decrease in pH with increasing water content could be explained by means of Henderson-Hasselbalch equation (Po and Senozan, 2001).

$$pH = pK_a - \log([A^-]/[HA]) \quad \text{Eq. 4.1.}$$

where; K_a is acid dissociation constant, $[HA]$ is the molar concentration of the undissociated weak acid, $[A^-]$ is the molar concentration of this acid's conjugate base. Increasing water content decreases the concentration of the H_3O^+ and OH^- ions in the solution. A decrease in the concentration of the H_3O^+ and OH^- ions causes a change in equilibrium that favors pH to decrease.

4.3.2. Viscosity Measurement

The viscosity of the initial solutions for different R ratio was measured to understand the effect of water content on the nucleation mechanism of the particles formed and the crystallization behavior of the powders. Viscosity is also an important parameter for nucleation kinetics of the particles formed. The data gathered from the viscosity measurements of the initial solutions were plotted with respect to setting time of the solutions at room temperature. The variation of the viscosity of the initial solutions with time is shown in Figure 4.1.

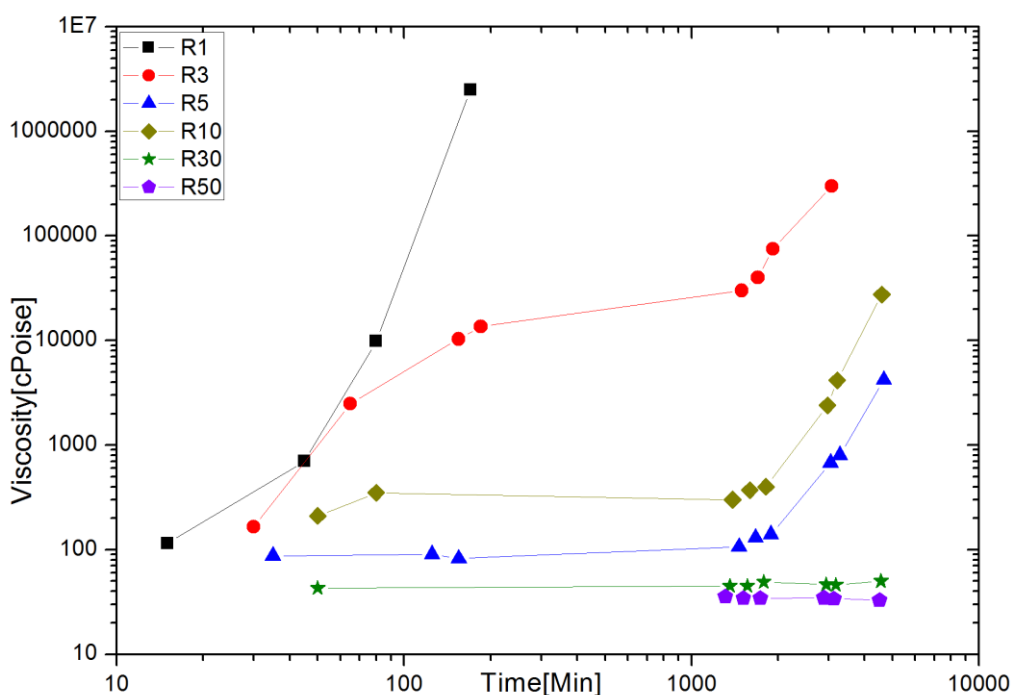


Figure 4.1. Viscosity vs time graph for the solutions prepared for different R ratio.

It is clear that viscosity of the solutions R1, R3, R5, and R10 increased with time while that of the solutions R30 and R50 did not change much after standing a few days at room temperature. Viscosity of the solutions gets lower as the water content of the solution is increased. There is a disorder between the solutions R5 and R10. For a given setting time, viscosity of solution R10 was higher than solution R5. The measurements on different batch of solutions consistently

showed that viscosity of solution R5 was lower than solution R10. The reason why R5 has lower viscosity than R10 was not understood and could not be explained at the moment. Nevertheless it was attributed to the changes taking place in sol-gel reactions. Viscosity of the solution R1 was about 2500000 cP, whereas that of the solution R50 (which has the smallest viscosity values at a given setting time among all of the solutions prepared) was only 30 cP after 120 min setting time. The ratio of viscosity between the upper and lower limiting water content in the solutions that is, the solutions R1 and R50, was about five orders of magnitude. However no direct relation between the R ratio and viscosity could be deduced from the data gathered.

General remarks obtained in viscosity measurements are listed below:

- 1- Gelation stage of solution R1 finished in less than 3 h. Gelation of the other solutions took much more time, even days. The solutions R30 and R50 showed no gelation stage at all.
- 2- There is about five orders of magnitude difference between the viscosity of the solutions R1 and R50 after 120 min setting time. This causes a huge difference between both atomic mobility in the solutions and difference in the crystal properties of the powders obtained from the solutions.
- 3- Comparison of the solutions R30 and R50 with the other powders might not be very appropriate since they did not show gelation stage. The excess water amount in the solutions R30 and R50 was so high and pH was so low that, even if the synthesis conditions were the same, powder formation took place with precipitation rather than gelation.

4.3.3. X-Ray Diffraction (XRD) Analysis

The XRD patterns belonging to the undoped powders in as-dried form are shown in Figure 4.2. XRD analysis revealed that all powders are composed of anatase phase in as-dried form, except powders R1 and R3 which did not show any crystallinity. Similar results were reported in literature. For instance, Li et al., 2004, obtained totally amorphous TiO₂ powders for R of 3 in as-dried condition whereas, Mohammadi et al., 2008 noticed high amount of crystallinity in anatase crystals for R of 500 in as-dried form. Characterization of the phase is done by the characteristic anatase peak of (101) plane at 2θ of $\sim 25.3^\circ$ (JCPDS #21-1272). As expected from the viscosity results, increasing water content resulted in better crystallinity in the as-dried powders.

From the data obtained for as-dried powders percentage of crystallinity in the powders was calculated. The calculated crystallinity percentage values are listed in Table 4.2. Crystallinity analyses of as-dried powders revealed that with increasing R ratio crystallinity increases. These results are in a very good agreement with the publication of Chen et al., 2009. Increase in crystallinity percentage is generally as the result of low pH and low viscosity. Yet, getting high crystallinity in as-dried powders is important for low temperature synthesis (Chen, et al., 2009). Since, no high temperature calcination was required, number of mediums they can be applied to increases (i.e. wood, plastic) (Jung, et al., 2005; Chen, et al., 2009).

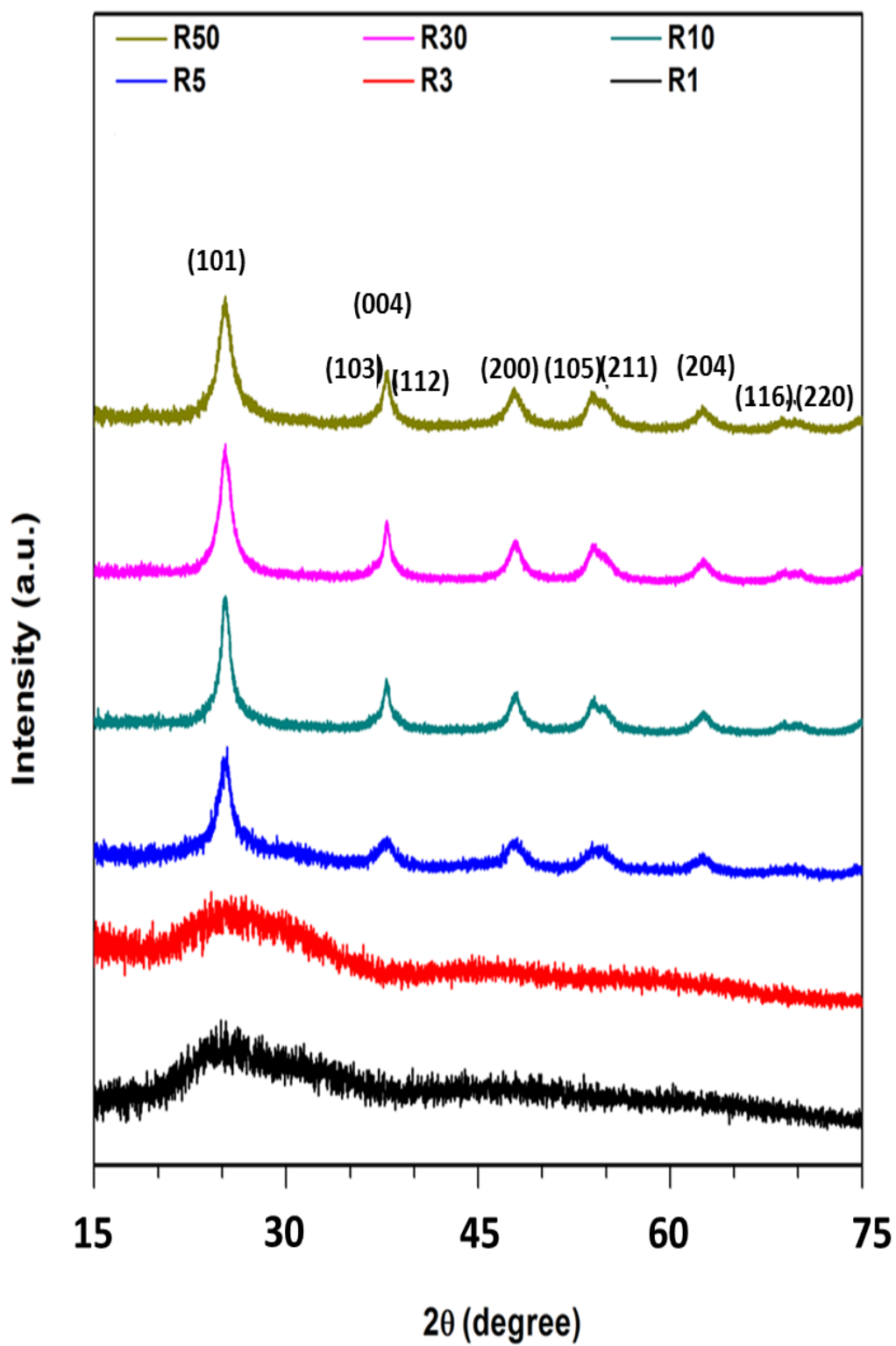


Figure 4.2. XRD patterns of the undoped TiO₂ powders in as-dried form.

Table 4.2. Percentage of crystallinity of the undoped TiO₂ powders in as-dried form.

Powder	Crystallinity %
R1 as-dried	~ 0
R3 as-dried	~ 0
R5 as-dried	57.62
R10 as-dried	67.62
R30 as-dried	69.77
R50 as-dried	70.44

The XRD patterns of the undoped TiO₂ powders calcined at 300°C, hereafter these powders were named as 300 series (301, 302, and 303) powders, revealed that irrespective of the calcination time all of these powders composed of only anatase crystals as seen in Figures 4.3-4.5. Characterization of the phase is done by the characteristic anatase peak of (101) plane at 2θ of $\sim 25.3^\circ$ (JCPDS #21-1272). No brookite or rutile formation was observed. Upon calcination at 300°C powders having R ratio equal to or greater than 5 completed their crystallization, while R1 and R3 were partially crystallized and crystallite sizes increased. Also, peak resolution increased but breadth decreased. Deconvolution of the peaks for (105) and (211), (116) and (220) planes took place for all powders except powders R1 and R3.

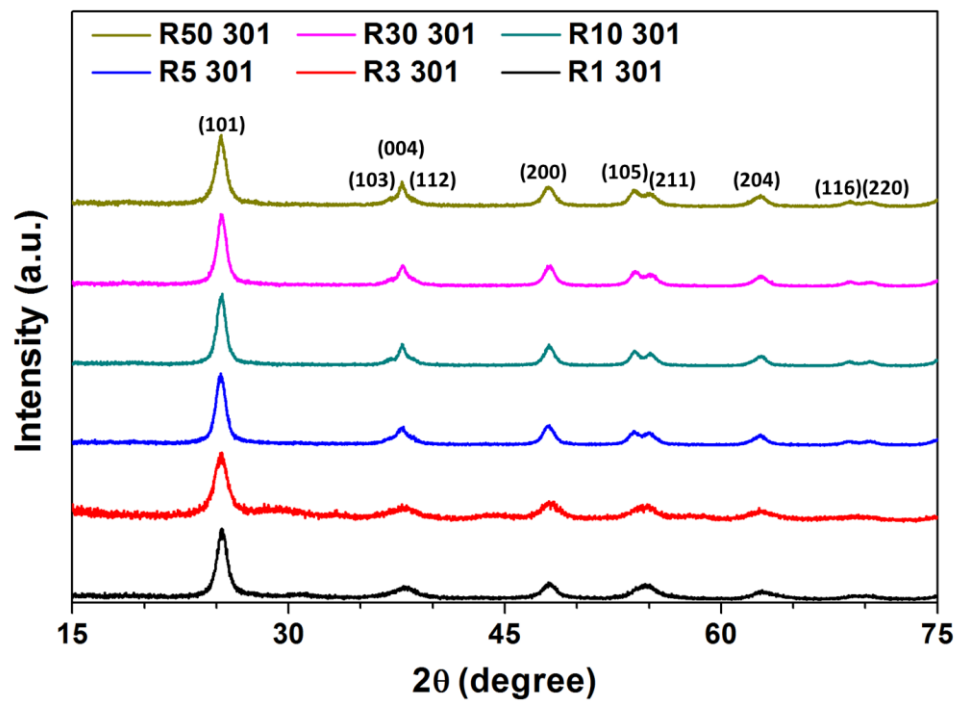


Figure 4.3. XRD patterns of the 301 series of the undoped TiO₂ powders.

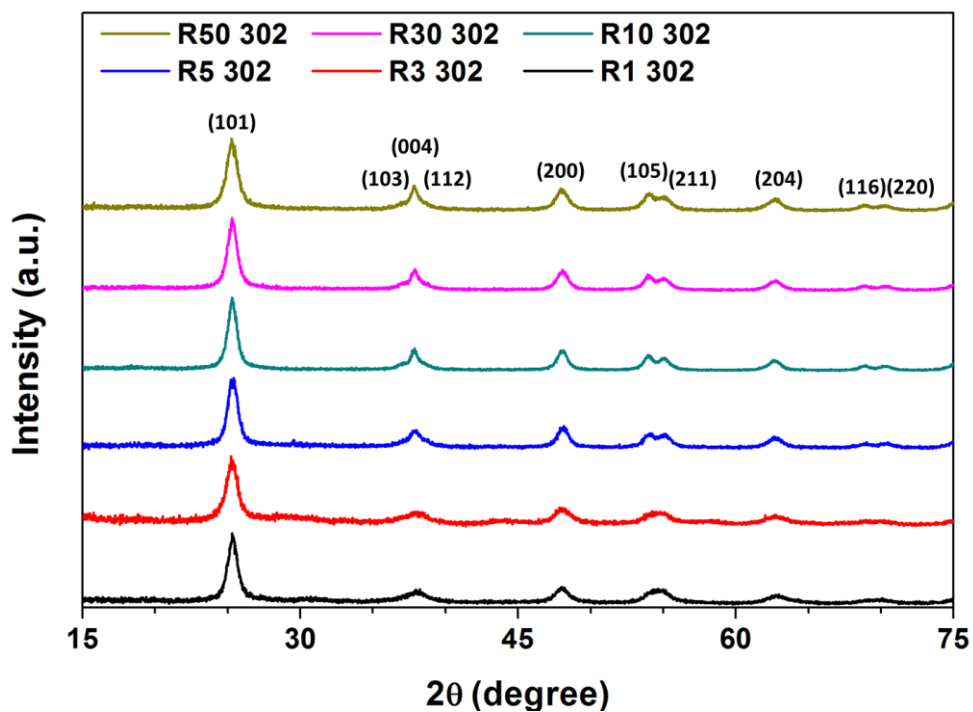


Figure 4.4. XRD patterns of the 302 series of the undoped TiO₂ powders.

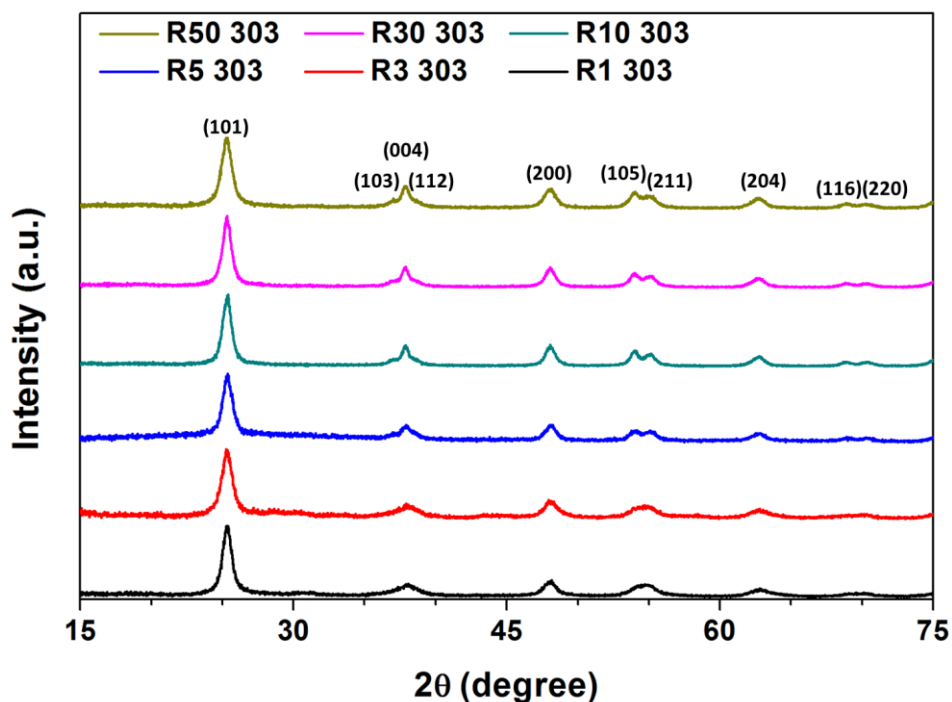


Figure 4.5. XRD patterns of the 303 series of the undoped TiO₂ powders.

The XRD patterns of the undoped TiO₂ powders calcined at 400°C, hereafter these powders were named as 400 series (401, 402, and 403) powders, revealed that irrespective of the calcination time, all of these powders composed of only anatase crystals as seen in Figures 4.6-4.8. Characterization of the phase was performed by the characteristic anatase peak of (101) plane at 2θ of $\sim 25.3^\circ$ (JCPDS #21-1272). No brookite or rutile formation was observed. Upon calcination at 400°C powders completed their crystallization and crystallite sizes increased. Also, peak resolution increased but breadth decreased. Deconvolution of the peaks for (105) and (211), (116) and (220) planes took place for all powders except powder R1.

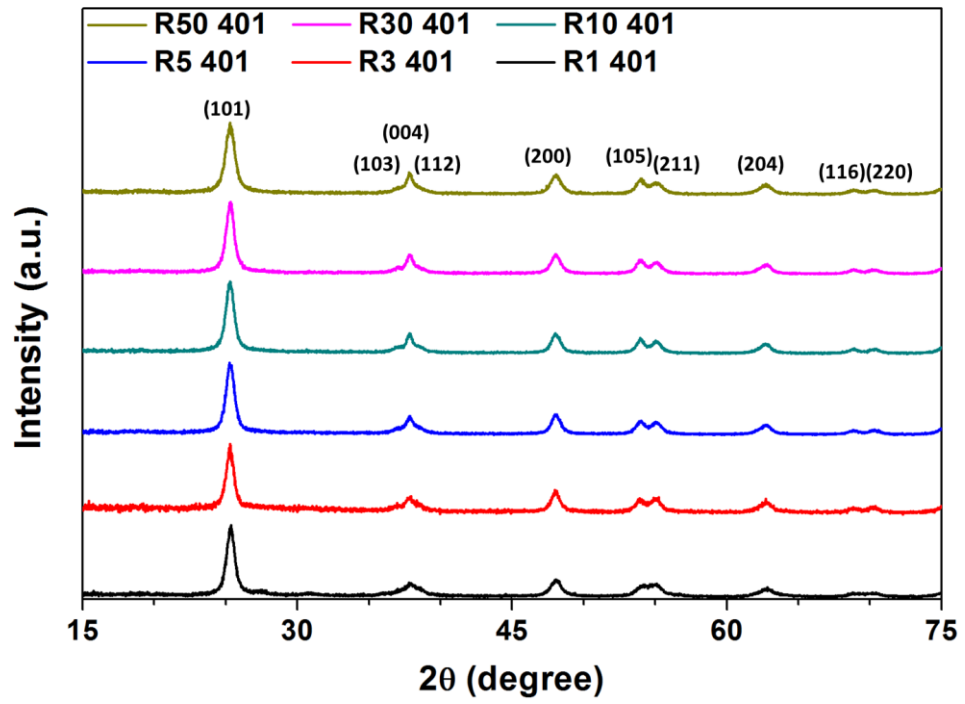


Figure 4.6. XRD patterns of the 401 series of the undoped TiO₂ powders.

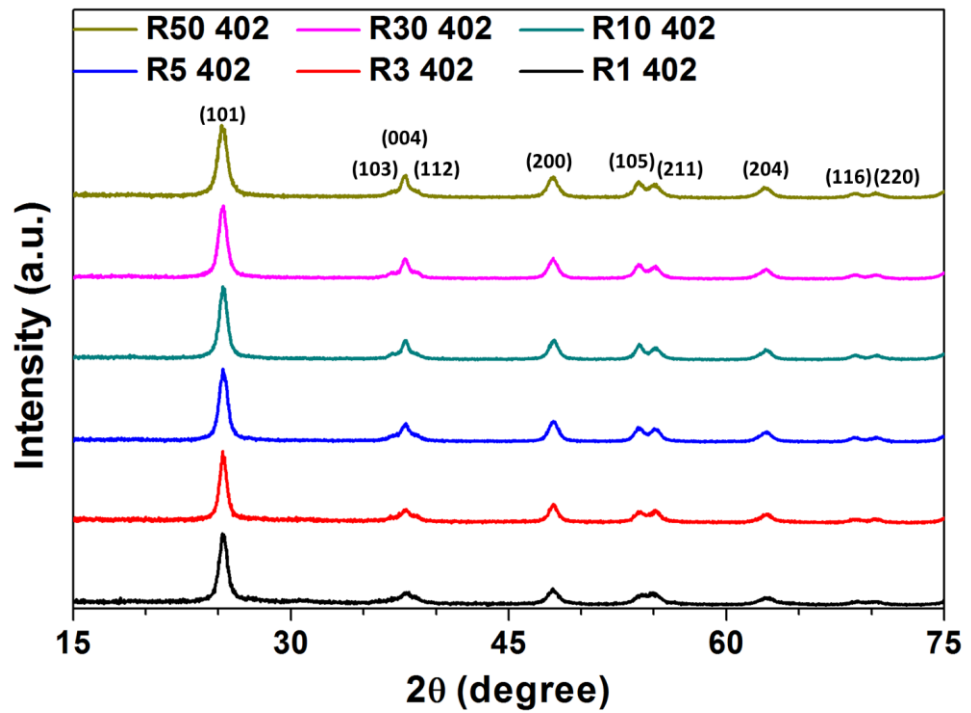


Figure 4.7. XRD patterns of the 402 series of the undoped TiO₂ powders.

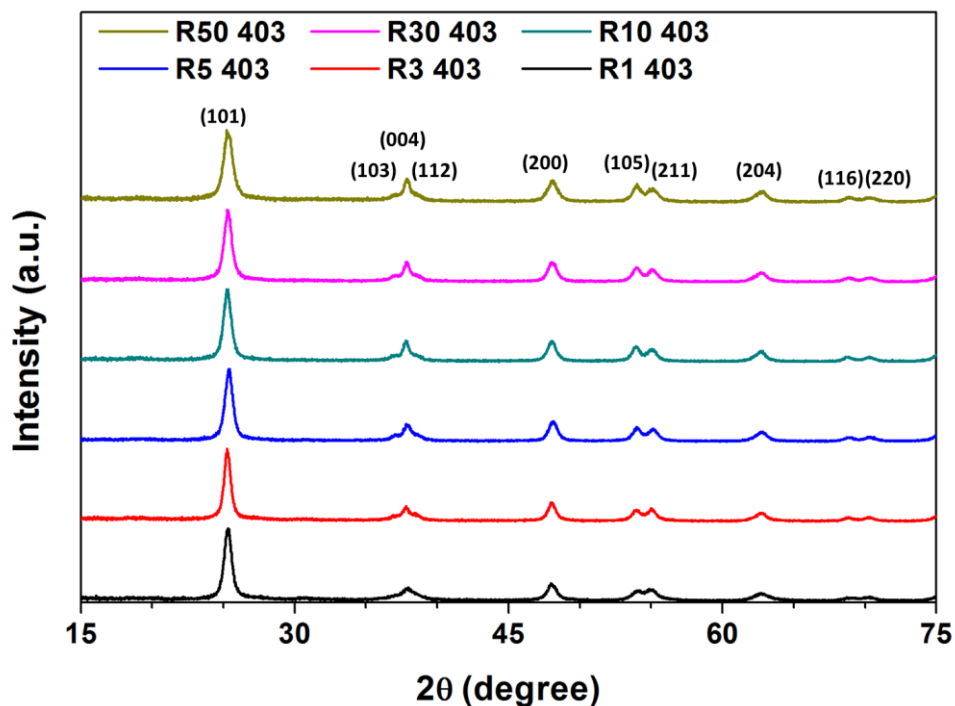


Figure 4.8. XRD patterns of the 403 series of the undoped TiO₂ powders.

The XRD patterns of the undoped TiO₂ powders calcined at 500 °C, hereafter these powders were named as 500 series (501, 502, and 503) powders, revealed that irrespective of the calcination time all of these powders except powders R1 and R3 composed of only anatase crystals. Powders R1 and R3 showed rutile crystals as seen in Figures 4.9- 4.11. Characterization of the phase was performed by the characteristic anatase peak of (101) plane at 2θ of $\sim 25.3^\circ$ (JCPDS #21-1272) and characteristic rutile peak of (110) plane at 2θ of $\sim 27.5^\circ$ (JCDPS 21-1276). No brookite formation was observed. Upon calcination at 500°C total crystallization of the powders took place and crystallite sizes increased. Also, peak resolution increased but breadth decreased. The increase in peak resolution and the decrease in breadth of the peaks were more dominant as compared to the powders in 300 and 400 series, as result of crystallite growing at high rate at 500°C. High decrease in peak breadth is the result of the passing of the activation energy of the atomic mobility, which was discussed in Section 2.4.3.1.6. Deconvolution of the peaks for (105) and (211) planes took place for all powders without any exceptions at 500°C of calcination temperature.

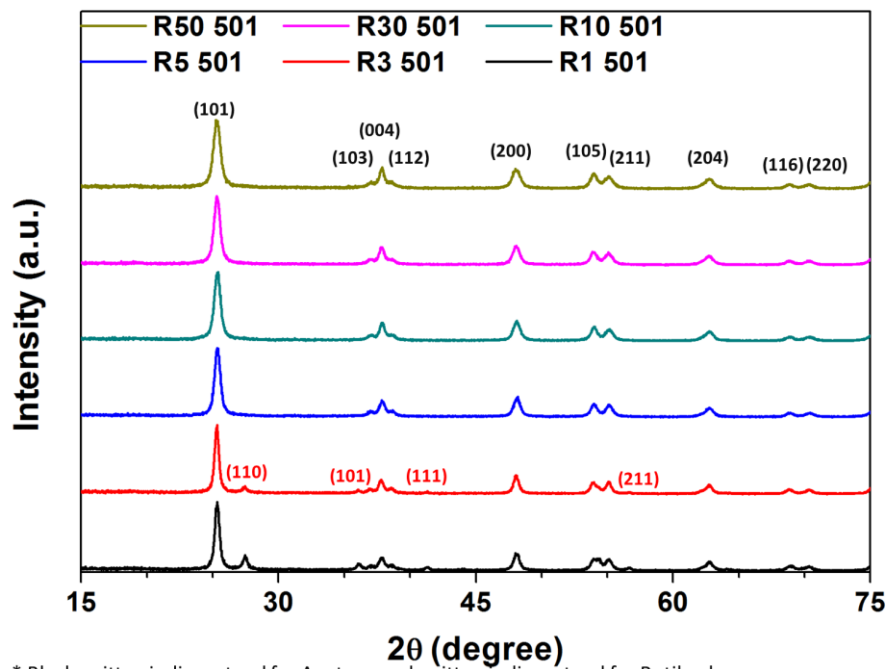


Figure 4.9. XRD patterns of the 501 series of the undoped TiO₂ powders.

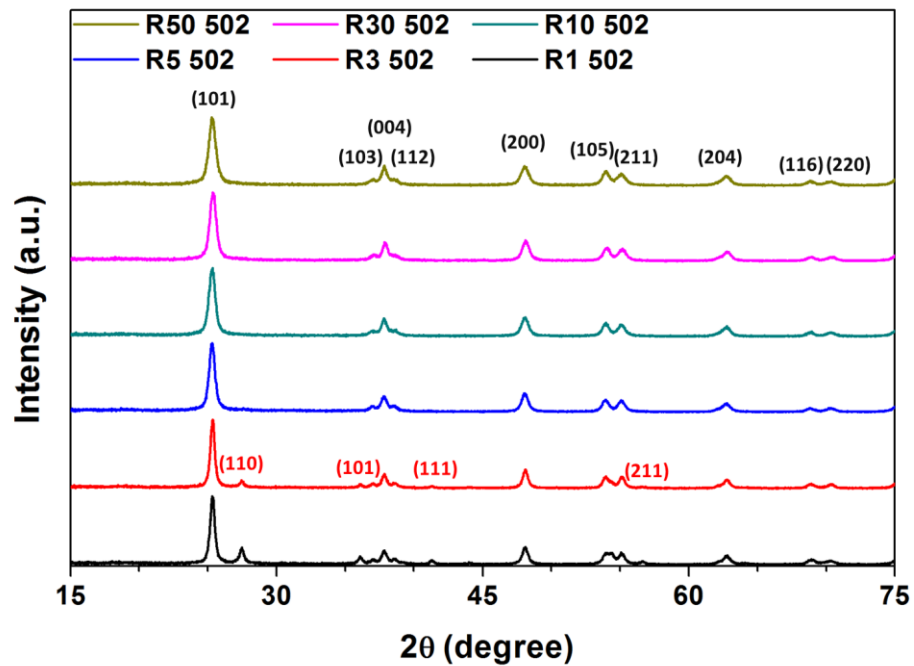
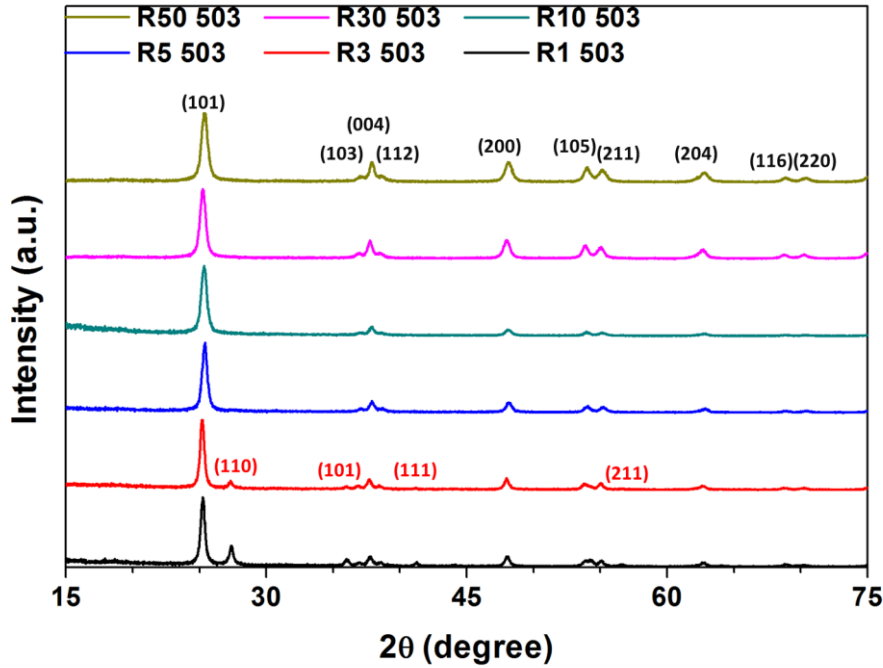


Figure 4.10. XRD patterns of the 502 series of the undoped TiO₂ powders.



* Black written indices stand for Anatase, red written indices stand for Rutile phase.

Figure 4.11. XRD patterns of the 503 series of the undoped TiO₂ powders.

Getting high crystallinity in calcined powders is also important for the application of these powders since an increase in the crystallinity percentage leads to changes in surface area and surface properties of titania powder (Chen, et al., 2009).

Rutile percentage was calculated for 500 series of powders by using Equation 4.2. The calculated values of Rutile percentage for powders R1 and R3 after calcination at 500°C and for different calcinations times were tabulated in Table 4.3.

$$\%Rutile = 100 / [1 + 0.8 * \{I_A(101) / I_R(110)\}] \quad \text{Eq. 4.2.}$$

where; I_A and I_R are intensity of the peaks for anatase and rutile phases, respectively.

Table 4.3. Rutile percentage in selected R1 and R3 powders.

	Undoped TiO₂ Powder					
	R1 501	R1 502	R1 503	R3 501	R3 502	R3 503
Rutile %	24.51	28.41	33.15	13.49	14.20	14.32

It is recognized that newly formed rutile crystallites grow to sizes close to or higher than the size of anatase crystallites because of high calcination temperature. Seabra et al., 2011 reported about 17 % rutile phase in the crystal structure for the TiO₂ powders composed of R of 3 and calcined at 500°C for 2 h. Percentage of rutile phase formed in powders R1 and R3 was comparable to the value published by Seabra et al., 2011.

General remarks obtained in XRD analysis are listed below:

- 1- As water content of the initial solution (R ratio) increases, the amount of crystallinity in the powders in as-dried form increases. Moreover, rutile formation affinity at high calcination temperatures decreases with increasing R ratio.
- 2- As calcination temperature of the powders increases, amorphous powders partially or fully crystallizes and partially crystallized powders complete their crystallization. Full crystallization is attained for the powders R ratio equal or greater than 5 at 300°C; for powders R1 and R3 at 400°C. Also, upon calcination at 500°C rutile formation is observed in powders R1 and R3 whereas anatase was the only phase for the powders having R ratio equal or greater than 5.
- 3- As calcination time of the powders increases, crystallite sizes slightly increases. Calcination time variations did not cause a significant change in the phases formed in the powders for different R ratio and calcined at different calcination temperatures.
- 4- XRD patterns suggested no significant change in the 2θ values of the peaks. Shifting of the peaks of the anatase and rutile phases as a result of changes in R ratio and calcination regimes was insignificant.

Full profile Rietveld refinement, which uses linear least square technique to minimize experimental and calculated value differences, was applied to all powders. XRD data must be collected via fixed divergence slit for counting statistics of Rietveld to be valid. Thus, XRD data of all of the undoped TiO₂ powders were collected by variable divergence slit. For the slit correction Equation 4.3 was taken into consideration.

$$I_{Fix} = I_{Var} / \sin(\theta) \quad \text{Eq. 4.3.}$$

where I_{Fix} and I_{Var} are fixed divergence slit intensity value of powder and variable divergence slit intensity value of powder.

Dual Cu K_α radiation was used during refinement since K_{α2} elimination cannot be conducted. X-ray wavelengths were 1.5406 Å for primary beam and 1.54439 Å for secondary beam. Polarization correction was not applied. Preferred orientation correction was done for peaks of (101) and (004) planes of the anatase phase in the XRD pattern. It resulted in better intensity fitting for the corresponding and the other peaks of anatase crystal.

Refinement continues until χ^2 , which is the fitting quality of the calculated values to experimental data, converges to any numeric value. Rp and wRp values also give information on fitting quality of the refinement. Fixed variables for Rietveld refinement are given in Table 4.4.

Table 4.4. Fixed variables for Rietveld refinement.

Refinement Parameter		Value
GU		33.54
GV		-17.80
GW		11.41
ANATASE	Space Group	I4 ₁ /amd
	Ti (x, y, z)	(0, 0.75, 0.125)
	O (x, y, z)	(0, 0.75, 0.3333)
	Ti (Occupancy)	1.0000
	O (Occupancy)	1.0000
RUTILE	Space Group	P4 ₂ /mnm
	Ti (x, y, z)	(0, 0, 0)
	O (x, y, z)	(0.306, 0.306, 0)
	Ti (Occupancy)	1.0000
	O (Occupancy)	1.0000

Lattice parameters are given in Tables 4.5 and 4.6.

Crystal structures of anatase and rutile phases are illustrated in Figures 4.12 and 4.13. Crystal structure of the phases was constructed in relation to the results obtained on the lattice parameters and atomic positions by using a software program CrystalMaker 9 developed by David Palmer and Shirley Palmer.

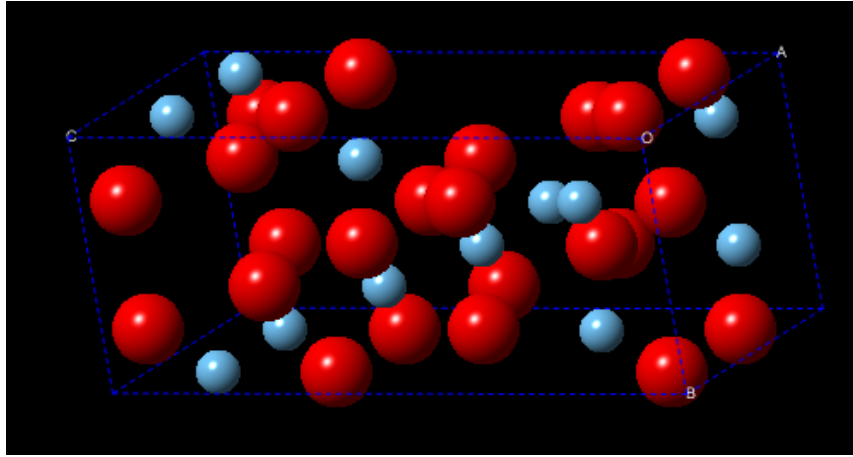


Figure 4.12. Crystal structure of anatase phase of R50 501. (Blue atoms are titanium, red atoms are oxygen).

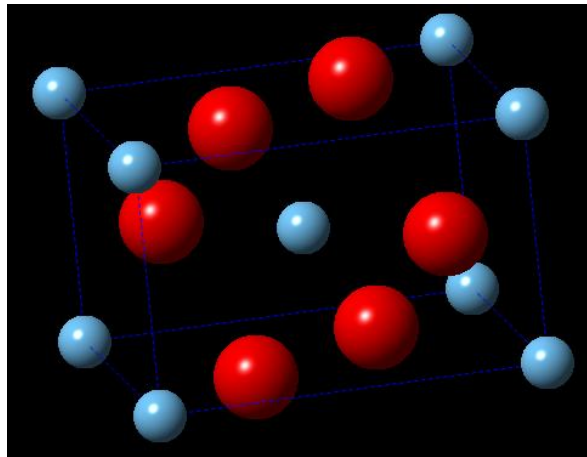


Figure 4.13. Crystal structure of rutile phase R3 502. (Blue atoms are titanium, red atoms are oxygen).

Lattice parameters and crystallite size determination of each powder were made using Rietveld refinement with the help of GSAS program. GSAS program suggests the use of program only for fully crystalline powders especially if sensitive parameters such as lattice parameters and atomic positions are being refined (Larson and Von Dreele, 2004). Lattice parameters and cell volume of rutile and anatase phases in undoped TiO_2 powders were refined and data gathered were tabulated in Tables 4.5 and 4.6, respectively.

Table 4.5. Lattice parameters and cell volume of anatase phase in undoped TiO₂ powders.

Lattice parameter	Undoped TiO ₂ powder						Calcination regime
	R1	R3	R5	R10	R30	R50	
a (Å)	-	-	3.78	3.77	3.76	3.80	As-dried
c (Å)	-	-	9.44	9.43	9.41	9.50	
Vol (Å ³)	-	-	134.47	133.93	133.22	137.12	
a (Å)	3.77	3.89	3.79	3.79	3.79	3.79	301
c (Å)	9.42	9.73	9.51	9.54	9.50	9.50	
Vol (Å ³)	133.74	147.09	136.40	137.04	136.19	136.24	
a (Å)	3.79	3.86	3.79	3.79	3.78	3.78	302
c (Å)	9.46	9.66	9.51	9.51	9.50	9.48	
Vol (Å ³)	135.57	144.23	136.61	136.49	136.04	135.33	
a (Å)	3.79	3.86	3.79	3.79	3.78	3.79	303
c (Å)	9.47	9.64	9.51	9.51	9.51	9.51	
Vol (Å ³)	136.01	143.29	136.66	136.31	135.93	136.49	
a (Å)	3.78	3.79	3.79	3.79	3.79	3.79	401
c (Å)	9.48	9.50	9.53	9.53	9.51	9.52	
Vol (Å ³)	135.77	136.32	137.06	137.15	136.58	136.87	
a (Å)	3.78	3.79	3.79	3.79	3.79	3.79	402
c (Å)	9.47	9.52	9.52	9.52	9.52	9.52	
Vol (Å ³)	135.54	137.01	136.95	136.84	136.88	136.98	
a (Å)	3.78	3.79	3.79	3.78	3.79	3.79	403
c (Å)	9.47	9.50	9.53	9.49	9.52	9.52	
Vol (Å ³)	135.20	136.18	137.15	135.64	136.71	137.11	
a (Å)	3.79	3.78	3.79	3.78	3.79	3.79	501
c (Å)	9.52	9.51	9.53	9.51	9.51	9.53	
Vol (Å ³)	136.45	136.07	137.13	136.11	136.42	137.25	
a (Å)	3.79	3.78	3.79	3.79	3.79	3.78	502
c (Å)	9.52	9.51	9.52	9.53	9.51	9.49	
Vol (Å ³)	136.45	136.26	136.74	137.17	136.39	135.57	
a (Å)	3.78	3.77	3.78	3.78	3.78	3.79	503
c (Å)	9.51	9.49	9.50	9.50	9.50	9.51	
Vol (Å ³)	135.92	135.02	135.93	135.77	135.73	136.25	

Table 4.6. Lattice parameter and cell volume of rutile phase in selected undoped TiO₂ powders.

Lattice Parameter	Undoped TiO ₂ Powder		Calcination Regime
	R1	R3	
a (Å)	4.57	4.58	501
c (Å)	2.94	2.95	
Vol (Å ³)	61.62	61.96	
a (Å)	4.59	4.58	502
c (Å)	2.95	2.95	
Vol (Å ³)	62.15	61.71	
a (Å)	4.61	4.57	503
c (Å)	2.97	2.94	
Vol (Å ³)	62.99	61.47	

All of the data gathered from Rietveld refinements for lattice parameters were presented in the tables although as-dried forms of powders R5, R10, R30, and R50, and 300 series of powders R1 and R3 deviated from average lattice parameter values as a result of being partially crystalline. No significant deviation from average lattice parameters was noted in fully crystalline powders. Rietveld refinement results are consistent with XRD results where no major shifting of the peaks of the crystalline phases was noticed. Moreover, no arithmetical relationship between water content and lattice parameter or between calcination regime and lattice parameters was recognized.

Crystallite size of the phases present in the powders was calculated with the parameters given in Table 4.4 by using Equation 4.4.

$$C(nm) = 18000k\lambda(nm) / \pi(LX) \quad \text{Eq. 4.4.}$$

where; C in the equation stands for crystallite size (nm), K is Scherrer constant taken as 0.9 since powders are rather spherical, λ is the wavelength of the X-ray, LX is the Lorentzian parameter. Calculated crystallite size values of anatase and rutile phases of the undoped TiO₂ powders after calcination in different calcination regimes are given in Figure 4.14. R1 R and R3 R in the figure are the crystallite size of the rutile phase formed in powders R1 and R3 at 500°C.

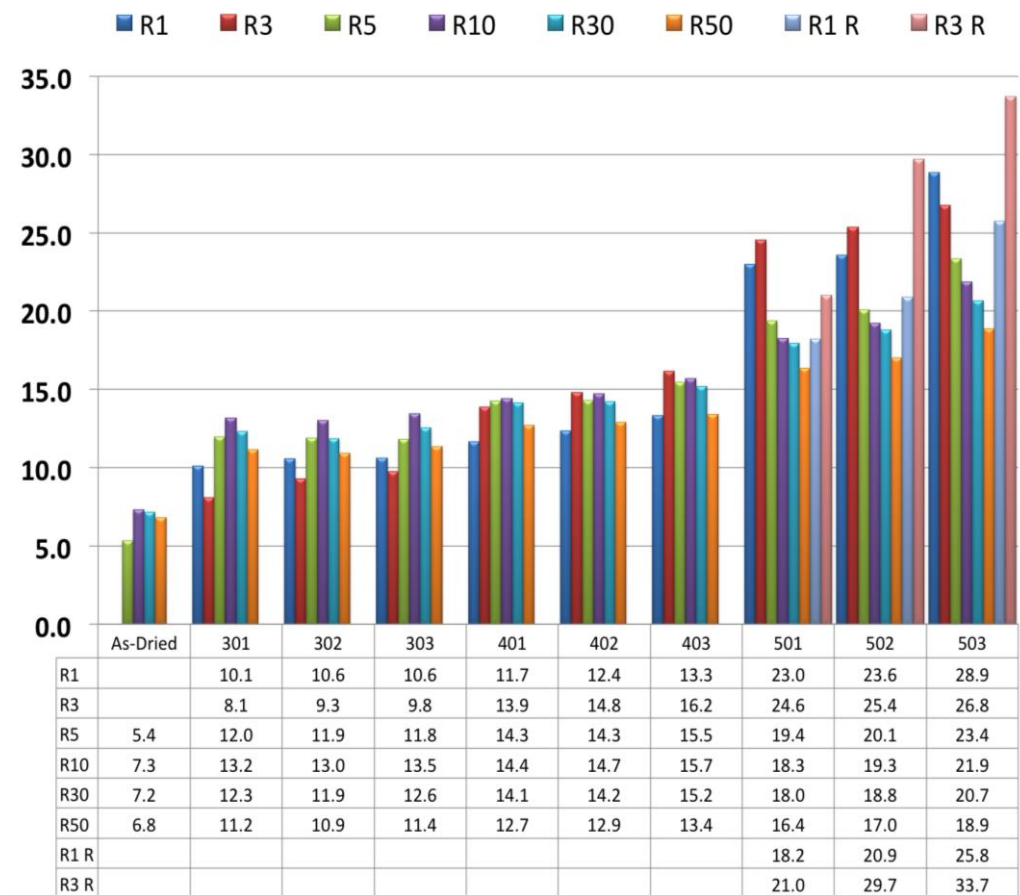


Figure 4.14. Crystallite size of the undoped TiO₂ powders calcined in different calcination regimes.

Size of crystallites plays a key role in photocatalysis, since they affect specific surface area directly. In order to, get a high photocatalytic activity, charge separation (e^-/h^+) should be done effectively. Oxidation/reduction reactions have

to take place at the surface. Increasing specific surface area, increases number of possible reaction sites and decreases the distance to be travelled by separated charges until reaching the nearest surface (Jung, et al., 2005; Rehman, et al., 2009). Calculated crystallite size values revealed that calcination temperature, calcination time, and initial solution composition have affected the size of the formed crystals. It has been observed that calcination temperature has the largest effect on crystallite size. The effect of calcination time on size is not as large as calcination temperature because nucleation and growth kinetics depend on temperature more strongly than time.

Crystallite size of the as-dried powders was less than 8 nm. Crystallite size of the calcined powders varied according to calcination regimes applied. It was below 14 nm for 300 series of the powders, below 16 nm for 400 series of the powders, and below 30 nm for 500 series of the powders. Ramaswamy et al., 2008 reported crystallite size around 8 nm for the powders calcined at 300°C for 3 h while Vorontsov et al., 2001 published crystallite size values around 14 nm for the powders calcined at 400°C for 3 h. Colmenares et al., 2006 calculated crystallites with average size of 28 nm for the powders calcined at 500°C for 6 h. It is apparent that the results obtained in this study were consistent with the ones given in literature. The smallest anatase crystallite size was obtained in powder R5 in as-dried form as 5.5 nm while the largest one was seen in powder R3 503 as 29.8 nm. The temperature of 500°C is the edge value for free movement of atoms, at which crystallite size values of anatase phase showed a jump to much higher values than expected values from routine increase with respect to calcination temperature increment. Powders R1 and R3 contained some amount of rutile phase upon calcination at 500°C. The smallest rutile crystallite size was obtained in powder R1 501 as 24.4 nm while the largest one was seen in powder R1 503 as 32.3 nm.

Data gathered on crystallite size suggested that effect of initial solution composition on crystallite size should not be overlooked. Powders R5, R10, R30, and R50 showed very close crystallite size values in all calcination regimes, but powders R1 and R3 showed dissimilarities. The crystallite size values of

powders R1 and R3 are smaller at 300 series, equal values at 400 series, and much larger at 500 series than that of powders R5, R10, R30, and R50.

Crystallite size of rutile phase in powder R3 was bigger than that in powder R1. Gouma and Mills 2001 reported that rutile phase transformation takes place on the surface of “coarser” anatase particles, in the form of fine lathes (plates) via a shear mode. Therefore, by having larger anatase crystallites, powder R3 has smaller specific surface area at where rutile crystallizes. Then, most of the incoming heat will be used for growth of the rutile crystals formed rather than nucleation of new crystals in powder R3 since nucleation sites are limited as compared to powder R1.

There are sixty undoped TiO₂ powders synthesized. Their Rietveld fitting figures, χ^2 , Rp, and wRp values are not given in this thesis manuscript. However, some representative refinement results for the selected powders in each R ratio are presented in Table 4.7. The best and worst fitting graphs of selected powders are shown in Figures 4.15-20.

Table 4.7. The χ^2 , Rp, and wRp values of the best and worst fitting for the powders calcined in different calcination regimes.

Powder		Well Fitted	Poorly Fitted
R1		R1 502	R1 401
	χ^2	0.0745	0.1411
	Rp	0.0854	0.1035
	wRp	0.1130	0.1323
R3		R3 502	R3 401
	χ^2	0.0629	0.1743
	Rp	0.0834	0.0894
	wRp	0.1118	0.1153
R5		R5 501	R5 302
	χ^2	0.0691	0.1393
	Rp	0.0941	0.0846
	wRp	0.1102	0.1100
R10		R10 501	R10 503
	χ^2	0.0686	0.1081
	Rp	0.0803	0.1213
	wRp	0.1054	0.1639
R30		R30 503	R30 302
	χ^2	0.0802	0.1069
	Rp	0.0852	0.0883
	wRp	0.1129	0.1141
R50		R50 503	R50 302
	χ^2	0.0802	0.1316
	Rp	0.088	0.088
	wRp	0.1159	0.1156

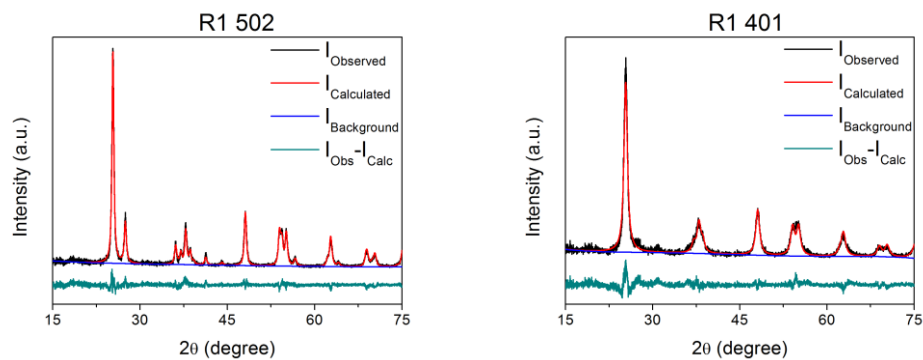


Figure 4.15. Well and poor Rietveld refinement fittings for powder R1.

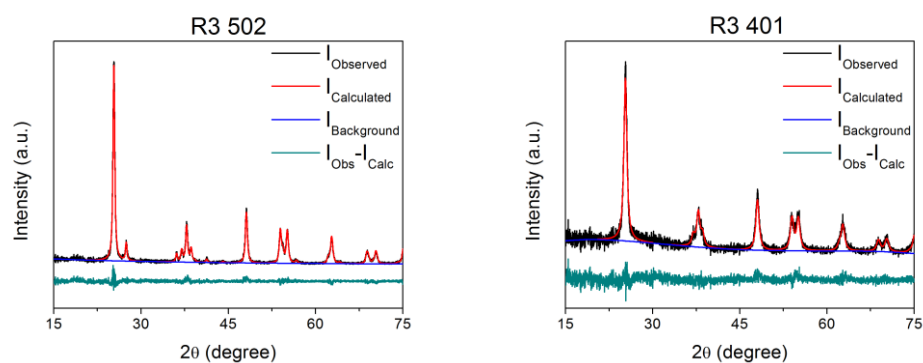


Figure 4.16. Well and poor Rietveld refinement fittings for powder R3.

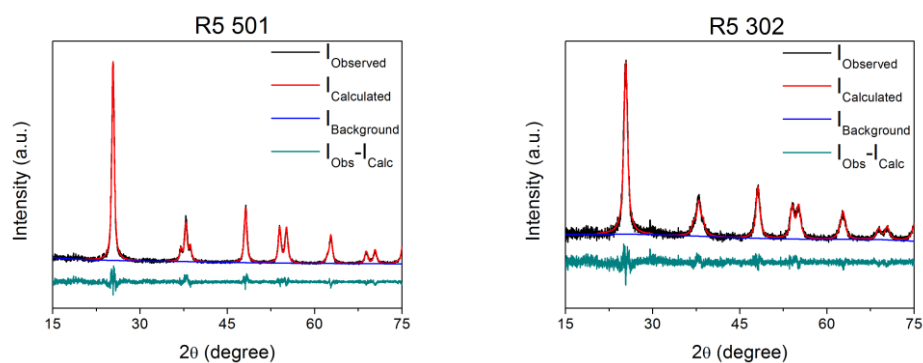


Figure 4.17. Well and poor Rietveld refinement fittings for powder R5.

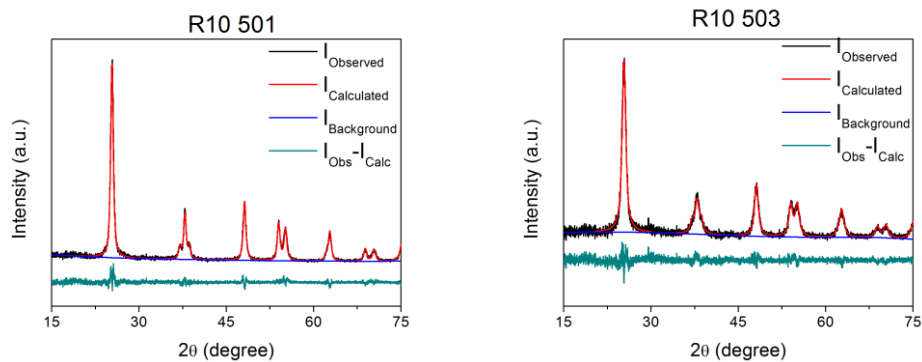


Figure 4.18. Well and poor Rietveld refinement fittings for powder R10.

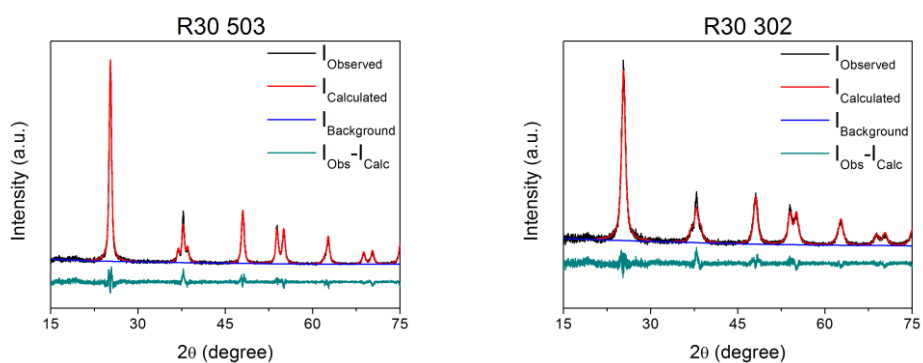


Figure 4.19. Well and poor Rietveld refinement fittings for powder R30.

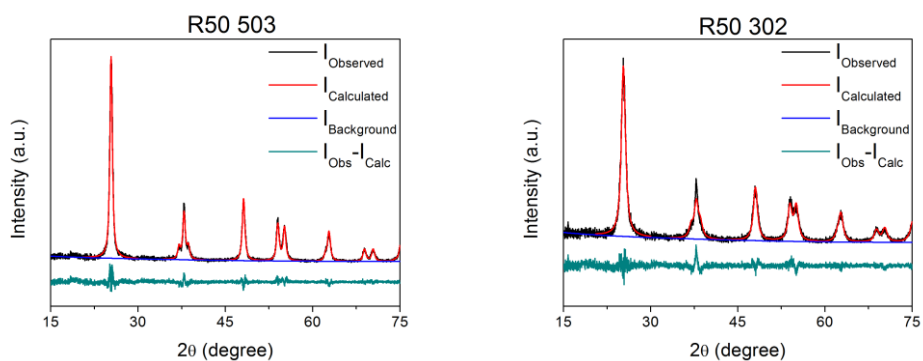


Figure 4.20. Well and poor Rietveld refinement fittings for powder R50.

4.3.4. Scanning Electron Microscopy (SEM) Analysis

Surface morphologies of all of the powders were investigated by using SEM. SEM analyses revealed that all powders were composed of particles smaller than 40 nm in size. Particle sizes could not be measured accurately from SEM images due to agglomeration, focusing difficulties at high magnifications, and astigmatism correction problems. Also, the irregular shapes of agglomerates caused level differences in the powders examined.

The water content in the initial solution did not have a significant effect in the morphology of the as-dried powders. SEM microstructures of the powders with different R ratio were compared with each other through SEM images taken in as-dried form as well as in 503 regimes (after calcination at 500°C for 3 h) in Figures 4.21-26. In as-dried form the smallest particle size was obtained whereas in the 503 regime i.e., regime at which highest temperature and time were applied, the largest particle size was obtained among the other calcination regimes applied. These two forms of the powders were the lower and upper limits of particle sizes.

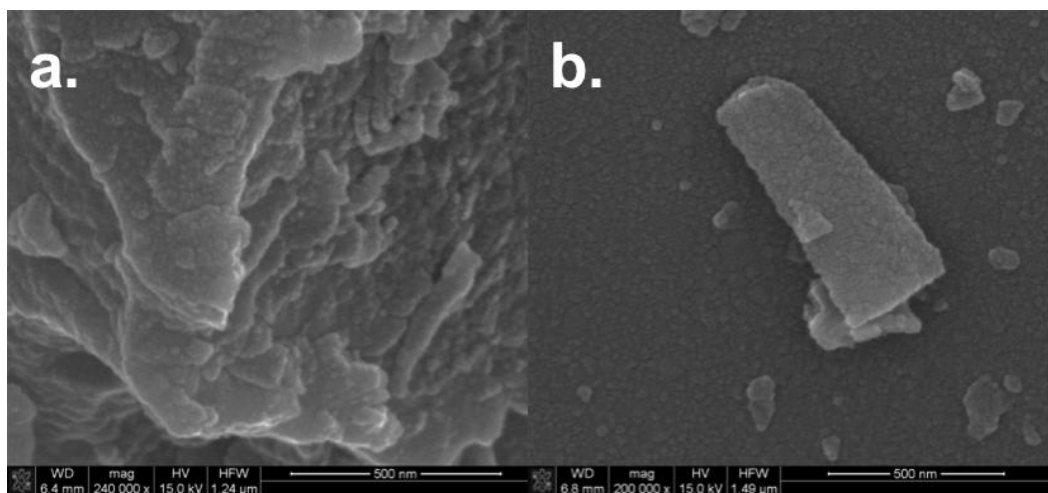


Figure 4.21. SEM images of a. powder R1 as-dried and b. powder R1 503.

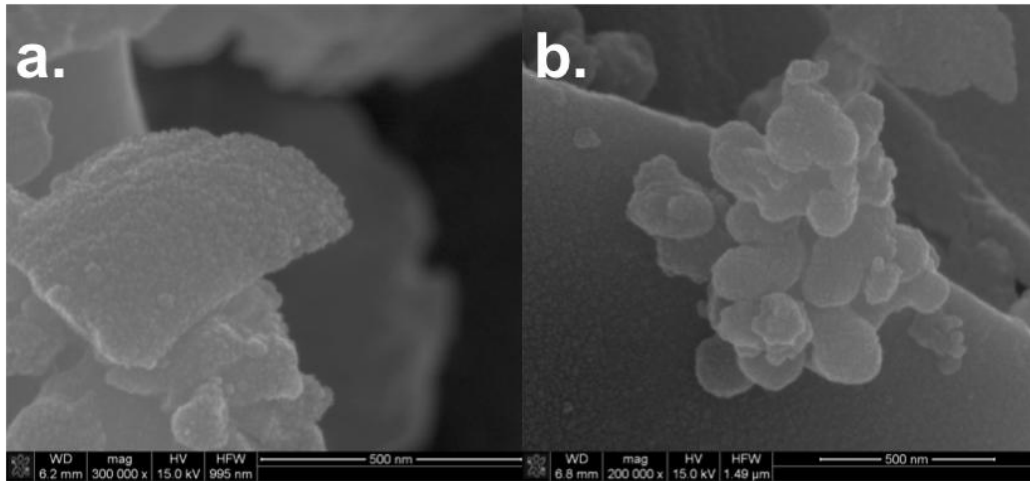


Figure 4.22. SEM images of a. powder R3 as-dried and b. powder R3 503.

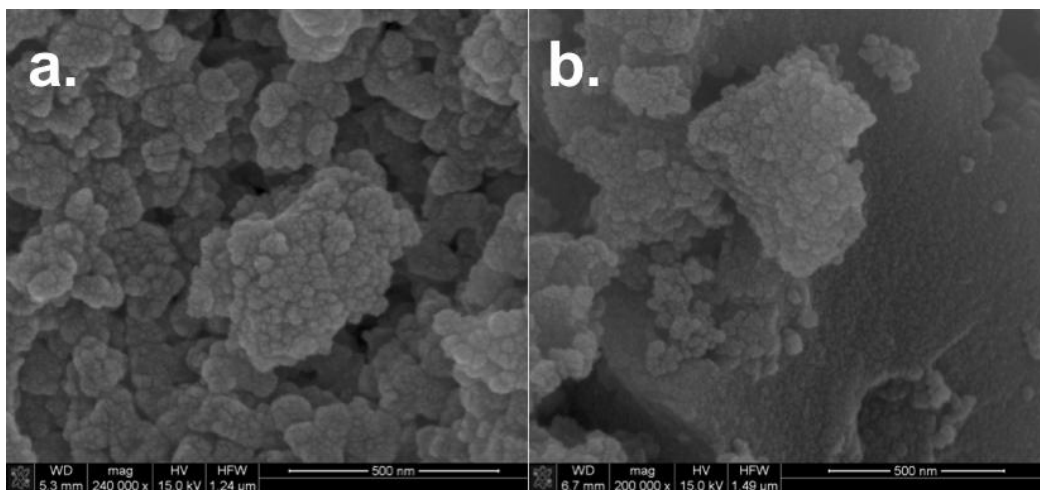


Figure 4.23. SEM images of a. powder R5 as-dried and b. powder R5 503.

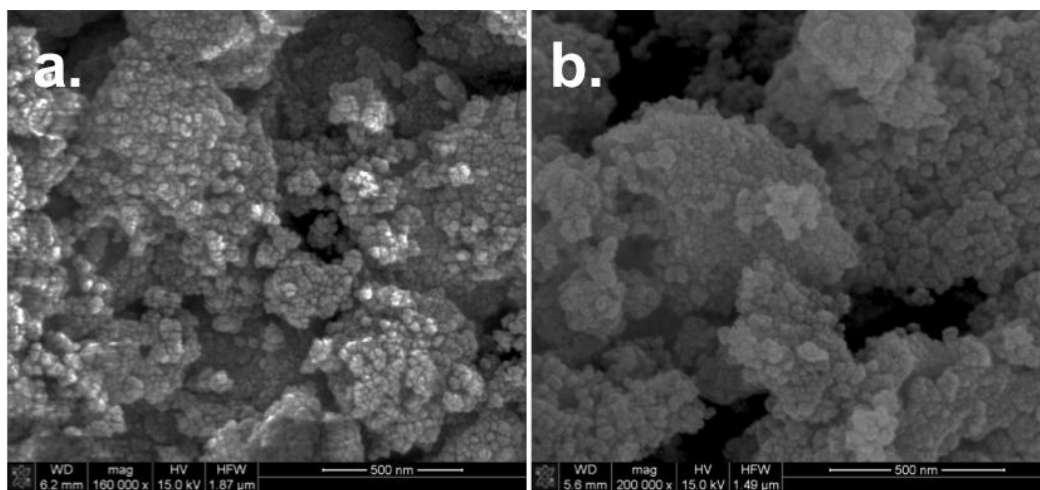


Figure 4.24. SEM images of a. powder R10 as-dried and b. powder R10 503.

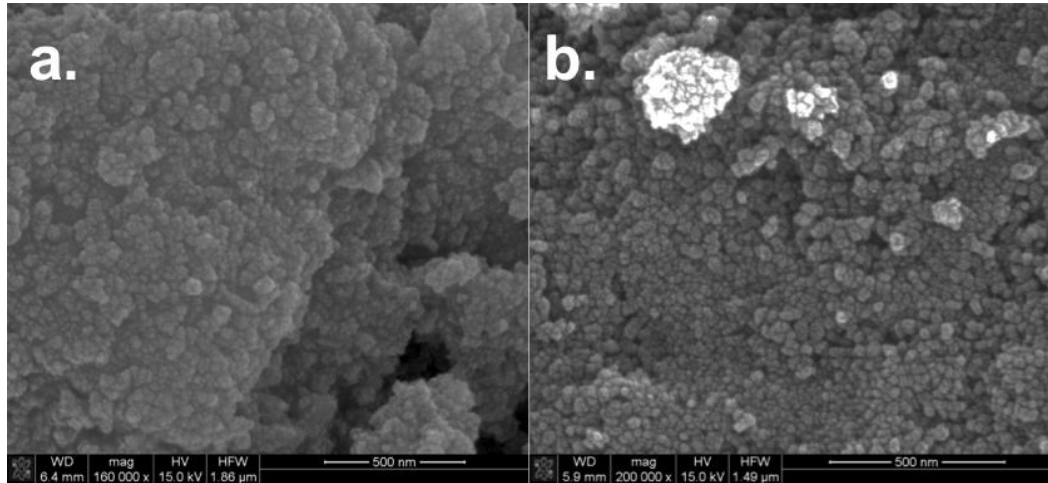


Figure 4.25. SEM images of a. powder R30 as-dried and b. powder R30 503.

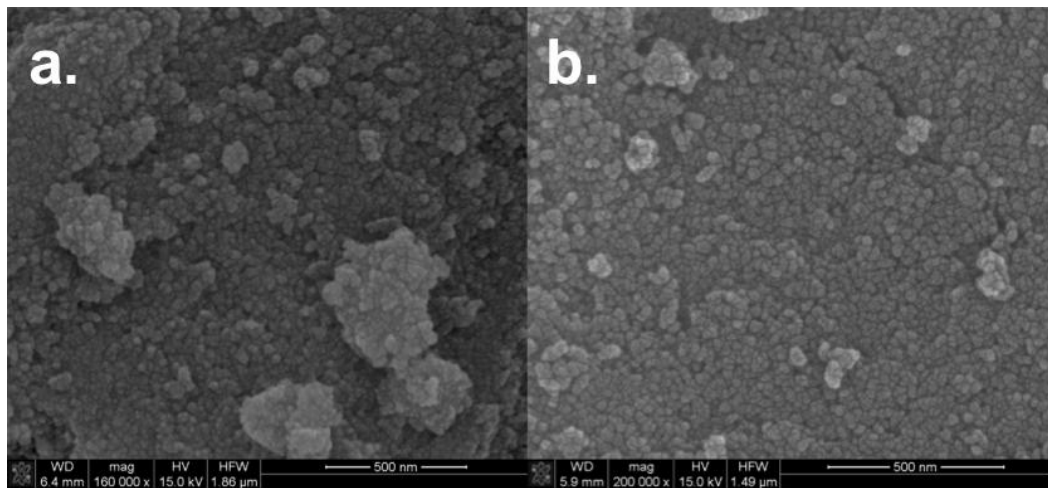


Figure 4.26. SEM images of a. powder R50 as-dried and b. powder R50 503.

General morphology of the powders did not show much difference with respect to calcination temperature and calcination time. Figure 4.27 illustrated SEM images of the randomly selected nine powders having different R ratios and exposed to different calcinations regimes. All particles in the powders were highly agglomerated. Size and shape of the agglomerates were totally irregular and random in distribution while individual particles were nearly spherical in shape.

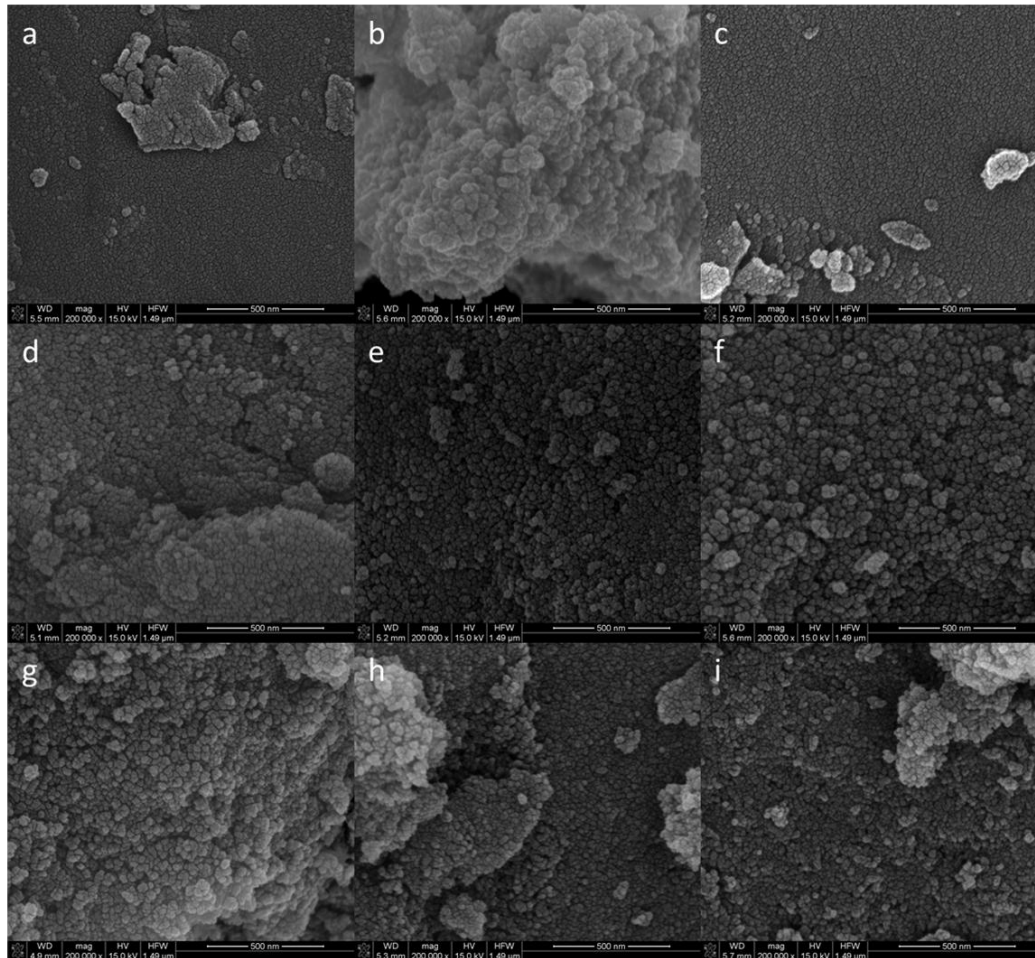


Figure 4.27. SEM images of powders a. R1 401, b. R1 501, c. R3 401, d. R5 302, e. R10 302, f. R10 403, g. R30 401, h. R50 402, and i. R50 502.

SEM images and morphological properties of the powders observed in this study were in a good agreement with that reported by Mohammadi et al., 2008 and Ramaswamy et al., 2008 who synthesized anatase crystals by sol-gel process for R ratios of R500 and R1.5, respectively. Furthermore, Kapusuz et al., 2013 synthesized the TiO_2 powders by non-hydrous sol-gel, and Hu et al., 2003 synthesized them by precipitation. The SEM images presented in their studies showed small and highly agglomerated particles. Consequently, the method used in the synthesis of the TiO_2 powders did not have a significant effect on their morphological features.

4.3.5. Diffuse Reflectance Spectroscopy (DRS)

The variation in DRS with respect to wavelength for the powders composed of different R ratios and exposed to different calcination regimes were shown in Figures 4.28-33. DRS of all powders increased with increasing wavelength. As-dried forms of the powders R1 and R5 showed blueshift (movement of the adsorption edge to lower wavelengths) whereas as-dried forms of the powders R10, R30, and R50 showed redshift (movement of the adsorption edge to higher wavelengths).

DRS of the powders changed when R ratios and calcination regimes were changed. For instance, powders R1 and R3 have smaller reflectance than the other powders with different R ratio for almost every calcination regimes. A comparison of the DRS taken for the powders of different R ratio before and after calcination revealed that redshift of adsorption edge was observed for almost every powder as a result of calcination. Vorontsov et al., 2001 reported very similar results. Powders R1, R5, and R50 showed redshift for 301 regimes, meanwhile powder R3 showed blueshift for wavelengths above 450 nm. Powders R1 and R3 showed high redshift when compared to others powders for 302, 303, 401, 402, and 403 calcination regimes. One of the goals of this study was to make powders visible light (daylight) active. Hence, having the smallest band gap values are beneficial, since it enables the powder to be active in a larger portion of EM-spectrum.

In 300 and 400 series of powder R1, low reflection values were measured as seen in Figure 4.28, which is probably because of the brownish, yellowish color of powders. Seo et al., 2011 reported similar results on coloring of undoped TiO₂ powders. Low reflection values in these powders are probably due to the result of high amount of adsorption of the incoming light beam for corresponding color of the powder. High reflection values (>80%) were observed for 500 series of powder R1 probably due to white color of the powders.

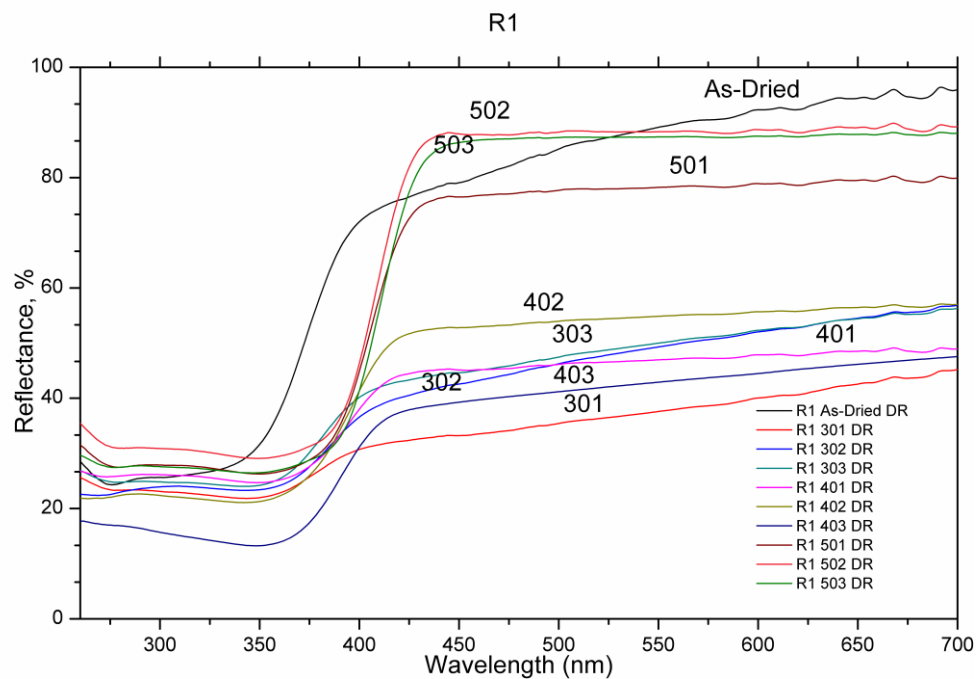


Figure 4.28. Diffuse reflectance spectra of powder R1 with respect to wavelength for different calcination regimes.

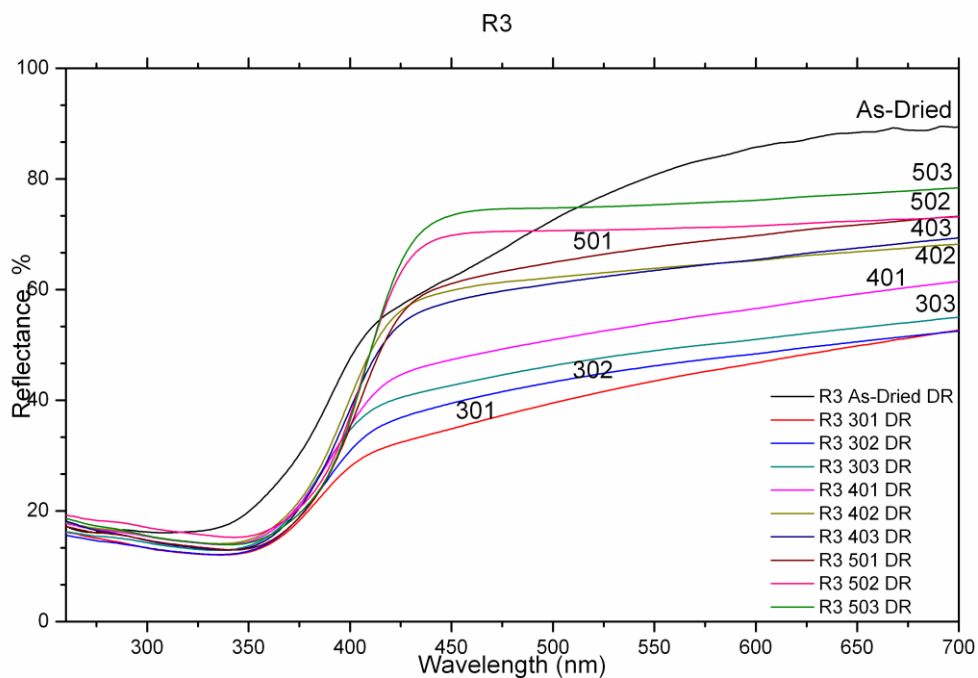


Figure 4.29. Diffuse reflectance spectra of powder R3 with respect to wavelength for different calcination regimes.

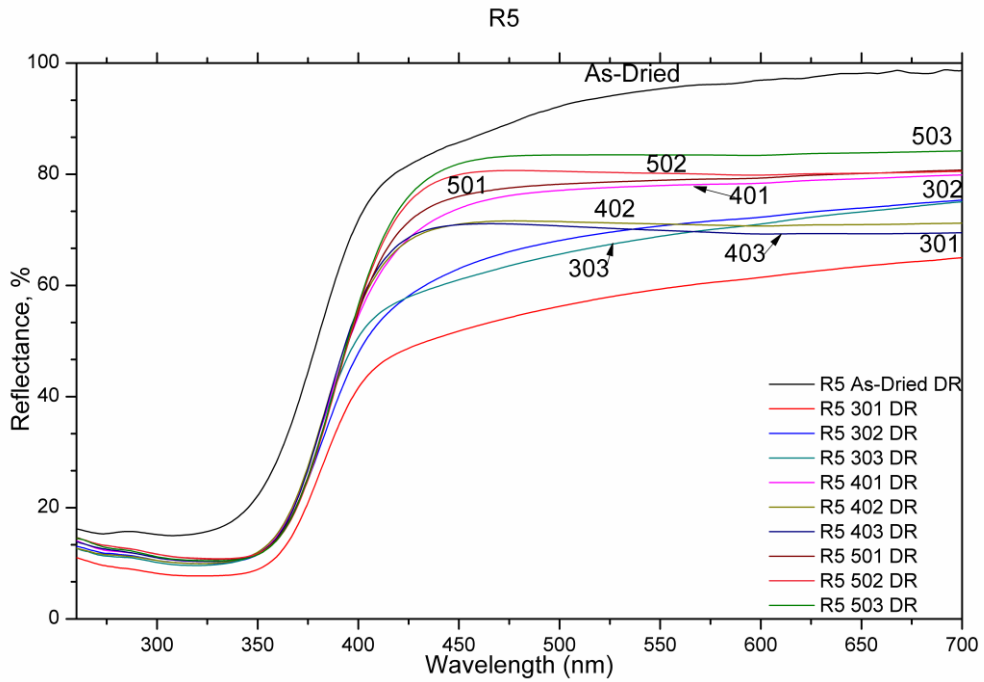


Figure 4.30. Diffuse reflectance spectra of powder R5 with respect to wavelength for different calcination regimes.

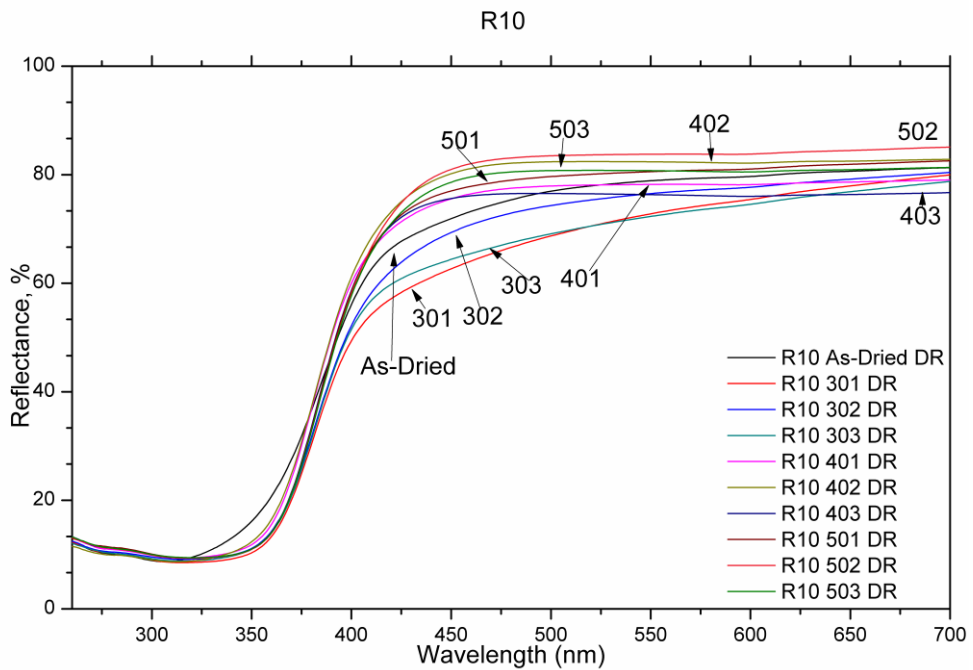


Figure 4.31. Diffuse reflectance spectra of powder R10 with respect to wavelength for different calcination regimes.

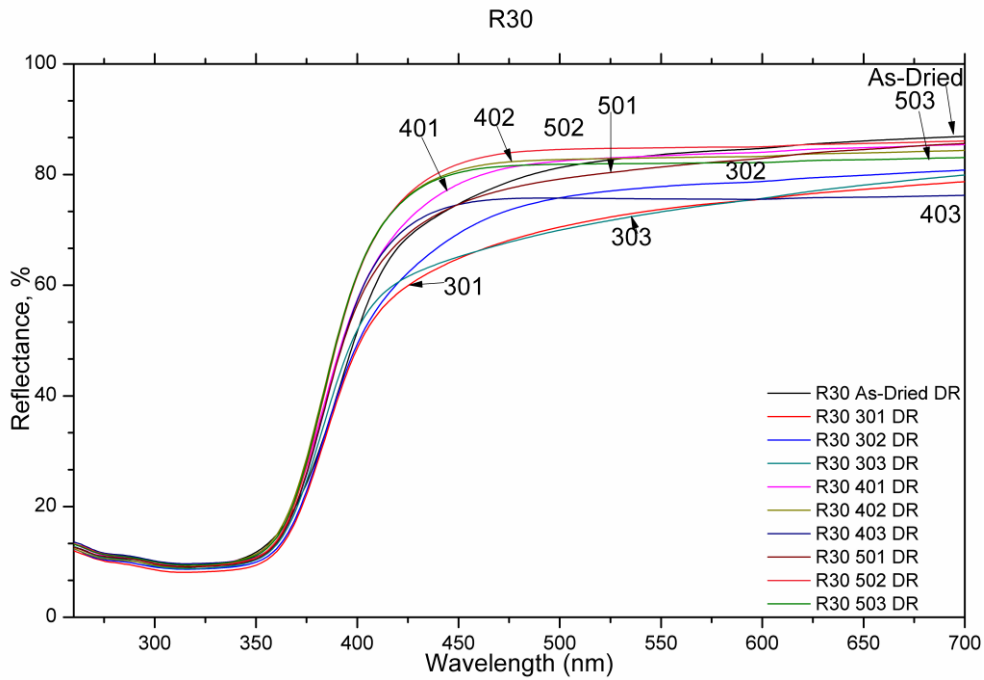


Figure 4.32. Diffuse reflectance spectra of powder R30 with respect to wavelength for different calcination regimes.

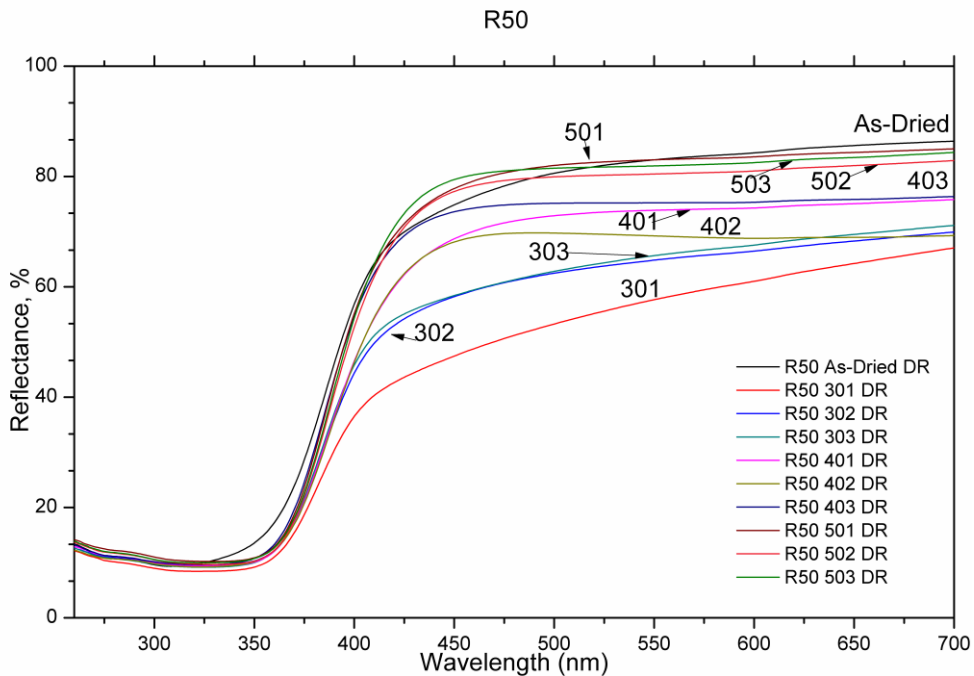


Figure 4.33. Diffuse reflectance spectra of powder R50 with respect to wavelength for different calcination regimes.

DRS reflection values of powder R3 showed an ordered change with respect to calcination regimes. 300 series of powder R3 appeared in yellowish color. Their reflection values are low with respect to 400 and 500 series of powder R3 as shown in Figure 4.29. All calcination regimes ended up with a redshift at adsorption edge for powders R5 and R50. However, powders R10 and R30 showed redshift for 300 series, while 400 and 500 series showed blueshift. No order or relation is predictable for the changes in reflection with respect to calcination regimes among the powders. Nonetheless, the DRS measurements showed that all powders are visible light active. Band gap energies of all of the powders were calculated by using Kubelka-Munk Transform and listed in Table 4.8.

Table 4.8. Band gap energy of the undoped TiO₂ powders synthesized.

Powder Name	Energy Band Gap (eV)	Powder Name	Energy Band Gap (eV)	Powder Name	Energy Band Gap (eV)
R1 As-dried	3.08	R5 As-dried	3.12	R30 As-dried	3.03
R1 301	2.45	R5 301	3.07	R30 301	3.1
R1 302	2.66	R5 302	3.06	R30 302	3.09
R1 303	2.73	R5 303	3.09	R30 303	3.12
R1 401	2.68	R5 401	3.08	R30 401	3.12
R1 402	2.83	R5 402	3.09	R30 402	3.13
R1 403	2.85	R5 403	3.1	R30 403	3.13
R1 501	2.9	R5 501	3.09	R30 501	3.13
R1 502	2.92	R5 502	3.07	R30 502	3.14
R1 503	2.9	R5 503	3.08	R30 503	3.14
R3 As-dried	2.87	R10 As-dried	3.04	R50 As-dried	3.07
R3 301	2.81	R10 301	3.09	R50 301	3.03
R3 302	2.84	R10 302	3.1	R50 302	3.05
R3 303	2.88	R10 303	3.09	R50 303	3.07
R3 401	2.83	R10 401	3.13	R50 401	3.06
R3 402	2.88	R10 402	3.13	R50 402	3.05
R3 403	2.89	R10 403	3.12	R50 403	3.1
R3 501	2.85	R10 501	3.13	R50 501	3.08
R3 502	2.88	R10 502	3.12	R50 502	3.08
R3 503	2.88	R10 503	3.12	R50 503	3.08
P25	3.13				

Band gap energy of P25, a commercially available TiO₂ powder composed of 81% anatase 19% of rutile (Raj and Viswanathan, 2009), was also measured and given in Table 4.8 for comparison of the data. In general, R ratio and calcination regime had an influence on band gap energy of the powders. For instance, powders R1 and R3 have smaller band gap energy than the other powders in almost every calcination regimes. However, no arithmetical relation could be driven amongst them. The smallest band gap energy values were obtained for 300 series of powder R1. Etacheri et al., 2011 explained the variation of the band gap values with variations in lattice parameters of III-V semiconductors and modification of the valance band resulting from oxygen excess defects.

Band gap energies of all of the powders were in visible light range. Band gap energy value of P25 was measured to be 3.13 eV. Grabowska et al., 2009 reported band gap energy of P25 as 3.15 eV. The measured band gap energy of P25 was lower than the reported value of anatase (3.2 eV) and of rutile (3.0 eV) phases by Ersoz 2009. Carp, et al., 2004 and Nahar, et al., 2009 stated that e^-/h^+ recombination rate decreases with coexistence of anatase and rutile phases together. Same kind of charge separation was observed at semi-conductor coupling application (Lee and Gouma, 2012). Coexistence of anatase and rutile is a natural born semi-conductor couple that has an activation energy lower than that of anatase but higher than that of rutile (Carp, et al., 2004; Zaleska, et al., 2009). It finds use in wide application areas due to its photocatalytic activation mechanism, during which e^- from valance band (VB) of anatase is excited to conduction band (CB) of rutile. Valance and conduction band positions of anatase and rutile were shown in Figure 2.2.

Comparing the band gap energies of the powders with that of P25, it was obvious that 52 of the total of sixty powders had lower band gap energy than P25, 6 of them had almost the same band gap energy with P25, and 2 of them had higher band gap energy than P25. Although 2 of the powders had higher band gap energy than P25, the difference between band gap energy of the 2powders and that of P25 was not much. For this reason, none of the R ratio and

calcination regime could be ignored for determination of the best R ratio and calcination regime for doping conditions from the DRS data.

4.4. Photocatalytic Activity Of Undoped TiO₂ Powders

4.4.1. Methylene Blue Degradation

The calculated percentage of MB degradation values after 30, 60, and 90 min UV light illumination for the powders composed of different R ratios and exposed to different calcination regimes were listed in Table 4.9. MB degradation value of P25 after 30, 60, and 90 min UV light illumination was also measured for comparison of the data and was given in Table 4.9. MB degradation measured in dark at 30 min was taken as the reference point for MB degradation calculations rather than MB concentration in the initial solution since the decrease in MB concentration taking place in dark was a simple physical adsorption process. A 30 min stirring in dark was done to ascertain the physical adsorption/desorption equilibrium. Houas et al., 2001 reported that a decrease in MB molecule concentration in dark is not a photocatalytic process. The decrease in MB concentration only after physical adsorption/desorption equilibrium point is due to photocatalytic degradation.

Table 4.9. MB degradation values of the powders after UV light illumination.

Powder	Percentage of MB Degradation		
	after 30 min UV light illumination	after 60 min UV light illumination	after 90 min UV light illumination
R1 As-dried	5.48	9.19	9.80
R1 301	27.26	46.56	65.95
R1 302	34.24	61.50	75.55
R1 303	17.33	37.77	53.73
R1 401	15.74	24.99	32.56
R1 402	12.45	30.19	43.00
R1 403	21.64	43.77	74.31
R1 501	6.45	11.00	19.36
R1 502	8.22	11.09	20.49
R1 503	6.07	12.68	20.13
R3 As-dried	2.01	2.24	3.19
R3 301	21.64	47.44	64.84
R3 302	9.12	23.63	36.43
R3 303	8.97	21.18	32.84
R3 401	6.60	9.42	12.30
R3 402	10.22	19.85	29.60
R3 403	5.57	13.90	23.66
R3 501	21.72	26.10	37.55
R3 502	13.81	27.18	42.08
R3 503	14.09	26.75	39.05
R5 As-dried	10.75	22.75	29.94
R5 301	59.65	91.41	99.47
R5 302	59.94	85.94	95.62
R5 303	52.94	82.07	93.60
R5 401	57.23	84.45	94.68
R5 402	50.32	71.71	84.78
R5 403	57.25	84.21	93.91
R5 501	38.67	79.93	99.99
R5 502	68.26	87.42	95.81
R5 503	73.03	92.72	99.79
R10 As-dried	31.30	60.45	88.71
R10 301	15.34	22.40	27.74
R10 302	73.72	92.79	99.88
R10 303	71.17	92.59	96.60
R10 401	63.27	86.21	95.11
R10 402	57.15	82.66	97.39
R10 403	77.96	93.63	98.51
R10 501	59.00	90.33	94.72
R10 502	58.26	85.63	97.50
R10 503	75.29	95.84	99.79

Table 4.9. (cont'd)

R30 As-dried	39.52	76.24	96.07
R30 301	73.54	97.80	99.28
R30 302	63.03	89.08	98.00
R30 303	59.08	80.71	93.06
R30 401	71.28	91.82	98.55
R30 402	72.68	94.30	99.35
R30 403	61.94	86.85	96.55
R30 501	62.18	84.98	91.99
R30 502	51.90	81.83	94.89
R30 503	69.34	92.31	98.31
R50 As-dried	29.30	56.79	79.11
R50 301	58.56	94.57	99.41
R50 302	63.07	87.36	97.52
R50 303	44.70	68.78	86.09
R50 401	38.58	82.24	94.86
R50 402	58.07	83.52	89.40
R50 403	52.44	84.25	96.03
R50 501	43.39	78.17	94.75
R50 502	52.55	81.97	92.94
R50 503	58.77	86.12	97.64
P25	57.18	87.51	96.00

MB degradation test results strongly depend on properties of TiO₂ (i.e. crystallinity, assembly of phases, crystallite size, oxygen vacancy, Ti⁺⁴/Ti⁺³ ion ratio, specific surface area, morphology, amount of porosity, band gap energy, interfacial charge carrier transfer rate), and operating conditions (light intensity, oxygen amount, initial concentration of solution, amount of catalyst, size and surface area of the beaker, stirring speed, distance between the UV light source and the beaker) (Xu, et al., 1999; Guillen-Santiago, et al., 2010; Etacheri, et al., 2011). In this study, operating conditions were kept constant for all MB degradation experiments. Then, the discrepancies between the MB degradation performances were due to the differences in their morphology and crystal properties of the powders.

It was obvious that MB degradation increases as UV light illumination time is increased for all of the powders composed of different R ratios at all conditions. That is, in as-dried and in calcined forms. As long as photon adsorption

continues at the surface of TiO₂ powder, new hydroxyl radicals are formed at surface (Chen and Dionysiou, 2008). Hydroxyl radicals continue to decompose MB molecules existing in the solution until there is no MB molecule remains. That's why, percentage of MB degradation after 60 min was less than that after 90 min but greater than that after 30 min UV light illumination time for all powders of different R ratio.

When the powders composed of different R ratio in as-dried form were illuminated to UV light, MB degradation commenced and increased as the UV light illumination time increased as seen in Figure 4.34. In general, total MB degradation in as-dried powders increased with increasing R ratio due to the increase in the amount of crystallinity in the powders. A disorder between powders R1 and R3 and between powders R30 and R50 was noted. MB degradation of powder R50 was even less than that of powder R10 at a given UV light illumination time. The highest MB degradation percentage in as-dried powders was obtained in powder R30 as 96.07% whereas, the lowest MB degradation was obtained in powder R3 as 3.19%. A large deviation range in MB degradation among powders was attributed to the extent of crystallinity caused by the difference in the formation routes. The XRD analysis suggested that the powder R3 as-dried was completely amorphous while powder R30 was in crystalline form (see Figure 4.2). As mentioned in Chapter 2, amorphous TiO₂ does not have significant photocatalytic performance. In addition, smaller crystallite size that gets smaller with increasing R ratio in the powders (see Figure 4.14) increases specific surface area. Large specific surface area means more reaction sites since photocatalytic reactions take place at the surface of the particle and favors photocatalytic activity.

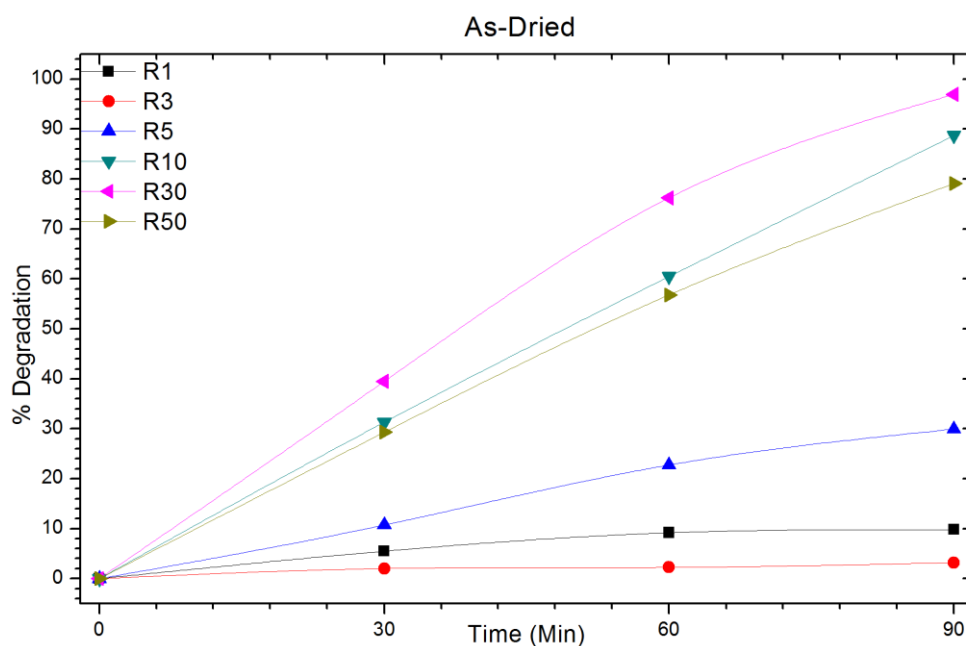


Figure 4.34. Percentage of MB degradation with UV light illumination time for all powders in as-dried form.

Figure 4.35 shows the MB degradation of the powders of different R ratio calcined at 300°C for 1 h. A comparison of MB degradation percentages for the powders of different R ratio before and after calcination revealed that MB degradation increased upon calcination for almost every powder except powder R10 that showed less MB degradation after calcination as compared to its as-dried form. It is obvious that calcination of powders even at 300°C for 1 h, that is the lowest calcination regimes, increased the MB degradation. Etacheri, et al., 2011 reported similar results. Xu et al., 1999 concluded that crystallinity and the crystal assembly affects the degradation rate of the powders. Therefore, the improvement in MB degradation due to calcination was attributed to the increase in percentage of crystallinity. In general, total MB degradation of the 301 series of powders increased with increasing R ratio. However no order could be distinguished between the powders. MB degradation of powder R10 301 was even less than the powders R1 301, R3 301, and R5 301 at a given UV light

illumination time. The highest MB degradation in the 301 series of powders was obtained in powder R30 301 as 99.28% whereas, the lowest MB degradation was obtained in powder R3 301 as 27.74%. A large deviation range in MB degradation among powders was attributed to the crystallite size, and extent of crystallinity caused by the difference in the formation routes. The XRD analysis suggested that the powder R10 301 had the biggest crystallite size among 301 series of powders (see Figure 4.14).

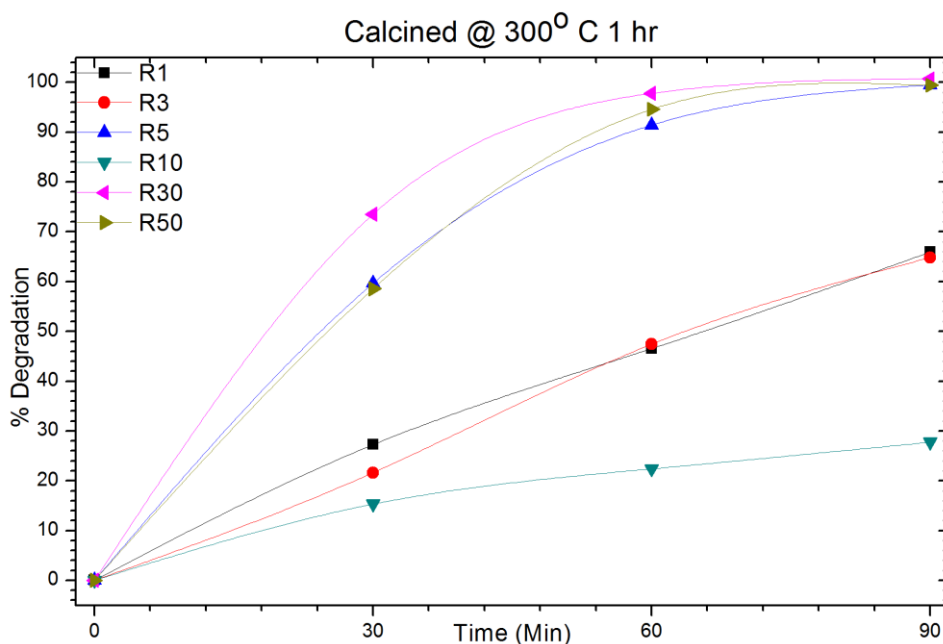


Figure 4.35. Percentage of MB degradation with UV light illumination time for all of the powders after calcination at 300^oC for 1 h.

MB degradation of the powders changed also when R ratio and calcination regimes were changed. For instance, powders R1 and R3 have lesser MB degradation than the other powders of different R ratios for almost every calcination regimes for a given UV light illumination time. The variation in MB degradation with R ratio for the powders calcined in different calcination regimes were shown in Figures 4.36-38. The change in MB degradation with R ratio did not follow an order with increasing or decreasing R ratio, and was

mainly related to the extent of crystallinity in the powders, size of crystallites, and types of crystalline phases present. Increasing water content and MB degradation amount did not show any correlation at 300 series and 400 series powders. However, at 500 series increasing R ratio improved MB degradation performance of the powders.

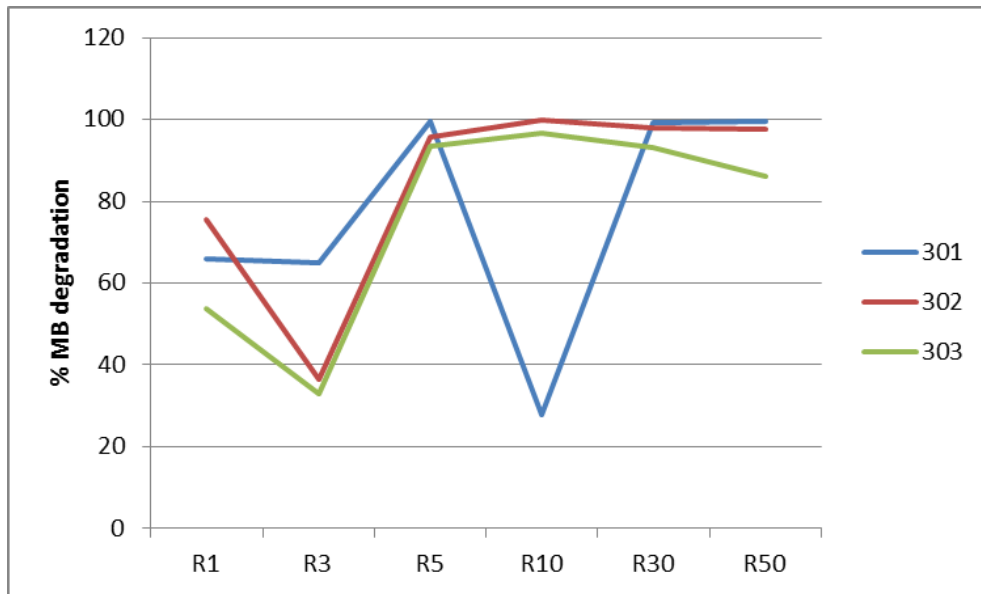


Figure 4.36. Variation in MB degradation with R ratio for the 300 series of powders.

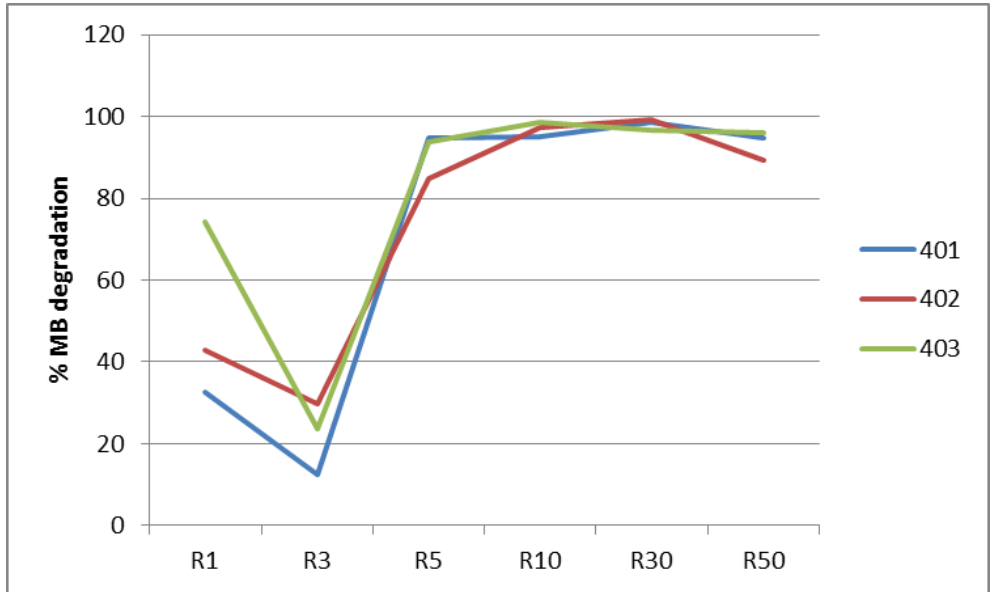


Figure 4.37. Variation in MB degradation with R ratio for the 400 series of powders.

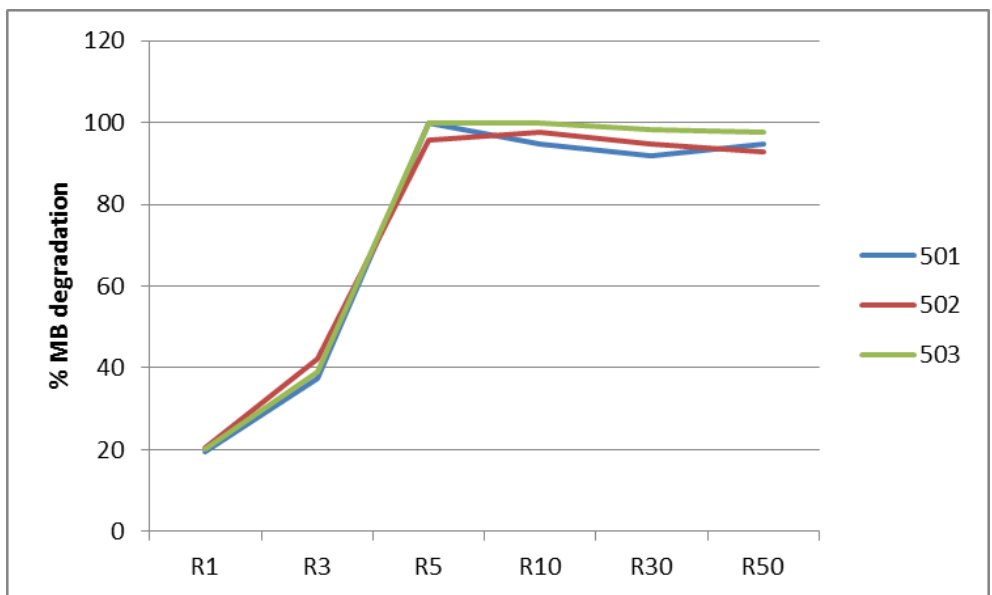


Figure 4.38. Variation in MB degradation with R ratio for the 500 series of powders.

It is commonly known that photocatalytic efficiency is affected by several other parameters such as phase assembly, oxygen vacancy, etc. which depend on calcination conditions. Having high or low calcination temperatures or calcination times leads to changes in the characteristics of the crystalline phases formed during calcination, and do not necessarily provide best photocatalytic performance. Therefore, application of the optimal calcination regimes has critical importance for photocatalytic performance of the powders.

The variation in MB degradation with UV light illumination time for the powders R1, R10, and R50 calcined in different calcination regimes were shown separately in Figures 4.39-41. Powder R1 showed a large deviation range in MB degradation upon calcination in different regimes as seen in Figure 4.39. The lowest degradation percentage was 9.80% for powder R1 as-dried while the highest degradation percentage was 75.55% for powder R1 302. XRD patterns suggested that powder R1 302 was highly crystalline meanwhile, powder R1 as-dried was completely amorphous. Powder R1 302 had 10 nm crystallite size. High crystallinity and formation of high amount of anatase crystals with very small crystallite size led to an improvement in MB degradation in powder R1 302.

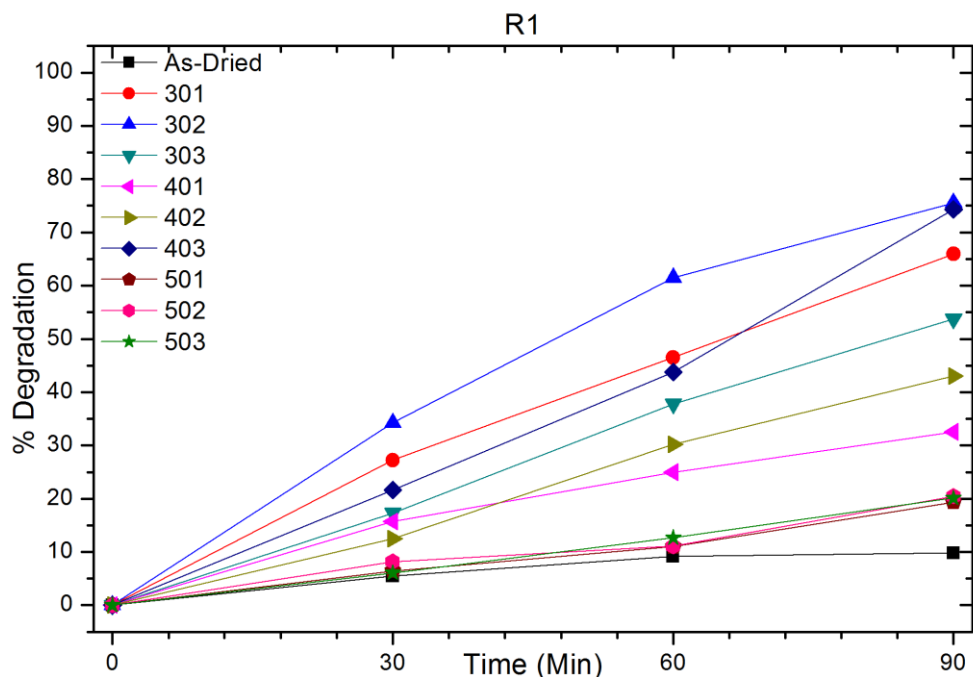


Figure 4.39. Percentage of MB degradation with UV light illumination time for powder R1 for different calcination regimes.

Powder R3 showed a large deviation range in MB degradation upon calcination in different regimes. The lowest degradation percentage was 3.19% for powder R3 as-dried while the highest degradation percentage was 64.84% for powder R3 301. XRD patterns suggested that powder R3 301 was highly crystallized meanwhile, powder R3 as-dried was completely amorphous. Crystallite size of powder R3 301 was 9.3 nm. Formation of high amount of anatase crystals with very small crystallite size resulted in better MB degradation in powder R3 301.

Powder R5 showed a large deviation range in MB degradation upon calcination in different regimes too. There was a large difference between the MB degradation of as-dried and calcined forms of powder R5. The lowest degradation percentage was 29.94% for powder R5 as-dried while the highest degradation percentage was 99.99% for powder R5 501. It is clear that full MB degradation was attained after 90 min UV light illumination of powder R5 501. XRD patterns suggested that powder R5 501 was totally crystalline meanwhile,

powder R5 as-dried was partially crystalline. Crystallite size of powder R5 501 was 19.5 nm and crystallite size of powder R5 as-dried was 5.4 nm. Due to small crystallite size in powder R5 as-dried photocatalytic performance is expected. However, its MB degradation was less than powder R5 501 due to partial crystallization and having lesser oxygen vacancies than powder R5 501.

Powder R10 showed a large deviation range in MB degradation upon calcination in different regimes as seen in Figure 4.40. The lowest degradation percentage was 27.44% for powder R10 301 while the highest degradation percentage was 99.88% for powder R10 302. It is clear that almost full MB degradation was attained after 90 min UV light illumination of powder R10 302. XRD patterns suggested that powders R10 302 and R10 301 are both totally crystalline. Crystallite size of powders R10 302 and R10 301 was the same, 13.1 nm. Band gap energy of powder R10 302 was 3.1 eV while that of powder R10 301 was 3.09 eV. Eventhough there was not much difference in morphology, crystallite size, and band gap energy among these powders, the reason for a large difference in MB degradation between these two powders was not understood and could not be explained at this moment. Nevertheless, MB degradation measurements were repeated once more to clarify whether this difference was caused by experimental error or not. But, again almost the same results were obtained.

Powder R30 showed a little deviation range in MB degradation upon calcination in different regimes. Since as-dried form of the powders was highly crystalline (but still partially crystallized), MB degradation was also high in as-dried form. The lowest degradation percentage was 91.99% for powder R30 501 while the highest degradation percentage was 99.35% for powder R30 402. It is clear that almost full MB degradation was attained after 90 min UV light illumination of powder R30 402. XRD patterns suggested that powders R30 402 and R30 501 are both totally crystalline. Crystallite sizes of powders R30 402 and R30 501 were 14.3 nm and 18.0 nm, respectively. Band gap energy of powders R30 402 and R30 501 was the same, 3.13 eV. Due to its lower crystallite size powder R30 402 has much higher specific surface area than powder R30 501. This might be the reason for the difference in MB degradation between these powders.

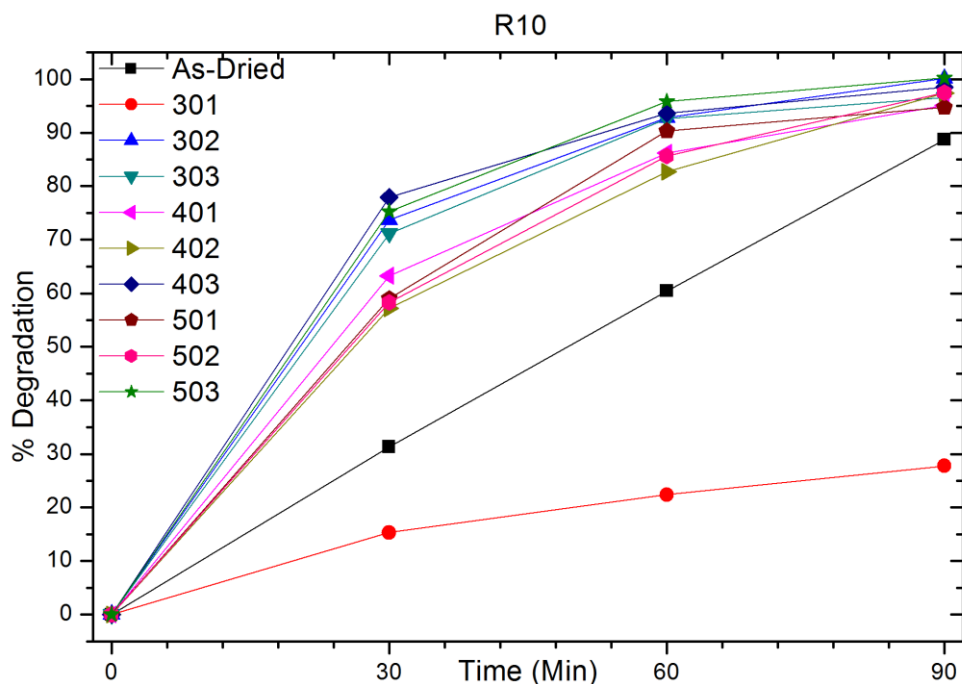


Figure 4.40. Percentage of MB degradation with UV light illumination time for powder R10 for different calcination regimes.

Powder R50 showed a little deviation range in MB degradation upon calcination in different regimes as seen in Figure 4.41. Since as-dried form of the powders was highly crystalline (but still partially crystallized), MB degradation was also high in as-dried form. The lowest degradation percentage was 79.11% for powder R50 as-dried while the highest degradation percentage was 99.41% for powder R50 301. It is clear that almost full MB degradation was attained after 90 min UV light illumination of powder R50 301. XRD patterns suggested that powder R50 301 was totally crystalline while R50 as-dried was partially crystalline. Crystallite sizes of powders R50 301 and R50 as-dried were 11.4 nm and 7.0 nm, respectively. Band gap energies of powders R50 301 and R50 as-dried were 3.03 eV and 3.07 eV, respectively. Powder R50 as-dried had lower crystallite size and band gap energy than powder R50 301. The lower MB degradation of R50 as-dried was attributed to its partial crystallinity.

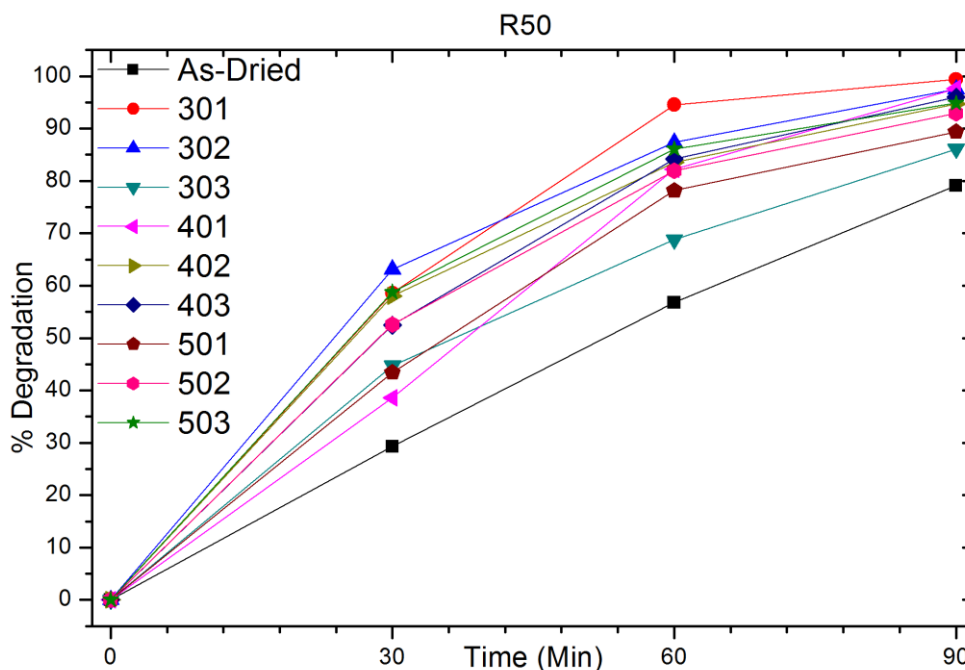


Figure 4.41. Percentage of MB degradation with UV light illumination time for powder R50 for different calcination regimes.

It is apparent that the powders composed of different R ratios and exposed to different calcination regimes are active under UV light illumination in photocatalytic degradation reaction of MB. The UV light source being used during MB degradation test had a single wavelength ($\lambda=365$ nm) that corresponds to an energy of ~ 3.39 eV. Therefore, the energy of the incoming light was greater than the band gap energy of all of the synthesized powders. That means all of the powders synthesized could easily be activated in the UV light source being used during MB degradation test. For that reason, the divergences between the band gap energy of the powders will not have a critical effect in terms of photocatalytic activity.

In view of the fact that no major difference in the morphology based properties like particle size and shape, porosity, and texture, was observed among the synthesized powders upon changing R ratio and calcination regimes, no noteworthy effect of morphology on the photocatalytic activity of the powders

was expected. On the contrary, percentage of crystallinity, phase assembly, and crystallite size were among the utmost importance for photocatalytic activity of the powders synthesized.

Smaller crystallite sizes lead to higher photocatalytic performance as a result of enhanced e^-/h^+ recombination rate via decreasing the distance for charge carriers to reach surface without recombination (Ramaswamy, et al., 2008; Xu, et al., 1999). Oxygen vacancies, formed during calcination, in the structure act as electron traps that lead to decrease in e^-/h^+ recombination rate (Kapusuz, et al., 2013). However, excess oxygen vacancies formed during calcination due to high calcination temperature act as e^-/h^+ recombination center and decreases the photocatalytic efficiency (Etacheri, et al., 2011).

Photocatalytic type of reactions took place at surface of the particles, which means having high specific surface area leads to having more reaction sites. Higher specific surface area can be achieved via decreasing the crystallite and particle size, increasing amount of porosity or by enhancing morphology of the powders (Etacheri, et al., 2011; Guillen-Santiago, et al., 2010).

Band gap energy was another parameter that the photocatalytic efficiency depends on, since it directly affects the photocatalytic activation of powders. As band gap energy decreases, the amount of the portion of EM-spectrum, by which activation of powders can be achieved, broadens (Stengl, et al., 2009). The achieved broadening is important for having visible light applications. As it gets more broadened the visible light response and efficiency increase.

For all R ratios the MB degradation results were more or less in an agreement with each other though there were a few exceptions. For powders R1 and R3 results showed a large deviation range upon calcination. As R ratio got bigger the deviation became smaller. Furthermore, MB degradation increased with increasing R ratio. Powders R3 301, R5 as-dried, and R10 301 showed deviation with respect to the other powders in same R ratio. They were tested once more to check if it is a kind of experimental or operator related error. The final results

were almost the same as that obtained from first measurements. Consequently, there was no error caused by experimental procedure or operator.

Photocatalysis mechanism taking place at the surface of TiO_2 powder was schematically illustrated in Figure 4.42 and could be interpreted in four stages. First stage covers the photon adsorption and charge carrier generation (e^-/h^+ formation). Generated charges are trapped at the hydrated surface functional groups ($\text{Ti}^{\text{IV}}\text{OH}$). Upon trapping of e^- 's, surface trapped conduction band electrons ($\text{Ti}^{\text{III}}\text{OH}$) are formed while trapping of h^+ 's produced surface trapped valance band holes ($\text{Ti}^{\text{IV}}\text{OH}^+$). $\text{Ti}^{\text{III}}\text{OH}$ reacts with O_2 molecule and forms O_2^- ions. $(\text{Ti}^{\text{IV}}\text{OH}^+)^+$ react with H_2O molecule and form OH^- and H^+ ions (Zhang, et al., 1998). In the second stage O_2^- may go further reactions with e^- and newly formed H^+ ions to form active OH^- radicals (Namratha and Byrappa, 2012). Previously and newly formed OH^- radicals react with organic molecules and form CO_2 and H_2O molecules. Third stage is the recombination stage of the produced charges which can be observed in three different forms; e^- and h^+ may react and recombine, e^- can react with $(\text{Ti}^{\text{IV}}\text{OH}^+)^+$, or h^+ can react with $(\text{Ti}^{\text{III}}\text{OH})$ and they both produce $\text{Ti}^{\text{IV}}\text{OH}$ (Zhang, et al., 1998). Last stage is the interfacial charge transfer, which is a much slower process with respect to charge carrier trapping and recombination (Zhang, et al., 1998).

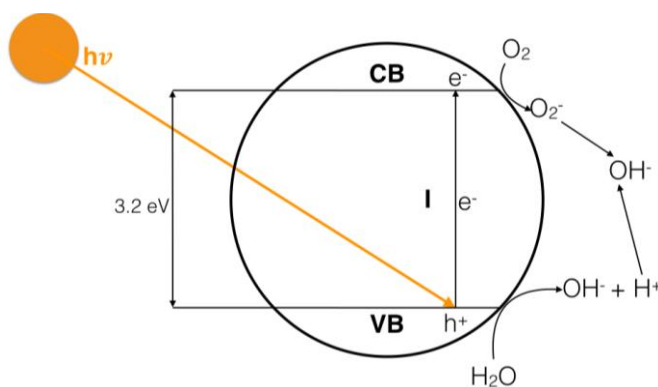


Figure 4.42. Schematic illustration of TiO_2 photocatalysis mechanism.

P25 powder was taken as a reference point and was set as the lower limit of success for photocatalytic testing results of the powders synthesized. When MB degradation of the powders are compared with that of P25, it is obvious that 37 of the total of sixty powders have lower MB degradation than P25, 7 of them have almost the same MB degradation with P25, and 16 of them have higher MB degradation than P25 (see Table 4.9). Although 37 of the powders have lower MB degradation than P25, 5 of them are in as-dried form. The difference between the MB degradation of the remaining 32 powders and that of P25 is not much. For this reason, none of the R ratio and calcination regime could be avoided for determination of the best R ratio and calcination regime for doping conditions from MB degradation data.

MB degradation test has its own weakness. It is high dependence of MB degradation percentage on concentration of the MB solution. In other words, if amount of MB powder in the solution is changed, MB degradation values changes. Therefore, comparison of the powders in terms of the MB degradation results with other researchers studies becomes difficult. In order to, overcome this difficulty, Langmuir-Hinselwood equation (Equation 4.5), which is a first order kinetic reaction equation, was applied to get the rate constants for each powder.

$$\ln \frac{C_0}{C_t} = k_p t \quad \text{Eq. 4.5.}$$

where; C_0 is initial concentration of MB, C_t is MB concentration at given time, k_{ap} is apparent rate constant, and t is time.

According to MB degradation and rate constant values, the best performing powder need to be selected for each R ratio. Then, the best performing powders selected will be tested in daylight for 24 h. Apparent rate constant is very much related to photocatalytic performance of TiO_2 powder. However, it is totally independent of the concentration of the MB solution.

4.4.2. Apparent rate constants

Representative apparent rate constant versus UV light illumination time graphs for the powders R1 and R50 exposed to different calcination regimes were shown in Figures 4.43 and 4.44. Apparent rate constant of P25 was also calculated and indicated in the figures for comparison of the data.

None of the powders R1 and R3 exposed to different calcination regimes showed higher rate constant than P25. None of the rate constant values for the R1 powders were even close to the value of P25. Since the success of the powders was set according to the properties of P25, the powders R1 and R3 were classified as “unsuccessful” in terms of photocatalytic performance. In other words, none of the powders R1 and R3 were able to pass the lower limit set for photocatalytic success.

Powders R5 301, R5 501, R5 503, R10 302, R10 303, R10 403, R10 502, R10 503, R30 as-dried, R30 301, R30 302, R30 401, R30 402, R30 403, R30 503, R50 301, R50 302, R50 403, and R50 503 exhibited higher rate constant than P25. Powders exposed to other calcinations regimes did not surpass the rate constant value of P25 although some of them got very close value to P25. Consequently, powders R5 301, R5 501, R5 503, R10 302, R10 303, R10 403, R10 502, R10 503, R30 as-dried, R30 301, R30 302, R30 401, R30 402, R30 403, R30 503, R50 301, R50 302, R50 403, and R50 503 were classified as “successful” in terms of the photocatalytic performance.

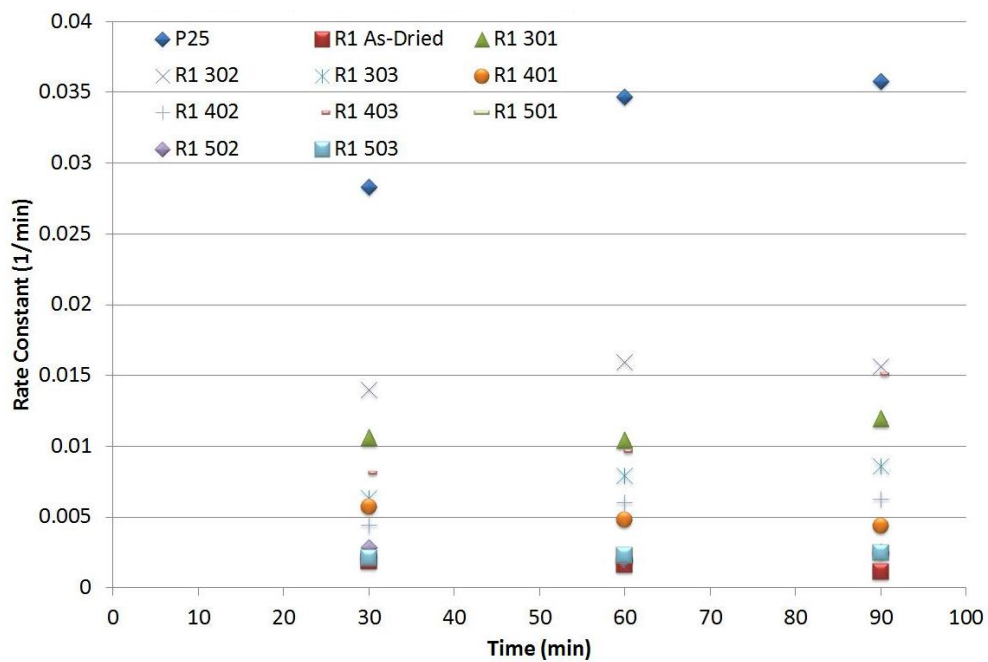


Figure 4.43. Rate constant of powder R1 with respect to UV light illumination time for different calcination regimes.

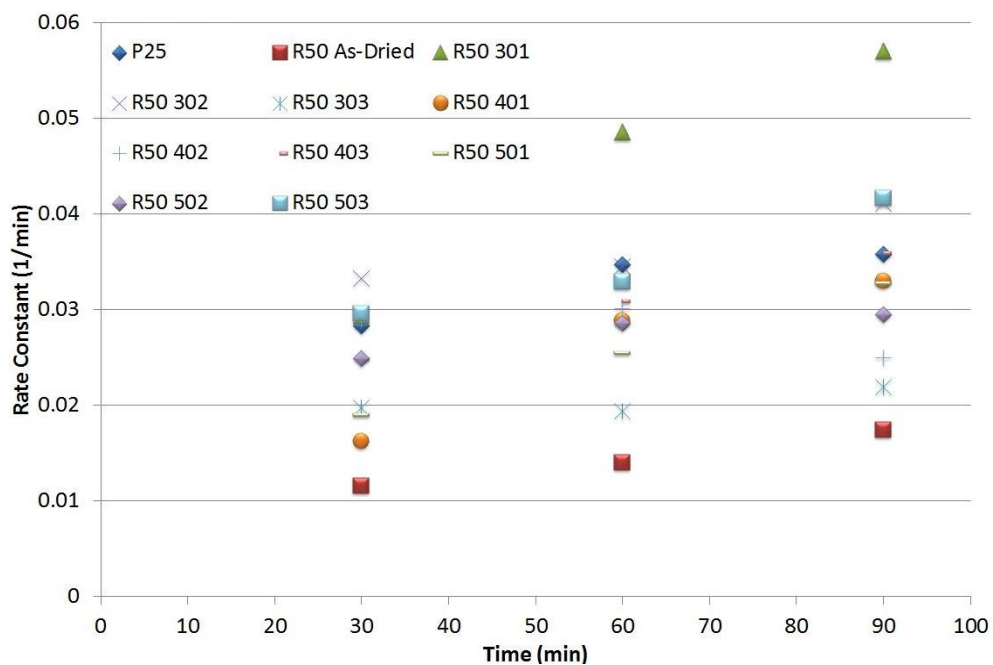


Figure 4.44. Rate constant of powder R50 with respect to UV light illumination time for different calcination regimes.

Photocatalytic performance of the selected powders was determined also by measuring the MB degradation capability of powders in daylight. Photocatalytic measurement was done according to the procedure described in Section 3.3. During the test no artificial light source was employed. The 48 h long testing duration includes both day and night. P25 was also exposed to daylight test along with selected powders for comparison of the data. Rate constants of the powders were calculated for the first 24 h. Data gathered from daylight tests were presented in Table 4.10.

Table 4.10. MB degradation and rate constant of the selected powders in daylight.

Powder Name	% MB Degradation		Rate Constant (1/min)
	After exposure to daylight for 24 h	After exposure to daylight for 48 h	After exposure to daylight for 24 h
P25	95.36	99.02	0.0021
R1 302	70.51	95.39	0.0008
R3 301	50.55	78.71	0.0005
R5 501	83.51	98.67	0.0013
R10 302	81.77	98.71	0.0012
R30 301	89.37	97.09	0.0016
R50 301	94.74	98.26	0.0020

Powder R50 301 showed a MB degradation value very close to the value of P25 in daylight. Powders R30 301, R10 301, and R5 501 showed high MB degradation values too. With an exception of powder R3 301, all other powders showed MB degradation values superior than 95% after 48 h exposure to daylight. Rate constant values calculated from MB degradation test of the powders in daylight for 24 h is shown in Figure 4.45. When a comparison is made between the rate constant values obtained in daylight and UV light illumination, it is obvious that the rate constant values obtained in daylight are quite lesser than the values obtained in UV light illumination as seen in Figure 4.46. The rate constant values obtained in daylight reveals that chemical and/or

physical improvements are necessary in order to get better photocatalytic performance in daylight.

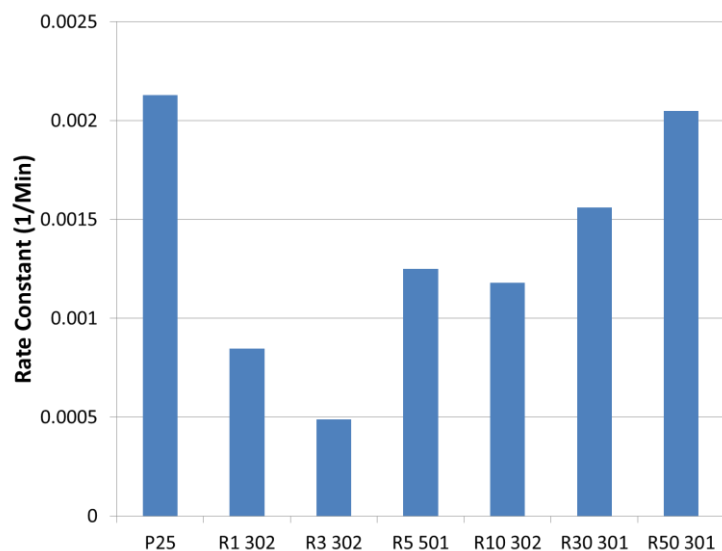


Figure 4.45. Rate constant values calculated from MB degradation test of the powders in daylight for 24 h.

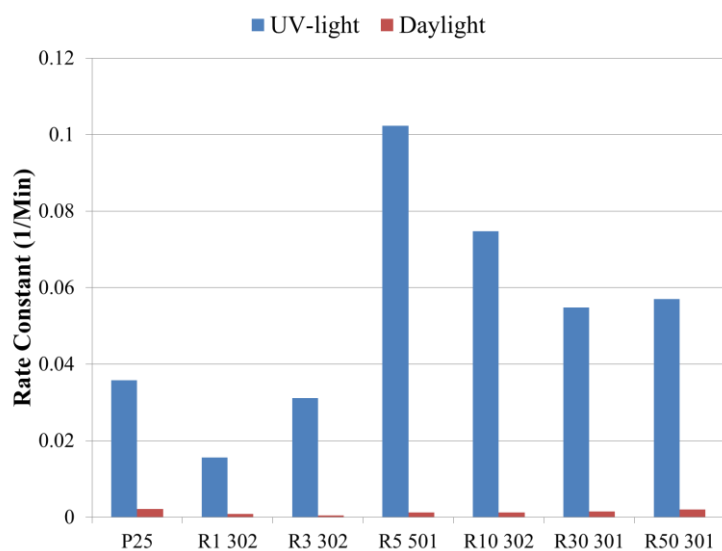


Figure 4.46. Comparison of rate constant values calculated from MB degradation tests of the powders in UV light and in daylight.

Results presented in this manuscript for undoped TiO₂ were superior to the ones given in literature. Kapusuz et al., 2013 synthesized TiO₂ powders via non-hydrous sol-gel procedure, where MB degradation was reported as 50% and 64% for calcination temperatures of 400 and 500°C, respectively. Yao et al., 2010 studied photocatalytic properties of TiO₂ powders produced by sol-gel synthesis and obtained ~50% MB degradation. Etacheri et al., 2011 reported 57.09% degradation on sol-gel synthesized TiO₂ powders. Lastly, Houas et al., 2001 tested P25 under two different wavelengths (290 and 340 nm) and reported 97.78 and 89.46% degradation, respectively. MB degradation of the powders synthesized in this study were, in general, better than MB degradation percentages reported for TiO₂ powders in literature.

All in all, it has been proved that only by changing water content in the mother solution and calcination regime, it is possible to synthesize visible light active TiO₂ powders via sol-gel process. However, daylight rate constants were very small when compared to UV light performance. Therefore, doping was applied to improve the performance of the TiO₂ powders in daylight. Before doping, best water content and calcination regime were determined according to requirements listed below.

- High photocatalytic activity in UV light exposure
- Better rate constant than P25 in UV light exposure
- Small crystallite size
- Smaller band gap energy than P25.

4.5. Determination Of Best R Ratio And Calcination Regime

In order to determine the best R ratio and calcination regime, properties and characteristics of P25 was taken as a reference. First, six of the sixty total undoped TiO₂ powders namely; R1 302, R3 301, R5 501, R10 302, R30 301, and R50 301 were selected because they exhibited relatively high MB degradation in

the R ratios that they belong to (see Table 4.11). Powders formed in two different routes. That is, for powders R1, R3, R5, and R10 gelation and for powders R30 and R50 precipitation were observed during powder formation. Best R ratio has been determined by evaluating the performance of the six powders according to the requirements listed above.

Among the six powders selected, four of them (R5 501, R10 302, R30 301 and R50 301) showed better rate constant than P25 under UV light illumination though their photocatalytic performance was not as good as that of P25 in daylight. Getting better rate constant than P25 in UV light is an important achievement in terms of photocatalytic performance.

Third evaluation was done according to the assessment of their crystallite sizes. All of the selected powders had relatively low crystallite size and composed of only anatase phase. Since all powders are composed of the same phase, their crystallite size plays an important role for photocatalytic performance due to the fact that the smaller the crystallite size, the better the photocatalytic properties (Ramaswamy, et al., 2008). Powder R5 501 showed largest crystallite size since it was calcined at 500°C while the others were calcined at lower temperatures.

The utmost goal of this study was to get visible light active powders with high photocatalytic activity. Then, last evaluation was done according to the comparison of their band gap energy values of the remaining powders. Band gap energy is an important consideration because as it decreases the portion of the solar spectrum from which photocatalytic reactions make use of increases. Having small band gap energy values was considered as a vital indication of the better photocatalytic performance.

Consequently, the evaluation of the powders according to the predetermined requirements suggested that powder R50 301 was the best performing undoped TiO₂ powder in terms of photocatalytic performance. Therefore, B and Zr doping were done only for powders composed of R ratio of 50.

4.6. Synthesis Of Doped TiO₂ Powders

The B doped, Zr doped, B and Zr co-doped TiO₂ powders were synthesized through the experimental procedure described in Section 3.1.2. The B doped TiO₂ powders appeared in white color both in as-dried and calcined forms. Zr-doped and B and Zr co-doped powders were in yellowish color at as-dried form but their colors changed to white after calcination. Colmenares, et al., 2006 and Patil, 2008 reported similar results for Zr doped TiO₂ powders.

These powders were synthesized by alkoxide sol-gel precipitation in powders R50. Powders were formed according to the principles and reactions given in Section 4.2.

4.7. Characterization Of Doped TiO₂ Powders

4.7.1. pH Measurements

The results of measured pH values of the initial solutions for variable doping contents were listed in Table 4.11.

Table 4.11. pH values of the doped solutions.

Solution	pH
R50	3
R50-2B	2~3
R50-3B	2~3
R50-4B	2~3
R50-5Zr	3
R50-10Zr	3
R50-15Zr	3
R50-3B-10Zr	2~3

Although the pH Zr doped R50 powder's solution stayed steady, with respect to solution of undoped R50 powder, a slight decrease in pH was observed in mother solutions of B doped and co-doped powders. For B doping boric acid was

occupied, while zirconium acetylacetonate was employed for Zr doping. Acid dissociation constant values for boric acid and Zr-acac were 9.23 and 9.8 respectively. Therefore, the pH decrease observed in the B employed solutions was attributed to lower pKa of boric acid.

4.7.2. Viscosity Measurements

Doping precursors were dissolved in a mixture of ethanol and glacial acetic acid. As a result, the amount of alcohol in the mother solution increased. Viscosity increased slightly with respect to the solution of undoped R50 powder, in solutions of both doped and co-doped powders. Viscosity values of ethanol and acetic acid are very low (1.2, 1.219 cP, respectively). Therefore, the slight increase in the viscosity of the solutions of the doped powders might be owed to the addition of doping precursors (boric acid, zirconium acetylacetonate), which were dissolved in ethanol and acetic acid. The measured viscosities of the initial solutions were listed in Table 4.12.

Table 4.12. Viscosity values of B or Zr doped and B and Zr co-doped powder solutions for R50 compositions.

Solution	Viscosity (cP)
R50	32.8
R50-2B	35.8
R50-3B	34.7
R50-4B	36.7
R50-5Zr	33.7
R50-10Zr	33.5
R50-15Zr	35.3
R50-3B-10Zr	31.7

In the beginning, the viscosity values of the solutions suggest high crystallinity in as-dried powders, because nucleation rate highly depends on viscosity. However, addition of doping agents to the mother solution did not change the

viscosities significantly. Then, the variation in nucleation rate may be caused by the changes occurred in other parameters, which depend on composition of the solution. Therefore, addition of extra alcohol and doping agents to the system caused some changes in C_0 , γ , ΔG_v , ω , and r parameters. Since, measurements of these parameters are not in the scope of this study, further discussion based on nucleation rate won't be conducted. However, the effects of doping agents on crystal formation were discussed in detail comparing the as-dried, 301, and 501 calcination conditions of powder R50 at XRD analyses.

4.7.3. X-Ray Diffraction (XRD)

The crystallization characteristic of solutions of doped powders does not only depend on viscosity, but also the other parameters as highlighted in Section 4.7.2. The comparison of Table 4.12 and diffractograms of B doped, Zr doped, and B and Zr co-doped powders in as-dried form clarify this statement. The measured viscosity values suggested similar crystallinity values for both doped and co-doped powders in as-dried form with respect to undoped as-dried form. However, only B doped R50 powders in as-dried form showed as high crystallinity as expected. Zr doped or B and Zr co-doped R50 powders were completely amorphous in as-dried form. B and Zr are reported to inhibit crystallization of powders (Kapusuz et al., 2013). As a result of not having expected crystallinity at as-dried forms of Zr-doped and co-doped powders. Calcinations were done at 500°C for 1 h. Total crystallization was observed at powders in 501 conditions. Then, 3wt% B and 10wt% Zr doped and 3wt%B and 10wt% Zr co-doped powders were calcined at 300°C for 1 h, to check if total crystallization can be achieved at 300°C calcination temperature. Yet, co-doped powders were amorphous, B or Zr doped powders were partially crystallized. But, during the discussion part the results were given in the order of increasing calcination temperature.

X-ray diffractograms of undoped and B-doped R50 powders in as-dried form are shown in Figure 4.47. XRD analyses of the synthesized powders revealed that all

B doped powders with R50 composition were partially crystallized and composed of anatase crystals in as-dried form. The phase was characterized by the characteristic peak of (101) plane at 2θ of $\sim 25.3^\circ$ (JCPDS #21-1272). B atoms are known to inhibit crystallinity (Zaleska, et al., 2008). As a result, percent crystallinity values decreased by increasing B content as listed in Table 4.13.

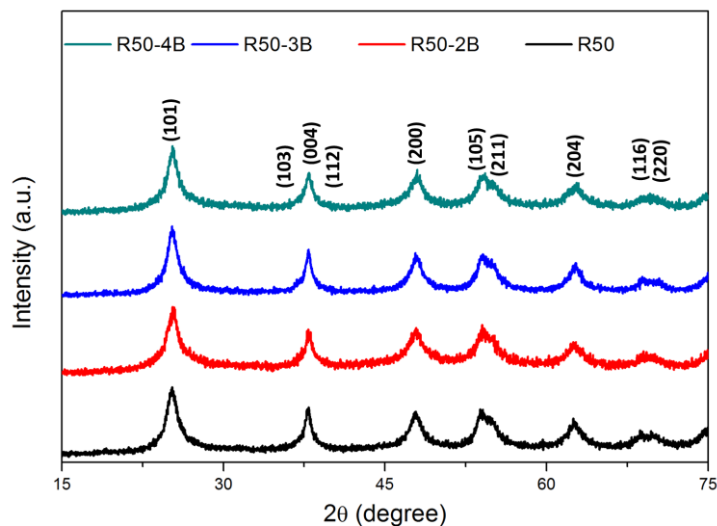


Figure 4.47. XRD patterns of B-doped TiO_2 powders in as-dried form.

X-ray diffractograms of the Zr doped TiO_2 powders in as-dried form did not reveal any crystallinity as shown in Figure 4.48. In other words, the addition of Zr ions inhibited crystallization of Zr doped R50 powders in as-dried form, significantly (Colmenares, et al., 2006). As a result, Zr doped R50 powders did not reveal any crystallinity in as-dried form. The viscosities of the solutions Zr doped powders were almost equal to that of solution of undoped R50 powder. This controversial result can only be explained by change occurred in ΔG_v , γ , C_0 , ω , and r parameters, due to addition of doping agents.

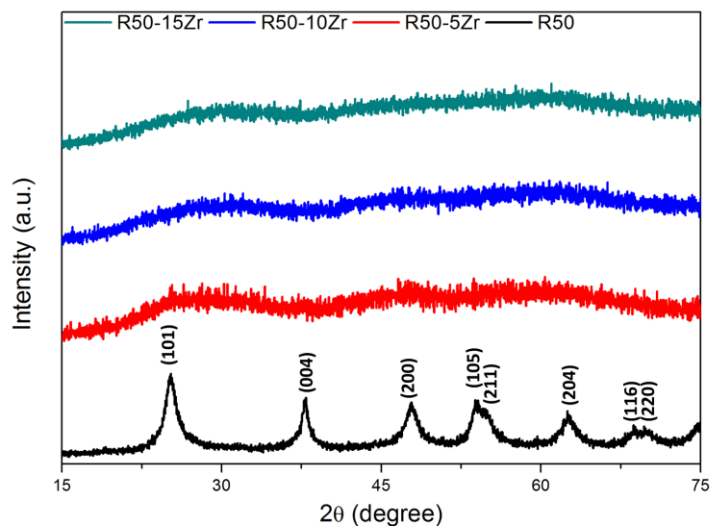


Figure 4.48. XRD patterns of Zr-doped as-dried TiO_2 powders.

The degrees of crystallinity of the synthesized TiO_2 powders in as-dried form were calculated from the X-ray diffractogram of the undoped, B doped and Zr doped powders, listed in Table 4.13. Increasing B amount in the solution decreased the % crystallinity of powders, as reported by Wu, et al., 2010. Addition of Zr doping agents inhibited the crystallization that powders of Zr doped R50 in as-dried form were fully amorphous. Xue, et al., 2013 reported similar changes in crystallization amount occurring with addition of doping agents. Zirconium caused more inhibition of crystallization than B atoms, due to its much larger ionic radius (see Table 2.2). Moreover, it can form O-Zr-Ti bonds in the structure.

B doped R50 powders showed high crystallinity as given in Table 4.13. Rietveld refinement was performed for B doped R50 powders in as-dried form. XRD data was very noisy, and amorphous phase was also present in the structure. Therefore, sensitive parameters (i.e. atomic position, lattice parameter) were not refined. The results of Rietveld refinement were given in Figure 4.49 and in Table 4.14. The Rietveld refinement results of undoped R50 powder in as-dried form were also given to see the changes occurred on crystal structure as a result of doping.

R50 powders in as-dried form showed no crystallinity upon Zr doping at all; so, Rietveld refinement was not conducted for them.

Table 4.13. %Crystallinity values of undoped and B doped and Zr doped as-dried TiO₂ powders with compositions of R50.

Powder	% Crystallinity
R50 As-Dried	70.44
R50-2B	71.30
R50-3B	60.52
R50-4B	51.81
R50-5Zr	~0
R50-10Zr	~0
R50-15Zr	~0

Table 4.14. Rietveld refinement results of undoped and B-doped TiO₂ powders in as-dried condition.

Sample	R50 As-Dried	R50-2B	R50-3B	R50-4B
χ^2	0.2200	0.2059	0.2187	0.1849
Rp	0.0860	0.1106	0.1092	0.0977
wRp	0.1117	0.1425	0.1361	0.1256
Crystallite Size (nm)	6.8	7.4	6.7	6.6

General remarks and outcomes for the analyses of B doped R50 powders in as-dried form are as follows:

- Upon doping, fitting quality (χ^2 , Rp, wRp) did not vary significantly with respect to undoped TiO₂ powder's fitting.
- Crystallite sizes showed change depending on varying doping percentages. For 2wt% doping, crystallite size increased slightly. However, with increasing doping amount crystallite size got smaller and decreased below that of undoped R50 powder in as-dried form. Increasing dopant amount leads to increasing amount of unsuccessfully doped B atoms. Therefore, the reason of decreasing crystallite size with increasing dopant amount is probably the result of the B atoms that cannot be doped successfully and segregated to the crystallite boundaries, that inhibits the crystal growth (Rahaman, 2007).

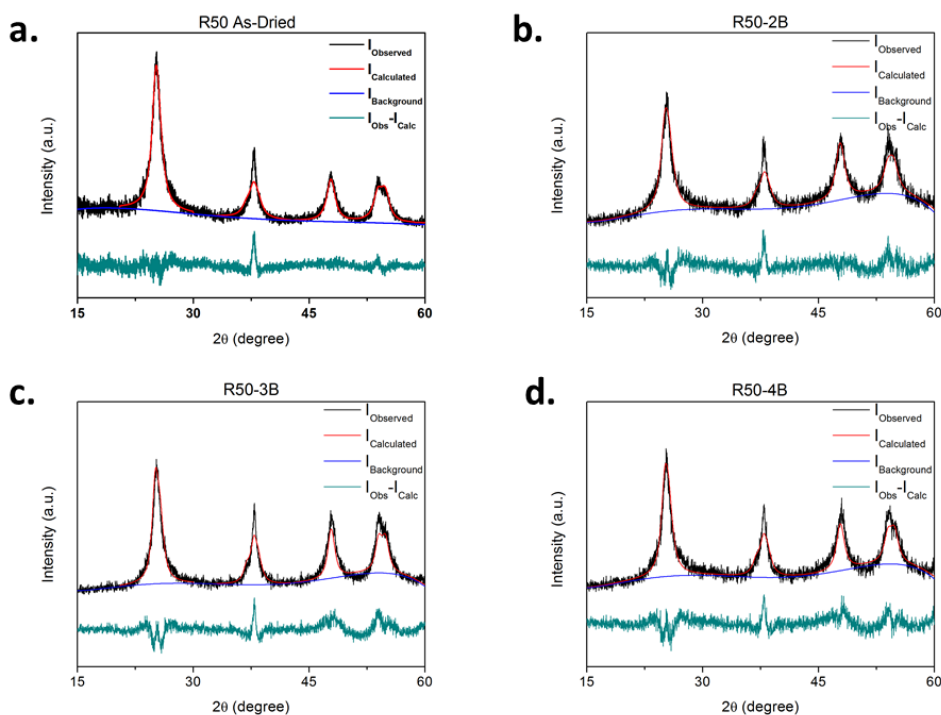


Figure 4.49. Rietveld fittings of a. R50 As-Dried, b. R50-2B, c. R50-3B, d. R50-4B.

The X-ray diffractogram of the B-doped TiO₂ powder, which was calcined at 300°C revealed that this powder was partially crystallized and composed of anatase crystals as seen in Figure 4.50. The phase was characterized by the characteristic anatase peak of (101) plane at ~25.3° (JCPDS #21-1272). No brookite, rutile, B₂O₃, or TiB₂ formation was observed within the limitations of Bragg-Brentano Cu-Kα radiation. Upon calcining at 300°C for 1h, R50-3B increased its crystallinity from ~60.52% to ~71.86%, as listed in Table 4.15. Zhang et al., 2012, published powders having similar degrees of crystallinity for same chemical composition and calcination condition. Moreover, the crystallite size of the R50-3B-301 powder was equal to two-thirds of the R50 301 powder.

Table.4.15. %Crystallinity values of R10 and R50 powders in undoped, B doped, and Zr doped 301 form.

Powder	% Crystallinity
R50 301	~ 100
R50-3B-301	~ 71.86
R50-10Zr-301	~ 35.22

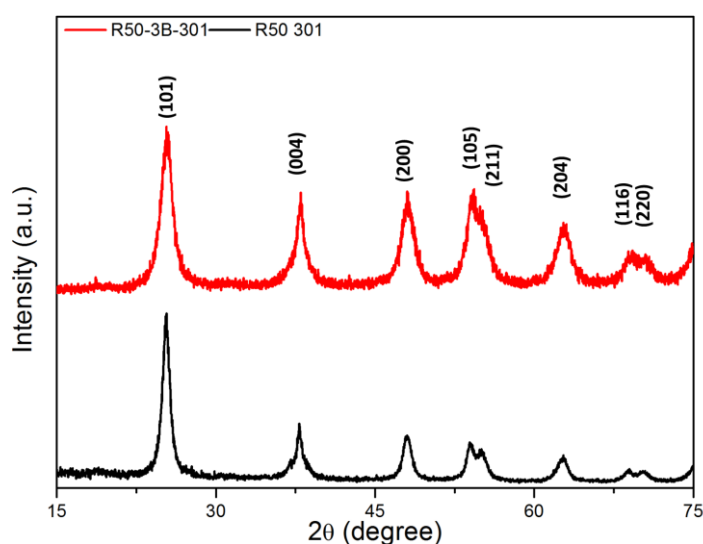


Figure 4.50. XRD patterns of B-doped 301 TiO₂ powders.

X-ray diffractograms of the Zr doped TiO₂ powders calcined at 300°C revealed that R50-10Zr-301 was partially crystallized and its crystals were only composed of anatase crystals as seen in Figure 4.51. The phase was characterized by the characteristic anatase peak of (101) plane at ~25.3° (JCPDS #21-1272). No brookite, rutile, or ZrO₂ formation was observed. Upon calcination at 300°C for 1 h, the degree of crystallinity of R50-10Zr-301 powders increased to ~35.22%. The phase observed at partially crystallized powders was anatase phase.

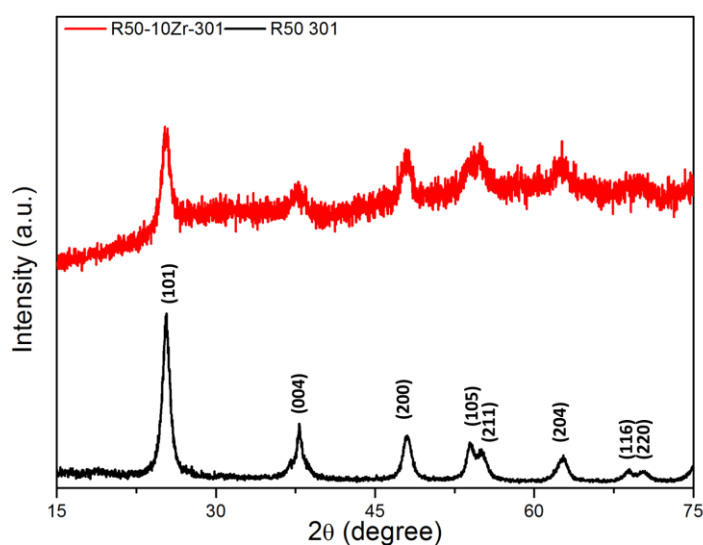


Figure 4.51. XRD patterns of Zr-doped 301 TiO₂ powders.

B doped R50 powder in 301 form showed high crystallinity as given in Table 4.15. Yet, still not enough for refining the lattice parameters or atomic positions. The Rietveld refinement results of R50-3B-301 were given in Figure 4.52 and tabulated in Table 4.16 with the results of undoped powder R50 in 301 condition to see the changes on crystal structure, occurred as a result of doping.

The XRD data of R50-10Zr-501 is, still, too noisy that the crystallite size or lattice parameter calculations could not be done by Rietveld refinement.

General remarks and outcomes of the analyses of R50 301 and R50-3B-301 TiO₂ powders are as follows:

- Upon doping, χ^2 increased three times that of undoped case. Moreover, slight change, which is not as severe as χ^2 , is observed at Rp and wRp.
- The crystallite size showed significant change at 301 conditions upon 3wt% B doping. At 301 condition both of the undoped and doped powders are highly crystalline. Zaleska, et al., 2008 reported B addition inhibits growth of the formed crystals. The calculated crystallite size of the doped powder is almost two-thirds of the size of undoped powder. Kapusuz et al., 2013, published decrease at crystallite size upon B doping. The decrease occurring at crystallite size of TiO₂ upon doping is probably the result of the unsuccessfully doped B atoms segregation at crystal boundaries (Rahaman, 2007).

Table.4.16. Rietveld refinement results of undoped and B-doped TiO₂ powders in 301 condition.

Sample	R50 301	R50-3B-301
χ^2	0.1221	0.3491
Rp	0.0873	0.1378
wRp	0.1138	0.1705
Crystallite Size (nm)	11.2	8.9

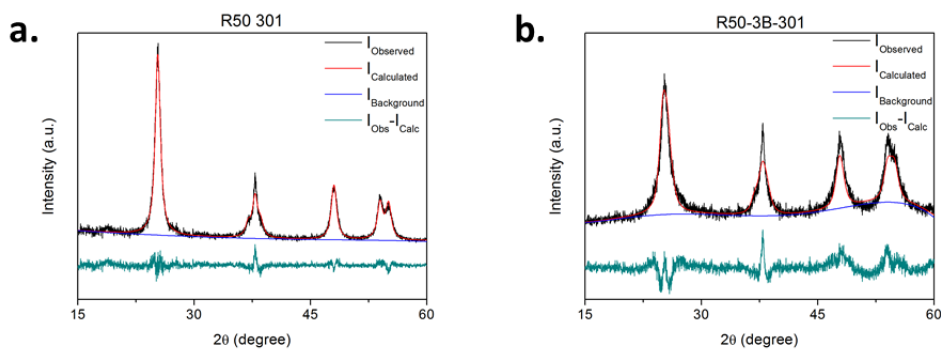


Figure 4.52. Rietveld fittings of a. R50 301, b. R50-3B-301.

The X-ray diffractograms of the B doped TiO_2 powders calcined at 500°C revealed that crystallization was completed for all of the powders, and they were only composed of anatase crystals as seen in Figure 4.53. The phase was characterized by the characteristic anatase peak of (101) plane at 2θ of $\sim 25.3^\circ$ (JCPDS #21-1272). No brookite, rutile, B_2O_3 , TiB_2 formation was observed at any of the calcined powders. As a result of, calcination at 500°C crystallite sizes of the powders were increased, more rapidly than in 301 condition. Peak positions showed slight shift to the right, upon B doping, with respect to undoped R50 in 501 calcination condition. The reason of the shift is the change of lattice parameter due to the entrance of the doping agents to the lattice interstitially. This change can be observed in **Figures 4.47, 4.50 and 4.53**. B atoms form new bonds with nearest three 'O' atoms upon interstitial doping to the TiO_2 lattice, as given in Figure 4.54 (Geng, et al., 2006). Therefore, newly formed bonds might lead to some decrease in lattice parameters.

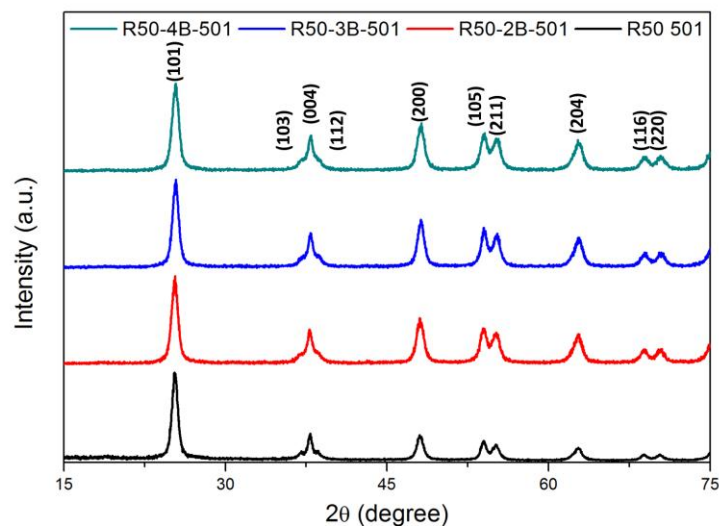


Figure 4.53. XRD patterns of B-doped 501 TiO₂ powders.

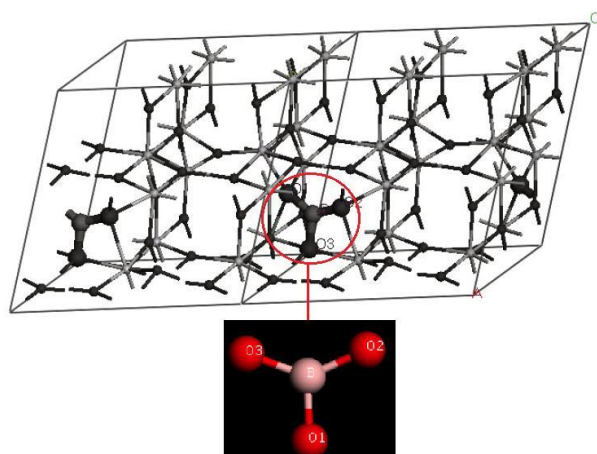


Figure 4.54. Interstitial doping of B to the lattice structure (Geng, et al., 2006).

B doped R50 powders completed crystallization, calcining at 500°C for 1 h, irrespective of the amount of doping agent. The Rietveld refinement results are given in Figure 4.55 and in Table 4.17 with the results of R50 501 powder for revealing the effect of doping. The crystal structure of R50-3B-501 was constructed with the obtained results in Figure 4.56.

Table 4.17. Rietveld refinement results of undoped and B-doped TiO₂ powders in 501 condition for R50 composition.

Sample	R50 501	R50-2B-501	R50-3B-501	R50-4B-501	
χ^2	0.0965	0.1622	0.1648	0.1505	
Rp	0.0921	0.1113	0.1172	0.1029	
wRp	0.1200	0.1454	0.1525	0.1314	
a=b (Å)	3.78	3.78	3.77	3.79	
c= (Å)	9.51	9.50	9.49	9.50	
Vol (Å ³)	135.88	135.74	134.88	136.46	
Atomic Positions (x, y, z)	Ti	(0.0000, 0.7500, 0.1250)			
	O	(0.0000, 0.7500, 0.3333)	(0.0000, 0.7500, 0.3334)	(0.0000, 0.7500, 0.3343)	(0.0000, 0.7500, 0.3386)
	B	(-, -, -)	(0.0000, 0.7500, 0.5217)	(0.0000, 0.7500, 0.5278)	(0.0000, 0.7500, 0.5703)
Crystallite Size (nm)	16.4	17.2	16.9	15.3	

General remarks and outcomes from the analyses of R50 501, R50-2B-501, R50-3B-501 and R50-4B-501 TiO₂ powders are as follows:

- Upon doping, χ^2 increased two times that of undoped case. Rp and wRp values showed slight increase.
- B atoms entered the titania's lattice structure interstitially as shown in Figure 4.56. Lattice parameters exhibited a slight decrease. Since, interstitially entered B atoms form new bonds, lattice parameter decrease is attributed to those newly formed bonds. Increasing B doping amount lead to decrease in lattice parameter, which means of more interstitial sites were occupied by B atoms.

- Crystallite sizes decreased with the increasing amount of doping agent. However, comparing with crystallite size of R50 501. Crystallite sizes increased above at 2 and 3wt% B doping, and at 4wt% B doping crystallite size decreased below. Crystallite size values are listed in Table 4.17. The crystallite size increase at 2 and 3wt% B doping might be the result of successful doping of B atoms. On the other hand, at 4wt% doping crystallite size got smaller, it is probably the result of the decrease of efficiency of B doping occurring to the lattice, and segregation of the unsuccessfully doped B atoms to the boundaries.

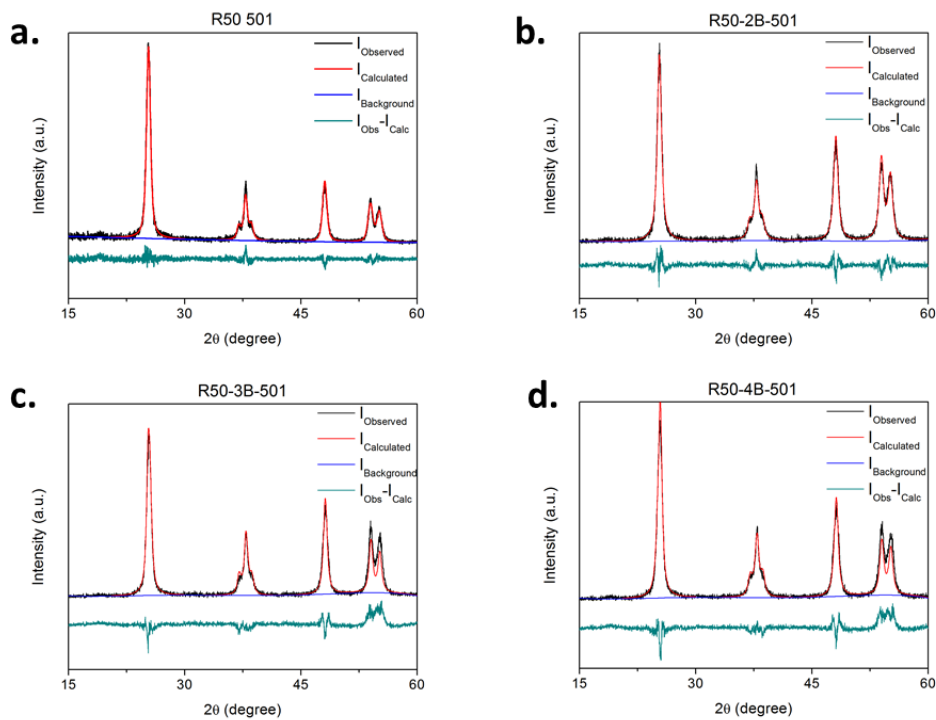


Figure 4.55. Rietveld fittings of a. R50 501, b. R50-2B-501, c. R50-3B-501, d. R50-4B-501.

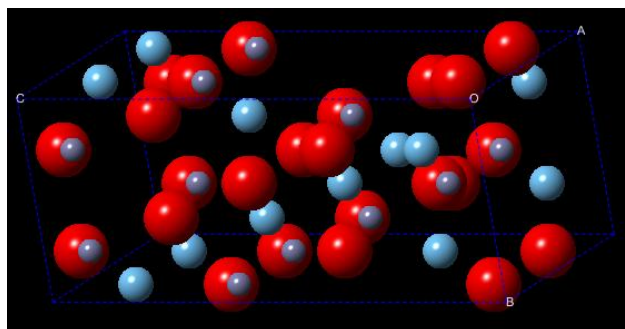


Figure 4.56. Constructed crystal structure of R50-3B-501 according to Rietveld refinement results (Blue atoms are titanium, red atoms are oxygen and grey atoms are boron).

As-dried and 301 forms of B doped R50 powders showed high crystallinity. Lattice parameters decreased at all of the B doped powders at 501 calcination condition with respect to R50 501. Yet, crystallite sizes with respect to R50 501 powder, increased at R50-2B-501, and R50-3B-501 powder; then, a significant decrease at R50-4B-501 powder. It might be the result of having less doping efficiency upon saturation of interstitial sites at R50-4B-501 powder. Therefore, in the light of the information gathered from XRD analyses, wt% doping saturation point have to be above 3 but below 4wt% for B doping. Rehman, et al., 2009 stated that after addition of certain amount of B to TiO_2 structure, B_2O_3 formation is observed. The boron oxide formation is not favored in the structure, because B_2O_3 has a band gap of 6.3.eV and it decreases the photocatalytic performance (Zaleska, et al., 2008).

Aim of doping was to have high visible light response at TiO_2 powders. As a result, having smallest band gap has severe importance. Band gap energies of R50-2B-501, R50-3B-501, and R50-4B-501 were 3.15, 3.09, and 3.13 eV, respectively. Moreover, photocatalytic performances of these powders under UV-light exposure have severe importance. Because the light employed, during MB degradation under UV-light tests, has a wavelength by which all of the synthesized powders can easily be photocatalytically activate. Photocatalytic

performances under UV-light exposure are 86.58% for R50-2B-501, 94.57% for R50-3B-501, 95.18% for R50-4B-501. MB degradation results of 3wt% B doped and 4wt% B doped powders had very close performances. Yet, band gap of 3wt% B doped powders is below that of 4wt% B doped powder. As a result of having high UV-light performance and lowest band gap value 3wt% B was chosen as the optimum doping percentage for co-doping purpose. Akpan and Hameed, 2010, and Zhang et al., 2012, published that they have achieved the best photocatalytic performance at around 3wt% B doping. In the following parts of the characterization, 2wt% B and 4wt% B doped powders will not be evaluated.

X-ray diffractograms of the Zr doped TiO₂ powders calcined at 500°C revealed that all of the powders, irrespective of doping percentage, completed crystallization and those crystals are composed of only anatase phase as seen in Figure 4.57. Colmenares, et al., 2006 found that transition metal doped powders complete their crystallization at 500°C via thermal analysis. The phase was characterized by the characteristic anatase peak of (101) plane at 2θ of ~25.3° (JCPDS #21-1272). No brookite, rutile, ZrO₂ formation is observed. Crystallite size decreased at Zr doped R50 powders in 501 condition with respect to R50 501 powder. Shifting of the peak positions to left side is observed, which is the result of lattice parameter increment. Lukac, et al., 2007 attributed the lattice expansion to Zr⁺⁴ substituting Ti⁺⁴ upon doping, since Zr⁺⁴ ions have larger ionic radius than Ti⁺⁴ ions (see Table 2.2.).

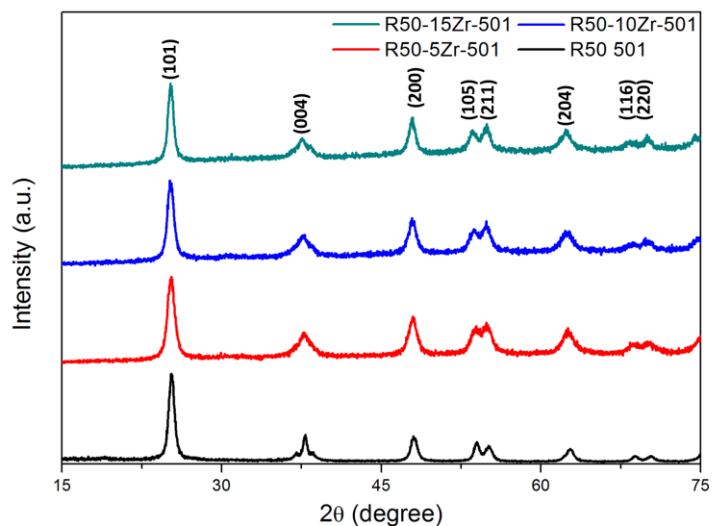


Figure 4.57. XRD patterns of Zr-doped 501 TiO₂ powders.

Zr doped R50 powders showed complete crystallization, upon calcination at 500°C for 1 h, irrespective of the doping agent amount. The Rietveld refinements were conducted and results were given in Figure 4.58 and in Table 4.18 with the results of R50 501 powder to see the effect of doping on crystal structure. The crystal structure of R50-10Zr-501 was constructed in Figure 4.59 with the results obtained after Rietveld refinement.

Table.4.18. Rietveld refinement results of undoped and Zr-doped TiO₂ powders in 501 condition for R50 composition.

Sample	R50 501	R50-5Zr-501	R50-10Zr-501	R50-15Zr-501	
χ^2	0.0965	0.1330	0.1758	0.0946	
Rp	0.0921	0.0808	0.0659	0.0649	
wRp	0.1200	0.1034	0.0841	0.0821	
a=b (Å)	3.78	3.79	3.80	3.80	
c= (Å)	9.51	9.52	9.53	9.53	
Vol (Å ³)	135.88	136.75	137.13	137.13	
Atomic Positions (x, y, z)	Ti	(0.0000, 0.7500, 0.1250)			
	O	(0.0000, 0.7500, 0.3333)	(0.0000, 0.7500, 0.3291)	(0.0000, 0.7500, 0.3365)	(0.0000, 0.7500, 0.3363)
	Zr	(-, -, -)	(0.0000, 0.7500, 0.1250)		
Crystallite Size (nm)	16.4	15.4	14.3	14.0	

General remarks and outcomes from the analyses of R50 501, R50-5Zr-501, R50-10Zr 501 and R50-15Zr-501 TiO₂ powders are as follows:

- Upon doping, χ^2 increased for 5 and 10wt% Zr doped R50 powders in 501 calcination condition. On the other hand, 15wt% Zr doped powder's χ^2 decreased. However, Rp and wRp values decreased at all powders.
- Zr doped R50 powders calcined at 500°C for 1 h, all of the powders showed substitutional Zr doping by replacing the Ti⁺⁴ ions as seen in Figure 4.59 (Lukac et al., 2007; Kapusuz et al., 2013).
- Lattice expansion also supports the substitutional doping of Zr atoms to the TiO₂ system (Tokmakci et al., 2013; Lukac et al., 2007).

- Lattice parameters are same for R50-10Zr-501 and R50-15Zr-501, while crystallite size of R50-15Zr-501 is 0.3 nm smaller than R50-10Zr-501. The same lattice parameter values might mean, after 10wt% no further Zr entrance was occurred to TiO₂ lattice at R50-15Zr-501. The decrease observed in crystallite size supports this idea. It is the result of unsuccessfully doped Zr atoms, which segregated to the boundary and decrease the growth rate of the crystals, as reported by Lukac, et al., 2007.
- Crystallite sizes were smaller than in R50 501 at Zr doped powders in 501 condition. Moreover, crystallite size decreased with increasing amount of Zr doping. Lukac et al., 2007, published crystallite size of 2.5wt% Zr doped TiO₂ powders, with R of 30 and calcined at 500°C, as 20 nm. Previously stated “Zr doping decreases crystallite size at TiO₂ structure (Lukac, et al., 2007; Binitha, et al., 2013)” fact is still valid.

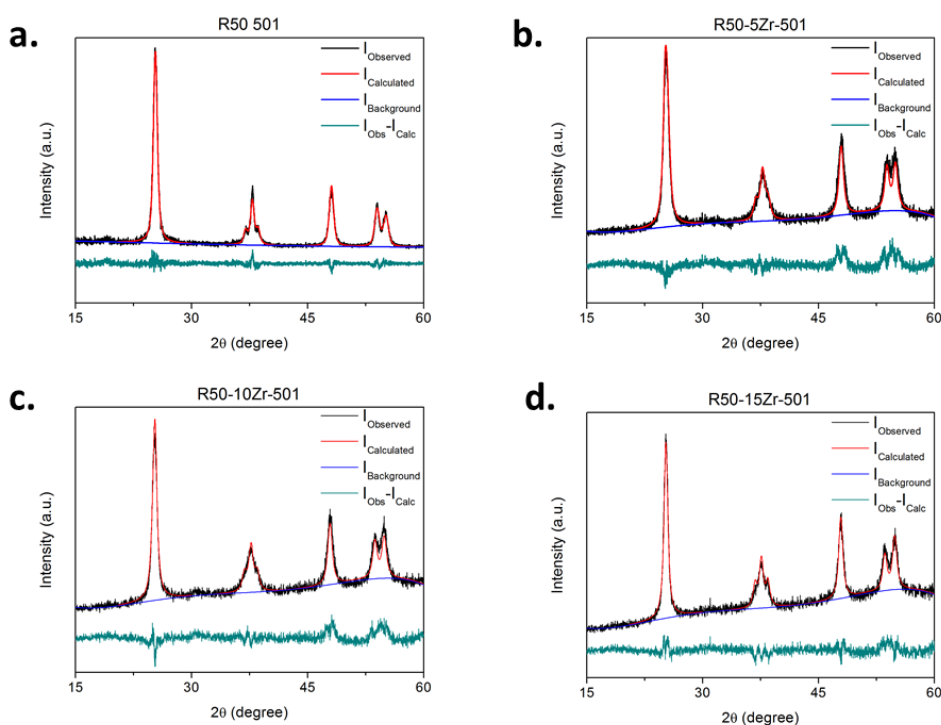


Figure 4.58. Rietveld fittings of **a.** R50 501, **b.** R50-5Zr-501, **c.** R50-10Zr-501, **d.** R50-15Zr-501.

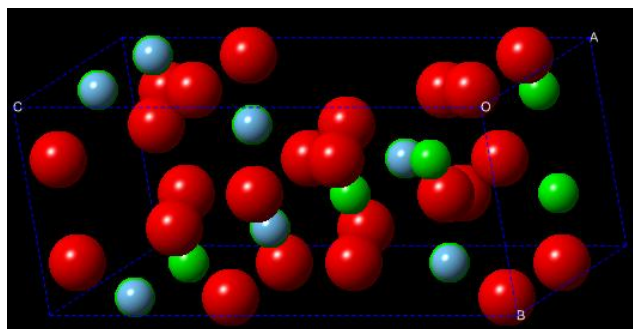


Figure 4.59. Constructed crystal structure of R50-10Zr-501 according to Rietveld refinement results (Blue atoms are titanium, red atoms are oxygen and green atoms are zirconium).

The goal was to have high visible light responsive and high photocatalytic performance under both UV and daylight in TiO_2 powders. Therefore, major requirement of this goal was to have the smallest band gap. Band gap energies of R50-5Zr-501, R50-10Zr-501, and R50-15Zr-501 were 3.15, 3.14, and 3.15 eV, respectively. Moreover, MB degradation percentages of the powders under UV-light exposure were 92.89, 98.46, and 97.05, respectively. Then, according to band gap energies and UV-light MB degradation performances, the optimum Zr doping content was found to be 10wt% for co-doping purpose. In the following parts of the characterization, 5wt% Zr and 15wt% Zr doped powders will not be evaluated.

B and Zr co-doped TiO_2 powders in as-dried and 301 calcination condition form showed no crystallinity as seen in Figure 4.60. Therefore, Rietveld refinement was not conducted for them. Yet, before Rietveld Refinement was conducted for 501 series R50 powders, B doped, Zr doped and co-doped powders in as-dried, and 301 forms were compared with each other for understanding the effect of doping agents on crystallization. 3wt% B doped R50 powder showed high crystallinity in as-dried form; however, at co-doped powder no crystallinity was observed in as-dried form. 10wt% Zr doped powders of R50 composition showed partial crystallization after calcination at 300°C for 1 h, while co-doped

powders of R50 calcined in 301 form showed no crystallinity at all. Therefore, it has been concluded that Zr atoms decrease mobility and crystallization affinity of the powders more than B atoms, due to its larger ionic radii (see Table 2.2). Yet, when B and Zr come together, crystallization amount is decreased even more for same calcination conditions with respect to undoped and doped R50 powders.

X-ray diffractograms of the B and Zr co-doped TiO₂ powders, which were calcined at 500°C, revealed that all of the powders completed crystallization. The crystals were composed of only anatase phase as seen in Figure 4.60. The phase was characterized by the characteristic anatase peak of (101) plane at 2θ of ~25.3° (JCPDS #21-1272). No brookite, rutile, B₂O₃, TiB₂, ZrO₂ or no other phase formation was observed. Upon calcination at 500°C crystallization of the powders are completed and crystallite sizes got smaller with respect to undoped and B or Zr doped R50 powders in 501 condition. Shifting of the peak positions to left side was observed, which was the result of lattice parameter increment. Lattice expansion was attributed to the entrance of Zr⁺⁴ ions to TiO₂ structure by substituting Ti⁺⁴ ions.

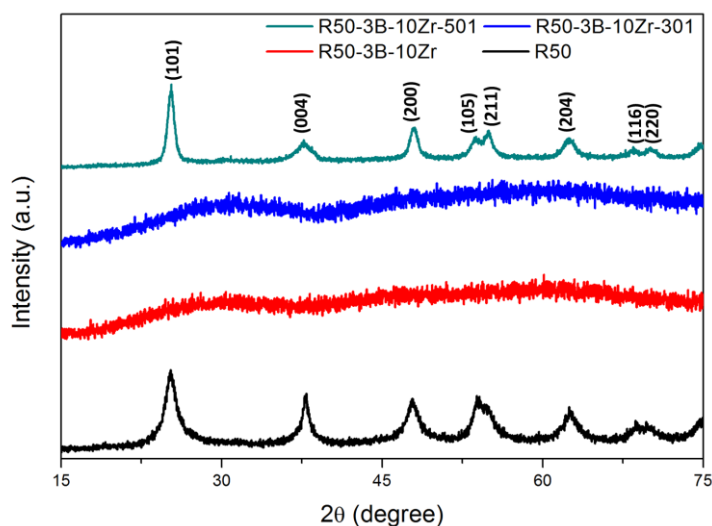


Figure 4.60. XRD patterns of R50 at undoped and co-doped case for as-dried, 301 and 501 calcination conditions.

B and Zr co-doped R50 powders showed complete crystallization, upon calcination at 500°C for 1h. Their Rietveld refinement results of co-doped powders in 501 form were given with R50 501 in Figure 4.61 and listed in Table 4.19, to see the effect of co-doping on crystal structure. The crystal structure of R50-3B-10Zr-501 was constructed in Figure 4.62 with the results obtained after Rietveld refinement.

Table 4.19. Rietveld refinement results of undoped and B and Zr co-doped TiO₂ powders in 501 condition.

Sample	R50 501	R50-3B-10Zr-501
χ^2	0.0965	0.1244
Rp	0.0921	0.0633
wRp	0.1200	0.0818
a=b (Å)	3.78	3.79
c= (Å)	9.51	9.55
Vol (Å ³)	135.88	137.18
Atomic Positions (x, y, z)	Ti	(0.0000, 0.7500, 0.1250)
	O	(0.0000, 0.7500, 0.3333)
	B	(-, -, -)
	Zr	(-, -, -)
Crystallite Size (nm)	16.4	13.2

General remarks and outcomes from the analyses of R50 501 and R50-3B-10Zr-501 TiO₂ powders are as follows:

- χ^2 increased upon co-doping with respect to R50 501 powder. Rp and wRp values, on the other hand, decreased upon co-doping of the powders.
- Lattice parameters increased upon B and Zr co-doping of R50 powders, especially in 'c' direction. Similar results were published by Kapusuz, et al., 2013 and Tokmakci, et al., 2013 for B and Zr co-doped TiO₂ powders.
- Lattice expansions suggested that doping was done successfully. Moreover, Rietveld refinement results revealed the atomic positions of Zr⁺⁴ ions were in (0, 0.75, 0.125) position, which was the position of Ti⁺⁴ ions. In other words, Zr⁺⁴ ions entered lattice by substituting the Ti⁺⁴ ions in co-doping, as reported by Lukac, et al., 2007. B atoms of R50-3B-10Zr-501 occupied (0, 0.75, 0.52) position, which indicated interstitial entrance of B atoms, as suggested by Rehman, et al., 2009.
- Comparing undoped powders with co-doped powders for as-dried, and 301 calcination conditions, it has been recognized that with addition of doping elements, crystallization amount decreases (which is not good, for low temperature synthesis of TiO₂ photocatalysts). However, comparison of the 501 calcination condition results of the undoped and co-doped powders revealed that doping agents decrease growth amount of crystals (which is good, since it enables having higher specific surface area than in undoped 501 powders), as reported by Zaleska, et al., 2008; Teh and Mohamed, 2011; Binitha, et al., 2010. Crystallite size was decreased in R50-3B-10Zr-501 powder with respect to R50 501, R50-3B-501, and R50-10Zr-501.
- Atomic positions of co-doped powders were similar with the one refined for doped. Lattice parameters increased slightly from doped to co-doped powders. This increment was attributed to the entrance of

two different ions to the system. On the other hand, crystallite sizes decreased from doped to co-doped powders. As a result of both B and Zr having inhibition effect over crystal growth (Stengl, et al., 2009; Lukac, et al., 2007)

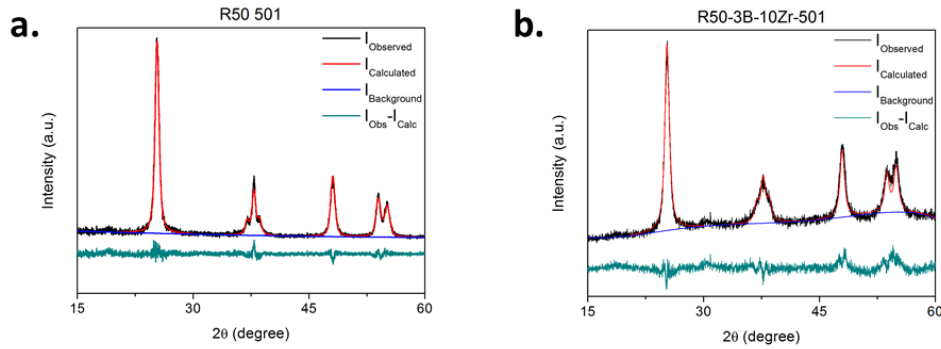


Figure 4.61. Rietveld fittings of **a.** R50 501, **b.** R50-3B-10Zr-501.

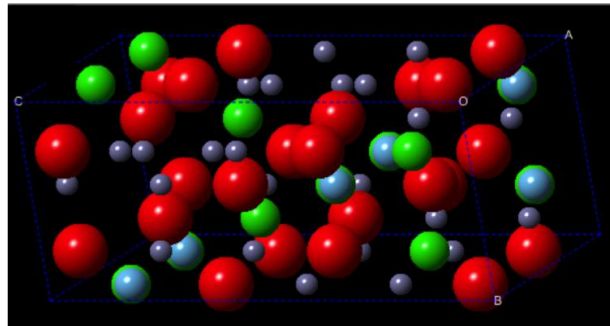


Figure 4.62. Constructed crystal structures of R50-3B-10Zr-501 according to Rietveld refinement results (Blue atoms are titanium, red atoms are oxygen, grey atoms are boron, and green atoms are zirconium).

4.7.4. Scanning Electron Microscopy (SEM)

Surface morphologies of all of the doped and co-doped powders were investigated using SEM. SEM analyses revealed that all powders were composed

of spherical particles smaller than 40 nm in size. Particle size could not be measured accurately from the SEM images due to agglomeration, focusing difficulties at high magnifications, and astigmatism correction problems. Moreover, the irregular shapes of agglomerates caused level differences in the powders being examined. However, unlike undoped powders' agglomerates, as given in Figure 4.63, agglomerates of doped and co-doped powders were highly porous as given in Figures 4.64-4.66, Gupta and Tripathi, 2011, stated that doped powders generally have higher specific surface area than undoped powders. Change of doping content or calcination regime did not lead to a significant morphological difference at the doped or co-doped powders.

General morphology of the undoped R50 powders did not show much difference with respect to calcination condition as seen in Figure 4.63. Obtained powders were highly agglomerated. Size and shape of the agglomerates were totally irregular and random in distribution while individual particles were nearly spherical in shape and smaller than 40 nm in size.

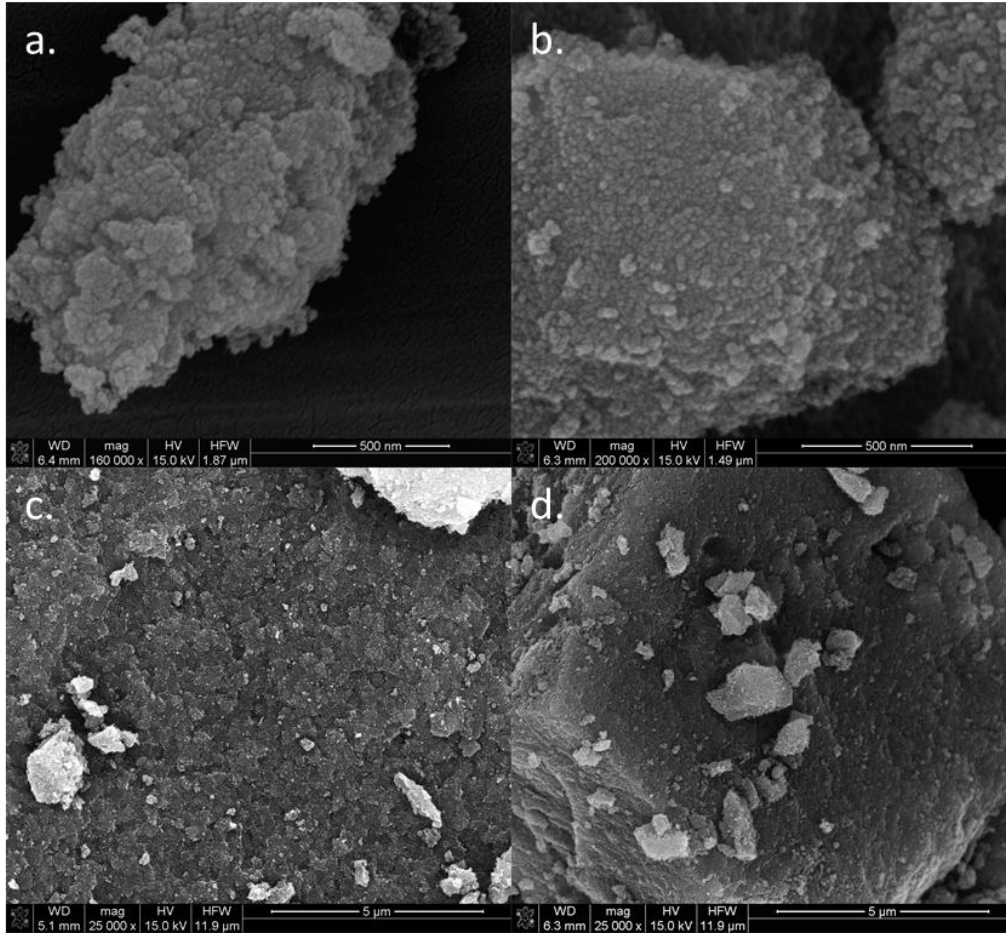


Figure 4.63. SEM images of **a.** R50 As-Dried (160000x), **b.** R50 501 (200000x), **c.** R50 As-Dried (30000x), **d.** R50 501 (25000x) powders.

Interstitial B occupation in TiO_2 crystal has a great importance for having high porosity (Stengl, et al., 2009). General morphology of the B doped powders significantly changed with addition of B dopant as given in Figures 4.63 and 4.64. Also, calcination at 500°C for 1 h was observed to decrease the amount of porosity and sphericity of the powders. The most important change upon B doping was observed at the shape of agglomerates. The agglomerates were non-porous in undoped powders. On the contrary, introduction of the doping agents made agglomerates highly porous. Tokmakci et al., 2013 and Stengl et al., 2009, published SEM micrographs for B doped TiO_2 powders that had similar microstructures. Moreover, porous and spherical structures of agglomerates in

as-dried form began to vanish and turn into irregularly shaped agglomerates, with the heat applied during calcination.

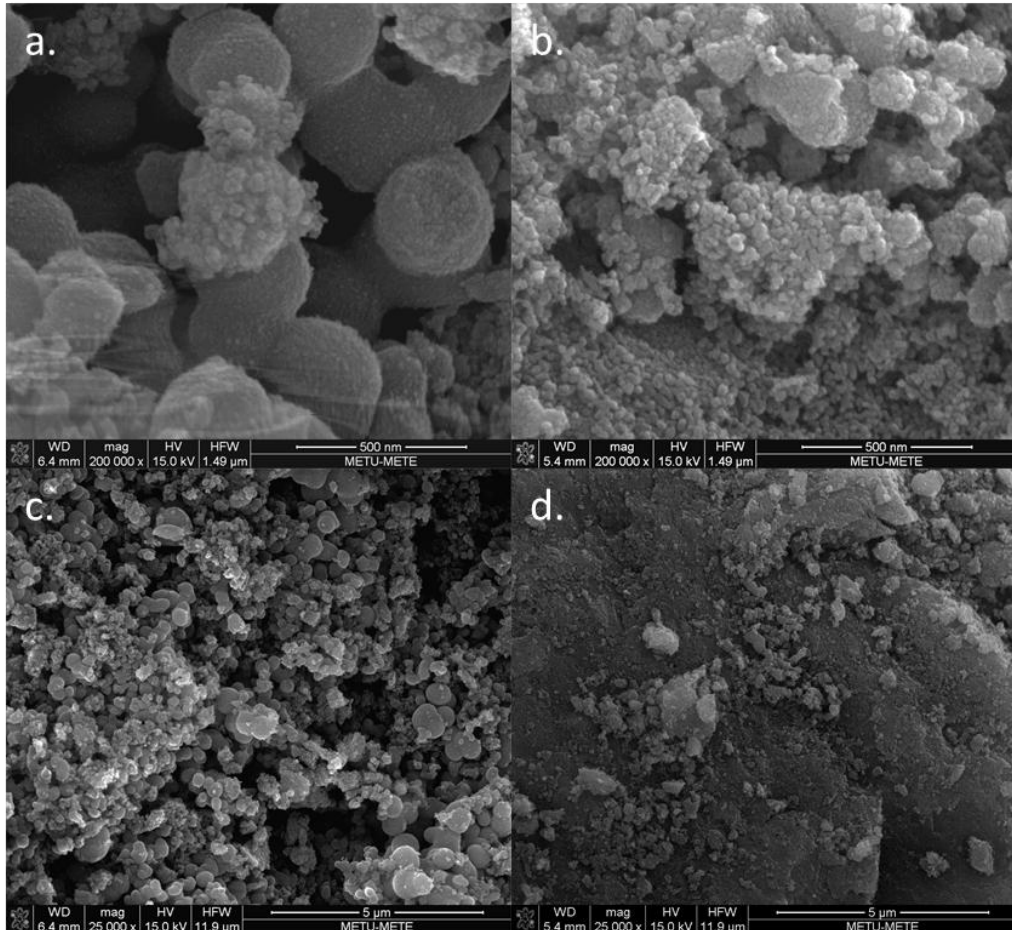


Figure 4.64. SEM images of a. R50-3B (200000x), b. R50-3B-501 (200000x), c. R50-3B (25000x), d. R50-3B-501 (25000x) powders.

General morphology of the Zr doped powders showed significant changes with respect to undoped powders as given in Figures 4.63 and 4.65. Yet, no significant effect of calcination was observed in morphology of powders. The most important change was observed at shape of agglomerates. Non-porous monolithic agglomerates of undoped powders turned into highly porous agglomerates upon Zr doping. Moreover, Binitha, et al., 2010, emphasized the

increasing sphericity of agglomerates in Zr doped powders, and published TEM micrographs of Zr doped TiO_2 powders. Moreover, Lukac et al., 2007, published SEM micrographs of Zr doped TiO_2 powders that had good agreement with the micrographs being presented in Figure 4.65, in terms of both particle size and porosity of agglomerates.

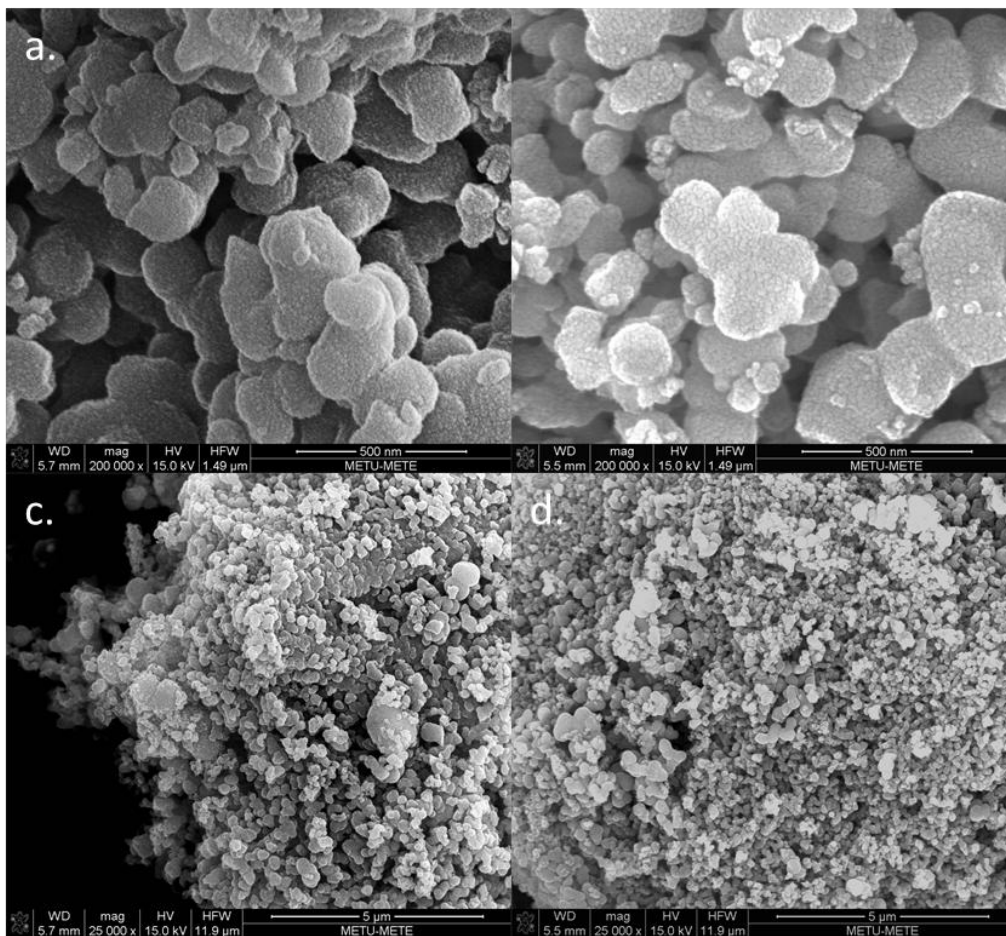


Figure 4.65. SEM images of; **a.** R50-10Zr (200000x), **b.** R50-10Zr-501 (200000x), **c.** R50-10Zr (25000x), **d.** R50-10Zr-501 (25000x) powders.

B and Zr co-doped powders showed important morphological changes with respect to undoped powders as given in Figures 4.63 and 4.66, still significant effect of calcination conditions was not seen at morphology of the co-doped

powders. Observed agglomerates in undoped powders were non-porous and chunky; on the contrary, upon introduction of the doping agents to the system, highly porous agglomerates were formed. Tokmakci et al., 2007, published SEM micrographs for B and Zr co-doped TiO₂ powders that show same kind of agglomerates, which are formed from nanoparticles. Moreover, no morphological changes observed between doped and co-doped powders.

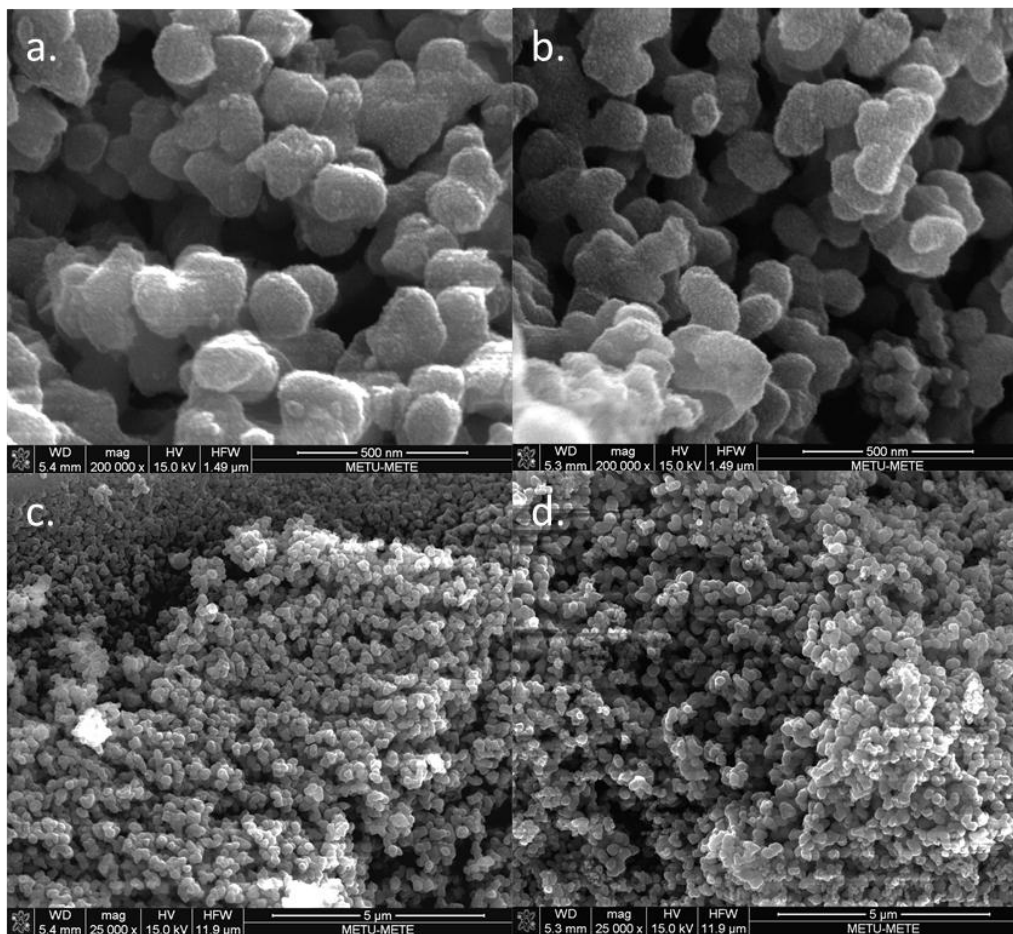


Figure 4.66. SEM images of; a. R50-3B-10Zr (200000x), b. R50-3B-10Zr-501 (200000x), c. R50-3B-10Zr (25000x), d. R50-3B-10Zr-501 (25000x) powders.

Some of the images (Figures 4.64.d, 66.c) at low magnifications (x25000) showed some monolithic agglomerates that have porous agglomerates over.

Whether those monolithic agglomerates are locally occurring agglomerates or not, will be determined from the dark adsorption results of the MB degradation tests. If the general morphology of the agglomerates is composed of monoliths, dark adsorption percentage could not be much high. However, if those monoliths are locally occurring agglomerates and the main morphology was composed of porous agglomerates. It is expected to have high percentages of MB adsorption after 30 minutes of dark stirring of the MB solution.

4.7.5. Diffuse Reflectance Spectroscopy (DRS)

The variation in diffuse reflectance with respect to wavelength for the undoped, 3wt% B doped, 10wt% Zr doped, 3wt% B and 10wt% Zr co-doped R50 powders were shown in Figure 4.67. Reflectance values were very low through UV-light region. From 350 nm to 400 nm region of EM-spectrum reflection values increased rapidly. Then, the reflectance value stayed steady for the remaining part of the visible light region. In other words, after a certain wavelength value between 350 nm and 400 nm, the incoming light was not adsorbed. Since, it cannot activate the TiO₂ powders for photocatalysis reactions to occur. R50 501 and R50-3B-501 powders adsorption edges redshifted with respect to other powders. Band gap energies were calculated from diffuse reflectance spectra of the powders via Kubelka-Munk transformation (Eq. 3.1-3.3.). Band gap energies of the powders were given in Table 4.20 with the corresponding wavelengths of the light, which can activate powders. Corresponding wavelengths revealed that in spite of adsorption edge redshift, all of the powders can respond to violet region of visible light (Table 4.20 and Figure 4.68), which is a small fraction of visible light region of EM-spectrum. Therefore, if all of the powders listed in Table 4.20 were assumed to have same structural and morphological properties, there could not be very significant photocatalytic performance change caused by band gap energy difference. However, the band gap energies revealed that all of the synthesized powders have visible light response.

Table 4.20. Band gap energies of the synthesized undoped, doped and co-doped TiO₂ powders with 501 calcination condition.

Name of The Powder	Energy Band Gap (eV)	Equivalent Wavelength (nm)
R50 501	3.08	~ 402.6
R50-3B-501	3.09	~ 401.3
R50-10Zr-501	3.15	~ 393.7
R50-3B-10Zr-501	3.16	~ 392.4
P25	3.13	~ 396.2

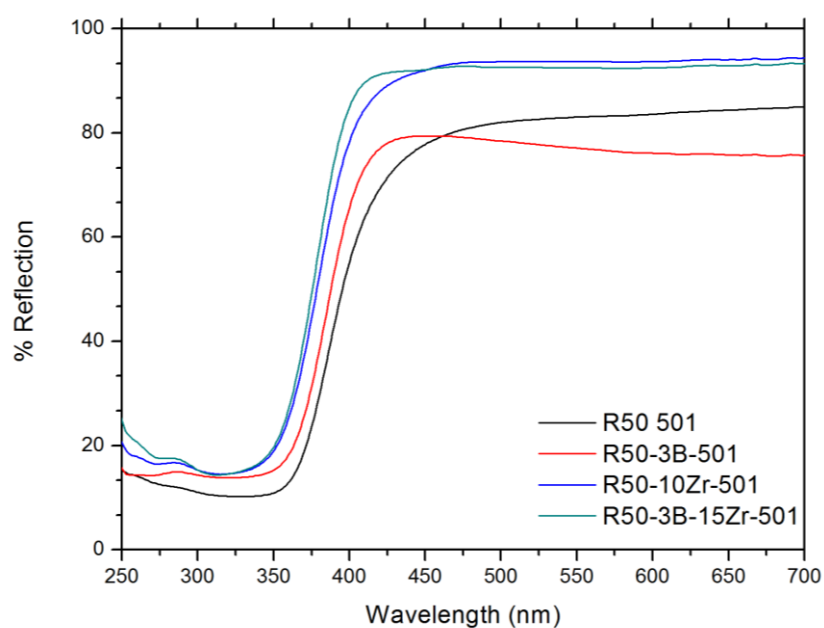


Figure 4.67. Diffuse reflectance spectra of undoped, B-doped, Zr-Doped, B and Zr Co-Doped powders with 501 calcination condition applied.

Some other researchers conducted similar studies with B, Zr or B and Zr atoms. Grabowska, et al., 2008, calculated the band gap of P25 as 3.15 eV, which is in a good agreement with the one listed in Table 4.20. Zaleska, et al., 2008, published

band gap energies for 2wt% and 3wt% B doped TiO₂ powder calcined at 450°C was to be 3.32 and 3.3 eV, respectively. Binitha, et al., 2010, applied 6wt% Zr doping to TiO₂ powders, which were calcined at 250°C and band gap was equal to 3.2 eV. Colmenares, et al., 2006, doped TiO₂ powders with 1wt% Zr, then calcined at 500°C and calculated band gap energy was 3.23 eV. As a result, B or Zr doped or co-doped R50 powders in 501 form had lower band gap energy than the ones given in literature.

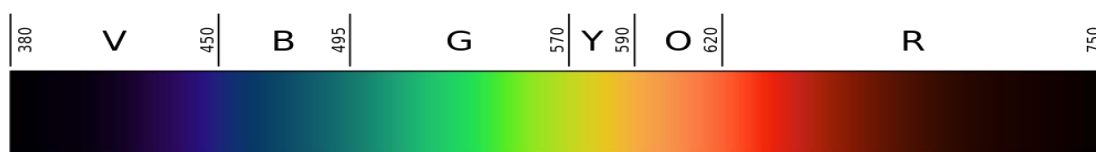


Figure.4.68. Visible light range of electromagnetic spectrum (Wikipedia, 2014).

Other than the band gap energies given in literature, P25 was taken as a reference point for the band gap values of the powders. It is obvious that 2 of the total 4 powders, listed in Table 4.20, have lower band gap than P25, none of them have almost the same band gap energy with P25, and 2 of them have higher band gap than P25.

4.8. Photocatalytic Activity

4.8.1. Methylene Blue Degradation

Photocatalytic activity measurements were conducted in two steps for undoped, doped and co-doped powders. UV light test was performed as explained in Section 3.3. Then, according to percent MB degradation values and rate constant values, performances of the powders were evaluated. Then, one of the undoped (R50 501), and three of the doped (R50-3B-501, R50-10Zr-501, R50-3B-10Zr-

501) powders, which showed high MB degradation under UV-light with lowest band gap energies and were put into daylight test (see Section 3.3.) for 24 h.

Degradation of MB solution with time in dark, UV-light and daylight for the chosen powders are given in Tables 4.21-4.23. It is for sure that each and every one of the powders are photocatalytically highly active. Moreover, according to their MB degradation percentages under UV and daylight as well as in the dark, imply that the synthesized doped TiO₂ powders have high amount of adsorbability of MB (Nguyen-Phan, et al., 2011). Porous structure of the doped powders lead to large specific surface area and cause to have higher density of OH⁻ radicals. As a result, adsorbability of powders increases drastically (Rouquerol, et al., 2014; Liu et al., 2012). Adsorption of MB molecule on a (001) surface of TiO₂ is represented in Figure 4.69. MB molecules adhere to the OH⁻ radicals at the surface of TiO₂ molecule, which leads to the significant increase in the adsorption taking place at the surface of the TiO₂ photocatalyst in dark stirring stage of MB degradation test.

Adsorbent kinetics depends on two parameters, pore size of the adsorbent and the dimensions of diffusing adsorbate molecule (Nguyen, et al., 2012). MB molecules have approximately 0.42 nm³ volume (Pham and Brindley, 1970) and average pore diameter of TiO₂ powders can be about a few nm (5-10 nm). At this conditions TiO₂ molecules can trap lots of MB molecules within the pores easily. SEM images of the doped powders (Figure 4.64-4.66) consist of many nanosized pores, which explained the high percentage of dark adsorption observed at the doped powders. Tokmakci et al., 2013, published even higher MB adsorption values in dark obtained with ball-milled TiO₂ powders. Moreover, the monolithic agglomerates observed at SEM images of some powders (see Figure 4.64.d, 66.c) were locally occurred agglomerates. Then, dominant agglomerates have to be porous type of agglomerates. Otherwise, the adsorption values measured for doped and co-doped powders at dark cannot be as high as listed in Table 4.21.

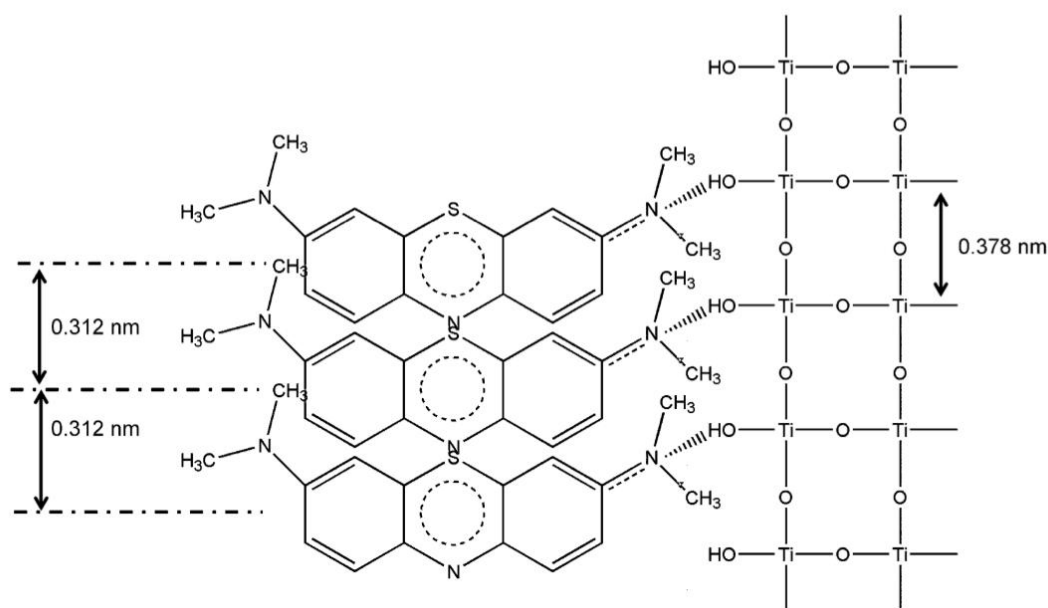


Figure 4.69. Adsorption of MB molecule in a (001) surface of TiO₂ crystal (Liu, et al., 2012).

Table 4.21. Physical adsorption percentages of R50 calcined at 501 under undoped, doped and co-doped conditions.

Powder	% Adsorption
R50 501	1.44
R50-3B-501	59.51
R50-10Zr-501	52.16
R50-3B-10Zr-501	10.58
P25	1.92

Photocatalytic activation mechanism of B doped TiO₂ powder is schematically illustrated in Figure 4.70. Photogenerated electrons move from valance band (VB) to conduction band (CB) at process I. In process II, electrons can be excited to CB of TiO₂ from B1s energy level, which decreases the energy required for photocatalysis reactions to occur (Rehman, et al., 2009).

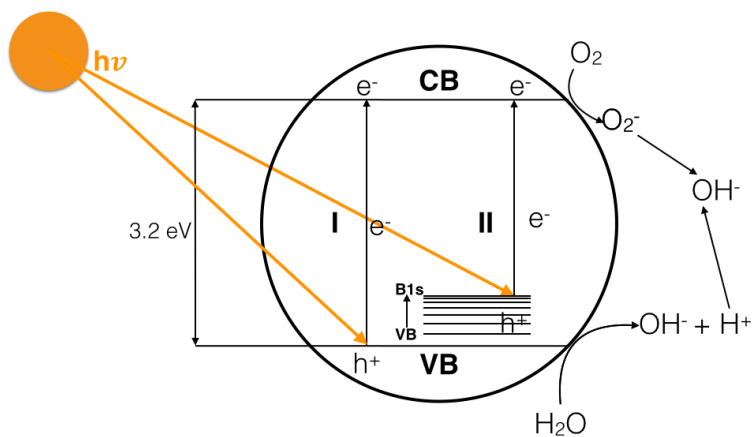


Figure 4.70. Schematic illustration of B doped TiO_2 powder's photocatalysis mechanism.

Photocatalytic activation mechanism of Zr doped TiO_2 powder was schematically illustrated in Figure 4.71. Process I is basic photocatalytic activation of undoped TiO_2 . Zr introduction to the lattice adds 'd' levels of Zr metal in the band gap of TiO_2 that decreases the band gap in Process III (Patil, 2008). Electrons are excited from VB of TiO_2 to Zr energy level, which increases the photogenerated charge particle separation (Hoffmann, et al., 1995). Photogenerated electrons can reduce Zr^{+4} to Zr^{+3} , it may react with adsorbed O_2 molecule to form O_2^- . That may react with electrons and reduce harmful products as seen in Eq. 4.7, 4.8 (Tokmakci, 2013).

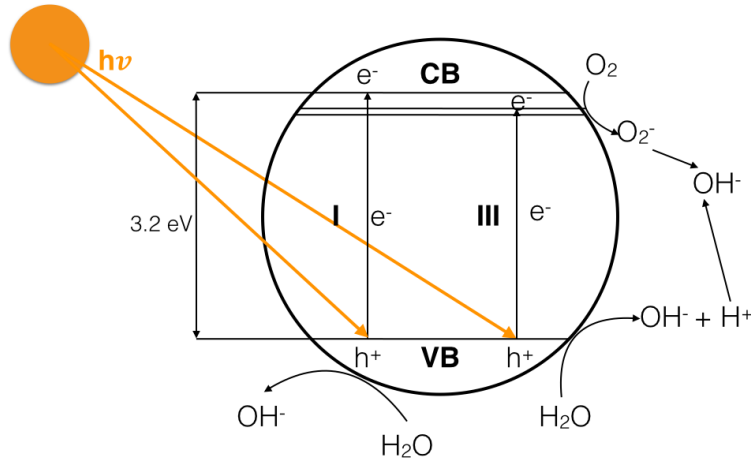


Figure 4.71. Schematic illustration of Zr doped TiO_2 powder's photocatalysis mechanism.

Photocatalytic activation mechanism of B and Zr co-doped TiO_2 powder was schematically illustrated in Figure 4.72. Processes I, II, III are same as explained previously. Moreover, another mechanism at which e^- 's from B1s excited to CB of Zr energy level can be observed. Similar activation reactions occur as given in Eq. 4.6-4.8. Further MB degradation mechanism discussion was done in detail in Section 2.2.

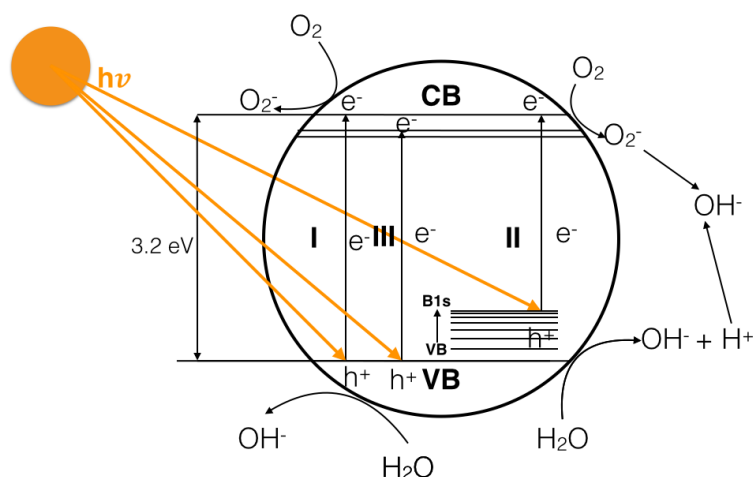


Figure 4.72. Schematic illustration of B and Zr co-doped TiO₂ powder's photocatalysis mechanism.

MB degradation percentage of doped and co-doped R50 powders under UV-light illumination enhanced with respect to R50 501 powders, except for R50-3B-501 powder. B doped powder revealed a little bit lower photocatalytic performance under UV-light illumination than R50 501. Zaleska, et al., 2008 published even more decrease at photocatalytic performance at B doped powder with respect to undoped powder. Photocatalytic degradation amount of MB under UV-light illumination was ~4% improved by 10wt% Zr doping with respect to R50 501. Binitha, et al., 2010 attributed this kind of photocatalytic performance improvements to changes occurring in structural and morphological properties. Highest improvement under UV-light illumination was achieved at co-doped powders as ~5%. Tokmakci, et al., 2013 explained this further improvement as synergistic effects of B and Zr co-doping. Photocatalytic degradation results of doped and co-doped R50 powders were given with undoped R50 and P25 powder in Figure 4.73 and Table 4.22.

It was obvious that the powders composed of different doping contents, were highly active under UV-light illumination in photocatalytic MB degradation reactions. The employed light source sent photons with energy of 3.39 eV. This means all of the synthesized powders, were activated easily by the sent photons.

Since, no significant variation was observed between the morphologies of B doped, Zr doped and co-doped powders (i.e. particle size, shape, porosity, etc.). As a result, no major effect of morphology on the photocatalytic performances was expected between doped and co-doped powders.

However, crystallinity, phase assembly, atomic positions and crystallite sizes have the upmost importance for photocatalytic performance of the doped powders under UV-light illumination. All of the given parameters were similar for all powders except crystallite size. Smallest crystallite size was observed in co-doped R50 powder in 501 condition, as supported by photocatalytic performance.

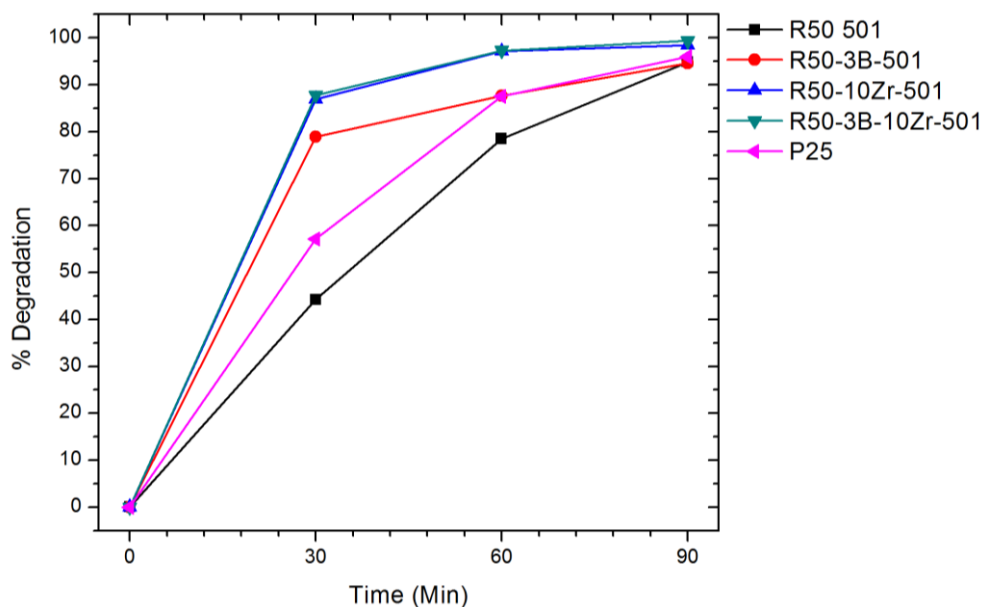


Figure 4.73. Methylene blue degradation graph of the undoped, doped and co-doped powders with composition for powders of R50 that are calcined at 500°C for 1 h, UV-light illumination for 90 min.

For all doping conditions results were more or less in good agreement with each other. Zr doped powders had higher photocatalytic performance than B doped powders. B and Zr co-doped powders showed synergistic effects. As a result, further photocatalytic performance improvements were observed.

P25 was set as lower limit of success for the doped and co-doped powders, as set for the undoped powders. 3wt% B and 10wt% Zr co-doped and 10wt% Zr-doped powders showed higher MB degradation, while undoped and 3wt% B doped powders revealed lower MB degradation than P25 under UV-light exposure.

Table 4.22. % Degradation values of the powders under UV-light illumination.

Powder	% Degradation Upon UV-light Illumination		
	30 Min	60 Min	90 Min
R50 501	44.21	78.48	94.83
R50-3B-501	78.86	87.67	94.57
R50-10Zr-501	86.95	97.16	98.46
R50-3B-10Zr-501	87.80	97.32	99.38
P25	57.18	87.51	96.00

Photocatalytic performances of these powders were, also, tested by MB degradation under daylight illumination for 24 h. Photocatalytic measurement was done at the end of 24 h as described in Section 3.3. Test was conducted under daylight; no artificial light source was occupied. Test interval covers both day and night. P25 was tested under daylight exposure for setting the lower limit of success for undoped, doped and co-doped powders under daylight illumination.

MB degradation amount of doped and co-doped R50 powders increased under daylight illumination with respect to undoped form. First of all, both doped and

co-doped powders showed improvement between 22 to 24% MB degradation under daylight illumination with respect to R50 501, as listed in Table 4.23. Unlike, MB degradation performance under UV-light exposure, B doped powders showed significant photocatalytic performance improvement under daylight exposure with respect to R50 501. Zaleska, et al., 2009, published high increase at visible light photocatalytic performance at 2wt% B doped TiO₂ powder. However, best performance was achieved at B and Zr co-doped powders as in the UV-light results. According to obtained results, Zr doping was found to be more effective than B doping under daylight illumination. Lastly, all of the doped and co-doped powders showed higher MB degradation percentages than P25 powder under daylight MB degradation test, which means highest goal (which was to have high visible light photocatalytic performance) was successfully achieved.

It is for sure that powders with different doping content, having high visible light photocatalytic performance, were synthesized successfully.

Table 4.23. % Degradation values of powders under daylight illumination.

Powders	% Degradation
R50 501	75.26
R50-3B-501	97.31
R50-10Zr-501	98.50
R50-3B-10Zr-501	99.15
P25	95.36

Consequently, B and Zr co-doped powders showed the best MB degradation performance under both UV and daylight exposure for R50 powders. High performance of B and Zr co-doped powders was caused by the synergistic effects of the decreased crystallite size and ‘O’ vacancy formed by B doping decreasing the recombination rate by forming electron traps and by leading h⁺s to the surface. The lattice expansion caused by Zr doping and the formed defects

prevent e^-/h^+ recombination that increases the rate constant of the co-doped powders (Kapusuz, et al., 2013; Rehman, et al., 2009; Lukac, et al., 2007; Tokmakci, et al., 2013).

4.8.2. Apparent Rate Constant

Rate constant versus UV-light illumination time graph was given in Figure 4.74. Rate constant of P25 was also calculated and indicated in the graph. Neither undoped nor B doped powders showed higher rate constants than P25 under UV-light exposure. Zr doped powders' rate constants were just above the rate constant of P25. Yet, B and Zr co-doping resulted with a drastic enhancement at rate constant values of the powders. R50-10Zr-501, and R50-3B-10Zr-501 were classified as “successful” in terms of the photocatalytical performance under UV-light exposure.

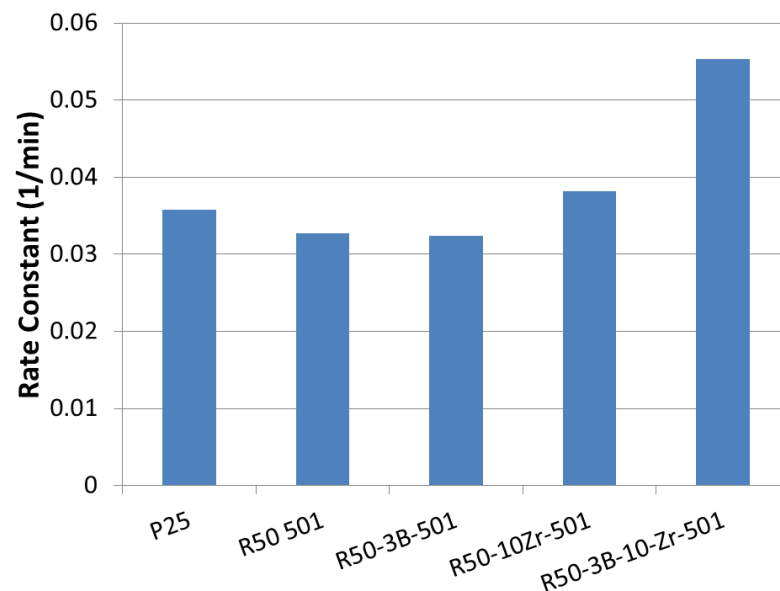


Figure 4.74. Rate constant values of R50 in undoped, doped and co-doped conditions, calcined at 500° C for 1 h, after 90 min UV-light illumination.

Rate constant versus daylight illumination time graph was given in Figure 4.75. Rate constant of P25 was also calculated and indicated in the graph. Undoped powders showed lower rate constant than P25. However, rate constants of B doped, Zr doped, B and Zr co-doped powders were significantly above the rate constant of P25. R50-3B-501, R50-10Zr-501, and R50-3B-10Zr-501 were classified as “successful” in terms of the photocatalytical performance under daylight exposure.

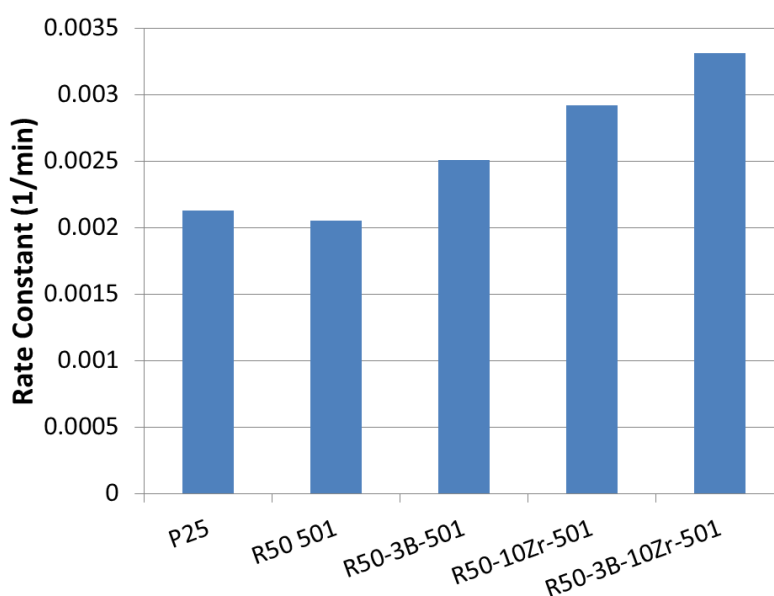


Figure 4.75. Rate constant values of R10 and R50 at undoped, doped and co-doped conditions, calcined at 500° C for 1 hour, after 24 h’s of daylight test.

Low daylight rate constants, with respect to UV-light rate constants, were the main reason why photocatalytic performance improvement was needed. Doping was occupied for improvement of photocatalytic performances and it worked well for both UV-light and daylight exposure. Figure 4.76 shows the improvement achieved by doping at rate constants with respect to undoped R50 501 and P25 powders. Both UV and daylight photocatalytic performances were improved by doping. Yet, according to the k_{ap}^{vis}/k_{ap}^{UV} ratio, as listed in Table

4.24, daylight performances were improved much more than UV-light performances, upon doping or co-doping of the powders.

Table 4.24. Daylight rate constant/UV-light rate constant values of undoped, doped and co-doped, R10 and R50 powders, calcined at 500°C for 1h.

Powder	k_{ap}^{vis}/k_{ap}^{UV}
R50 501	0.030
R50-3B-501	0.077
R50-10Zr-501	0.074
R50-3B-10Zr-501	0.059

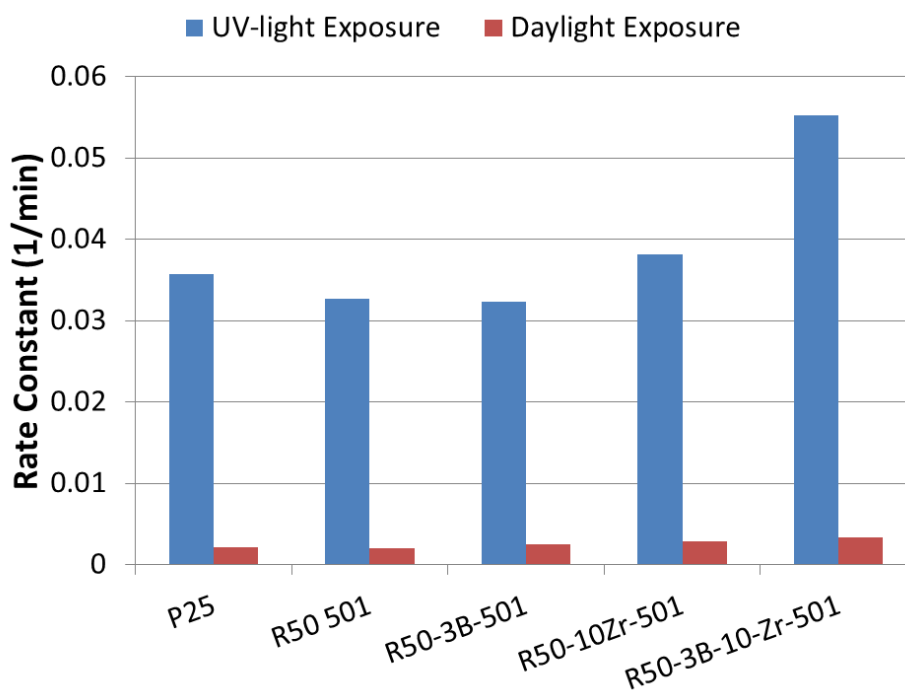


Figure 4.76. Rate constant value comparison of R10 and R50 at undoped, doped and co-doped conditions, calcined at 500°C for 1 hour, after 90 minutes of UV-light and 24 h's of daylight illumination test.

Conclusively, in the first part of the thesis, it has been proved that only by changing water content of the mother solution and calcination conditions, daylight active TiO₂ powders were synthesized. However, undoped powders had low daylight photocatalytic performance with respect to UV-light performance. Therefore, the next goal was to increase the photocatalytic performance of the powders under daylight via doping or co-doping. It has been found that doping amount and type of agent directly affected the lattice parameters, and the crystallite sizes. Doping caused a drastic change in powder morphology from monolithic agglomerates to porous agglomerates too. However, band gap energy values did not show much fluctuation via doping. They were all in visible light region of EM-spectrum. Photocatalytic performances of R50 501 powders were very high under UV-light exposure. Therefore, doping and co-doping showed slight improvement under UV-light. However, daylight performances were enhanced ~22% for R50-3B-501, ~23% for R50-10Zr-501, and ~24% for R50-3B-10Zr-501 powders only by doping with B or Zr or by co-doping them together.

To determine the best conditions for the synthesis of the powders to be used in photocatalytic applications, two requirements were set, according to the explanations given in Section 4.5:

- Higher MB degradation percentage than P25 under both UV and daylight exposure,
- Having the smallest crystallite size.

4.9. Determination Of Best Water Content And Doping Content

In order to, determine the best calcination condition and doping content, characteristics of P25 were taken as reference. Upon, analysis of the structural properties of the doped and co-doped powders, best calcination condition was found to be 500°C for 1 h. Best B and Zr doping percentages were determined, according to the band gap energies and photocatalytic performance under UV-

light of the powders in 501 form. After evaluation of the band gap energies and photocatalytic performances, 3wt% for B and 10wt% for Zr were found to have the lowest band gap energies among all of the B or Zr doped TiO₂ powders.

Upmost goal of the study was to synthesize TiO₂ powders with high visible light photocatalytic performance. All of the four powders were visible light active. Moreover, high daylight photocatalytic performances were achieved at doped and co-doped powders. Also, their band gap energies were very close to each other. Therefore, no elimination based on band gap energy values could be performed.

According to MB degradation values under daylight and UV-light exposure. Firstly, R50 501 powder was eliminated due to its lower daylight performance than P25. Then, due to having lower UV-light performance than P25, R50-3B-501 was eliminated. Then, two of the four of undoped, doped and co-doped TiO₂ powders namely; R50-10Zr-501, and R50-3B-10Zr-501 were selected because they exhibited relatively high MB degradation than P25 powder under both UV and daylight exposure.

Final requirement was to have the smallest crystallite size. Both of the selected powders were composed of anatase phase and they had relatively low and very close crystallite size. As told previously, specific surface area has severe importance for photocatalytic applications. In other words, having smaller crystallite size means having better photocatalytic performance (Ramaswamy, et al., 2008; Xu, et al., 1999). Therefore, as listed in Tables 4.17 and 4.18; smallest crystallite size was achieved at R50-3B-10Zr-501.

Conclusively, powder with R ratio of 50 that was 3wt% B and 10wt% Zr co-doped and calcined at 500°C for 1 h was found to be the best candidate for photocatalytic applications.

CHAPTER 5

CONCLUSIONS

This thesis study composed of two main parts. In the first part the effects of water content of the initial solution and calcination regime (time and temperature) on the formation, structure, morphology, and photocatalytic properties of sol-gel derived TiO₂ powders were researched. Various mole of water/mole of Ti precursor ratios (R ratio) and calcination temperatures and durations were employed to determine the best R ratio for doping and co-doping purposes. The following conclusions were attained.

1. Visible light active TiO₂ powders could be synthesized by sol-gel process.
2. Water content of the initial solution affected the powder formation and percent crystallinity developed in as-dried powders. The powders with R ratio smaller than or equal to 10 were synthesized by alkoxide sol-gel via gelation. Upon increasing the R ratio to 30 and 50, powders were synthesized by alkoxide sol-gel via precipitation.
3. XRD analysis revealed that structural properties such as; degree of crystallinity in as-dried powders, present phases, assembly of the phases, and crystallite size of powders were affected by changing the R ratio and calcination regime. In general, increasing water content led to a decrease in the crystallite size for a given calcination regime.
4. No significant effects of water amount or calcination regimes were observed on particle size and morphology of the powders.

5. Band gap energy of the powders was affected by the R ratio and calcination regime. However no mathematical relationship was observed between band gap energy and water content or calcination regimes.
6. Better Methylene Blue (MB) degradation could be achieved with increasing R ratio. Some of the powders synthesized had better MB degradation percentage than commercially available well known P25 powder after 90 minutes of UV-light illumination. Visible light photocatalytic activity was observed in daylight. However, the powders were not able to pass MB degradation value of P25 in daylight illumination.

In the second part of the study, boron (B) doped, zirconium (Zr) doped, and B and Zr co-doped TiO₂ powders were synthesized by sol-gel process. The effects of calcination temperature and type and amount of doping agent on structural, morphological, and photocatalytic properties were examined for the doped and co-doped TiO₂ powders. The conclusions withdrawn from this part of the study are listed below:

1. B and Zr doping inhibited crystallization of the powders. The Zr doped, B doped, and B and Zr co-doped powders showed no crystallinity in as-dried form. Total crystallization in all of the doped and co-doped powders was achieved after calcination at 500°C for 1 h.
2. B ions entered the lattice of TiO₂ interstitially and lead to shrinkage in lattice whereas, Zr ions entered the lattice by substituting the Ti ions causing an expansion in the lattice due to its larger radius than Ti. Largest lattice expansion was observed in co-doped powders.
3. Crystallite size decreased with increasing doping amount for both B and Zr doping. However, upon co-doping a drastic decrease was observed with respect to undoped powders calcined at the same conditions.
4. Doping caused some changes in morphology of the powders. Agglomerates became much more spherical and highly porous.

5. Although, band gap energy of the doped and co-doped TiO₂ powders did not change much as compared to undoped TiO₂ powders, all of the doped and co-doped powders were visible light active.
6. Photocatalytic properties improved by doping and co-doping in UV-light and daylight illumination with respect to undoped powders. Zr doping influenced photocatalytic performance of TiO₂ powders more than B doping. Though, B and Zr co-doping further improved the photocatalytic performance in both UV and daylight illumination as compared to single doping of each dopants. Zr doped, B and Zr co-doped TiO₂ powders showed better MB degradation than P25 powder in both UV and daylight illumination.

All in all, it has been proved that TiO₂ powders with enhanced daylight photocatalytic activity could be synthesized successfully by sol-gel process when an appropriate mole of water/mole of Ti precursor ratio, calcination regime, and doping is applied.

REFERENCES

- Akpan, U., and Hameed, B. (2010). The advancements in sol-gel method of doped-TiO₂ photocatalysts. *Applied Catalysis A: General*, 375, 1-11.
- Asbury, J. B., Hao, E., Wang, Y., Ghosh, H. N., and Lian, T. (2001). Ultrafast electron transfer dynamics from molecular adsorbates to semiconductor nanocrystalline thin films. *Journal of Physical Chemistry B*, 105, 4545-4547.
- Aysin, B., Ozturk, A., and Park, J. (2013). Silver-loaded TiO₂ powders prepared through mechanical ball milling. *Ceramics International*, 39, 7119-7126.
- Bahnemann, D. W., Kormann, C., and Hoffmann, M. R. (1987). Preparation and characterization of quantum size zinc oxide: A detailed spectroscopic study. *Journal of Physical Chemistry*, 91, 3789-3798.
- Bartlett, J. R., Woolfrey, J. L., and Buykx, W. J. (1990). Effects of solvent concentration and the method of catalysis on the preparation and properties of Synroc powders. *Proceedings of the 3rd International Conference on Powder Processing Science* (pp. 191-196). San Diego: MRS Symp Proc.
- Bian, L., Song, M., Zhou, T., Zhao, X., and Dai, Q. (2009). Band gap calculation and photo catalytic activity of rare earths doped rutile TiO₂. *Journal of Rare Earths*, 27, 461-468.

- Binitha, N. N., Yaakob, Z., and Resmi, R. (2010). Influence of synthesis methods on zirconium doped titania photocatalysts. *Central European Journal of Chemistry*, 8, 182-187.
- Busch, R., Bakke, E., and Johnson, W. L. (1998). Viscosity of the supercooled liquid and relaxation at the glass transition of the $Zr_{46.75}Ti_{8.25}Cu_{7.5}Ni_{10}Be_{27.5}$ bulk metallic glass forming alloy. *Acta materials*, 46, 4725-4732.
- Byrappa, K., and Adschiri, T. (2007). Hydrothermal technology for nanotechnology. *Progress in Crystal Growth and Characterization of Materials*, 53, 117-166.
- Cандero, B., Gomez, V., Platero-Pratz, A. E., Reves, M., Echevirria, J., Cremades, E., et al. (2008). Covalent radii revisited. *Dalton Transactions*, 21, 2832-2838.
- Carp, O., Huisman, C. L., and Reller, A. (2004). Photoinduced reactivity of titanium dioxide. *Progress in Solid State Chemistry*, 32 (1-2), 33-117.
- Chatterjee, D., and Dasgupta, S. (2005). Visible light induced photocatalytic degradation of organic pollutants. *Journal of Photochemistry and Photobiology C: Photochemistry Reviews*, 6, 186-205.
- Chen, Y., and Dionysiou, D. D. (2008). Sol-gel synthesis of nanostructured TiO_2 films for water purification. In P. Innocenzi, Y. Zub, and V. Kessler, *Sol-Gel Methods for Materials Processing* (pp. 67-75). Dordrecht: Springer.
- Chen, Z., Zhao, G., Li, H., and Han, G. (2009). Effects of Water Amount and pH on the Crystal Behaviour of a TiO_2 Nanocrystalline Derived from a Sol-Gel Process at a Low Temperature. *Journal of American Ceramic Society*, 92 (5), 1024-1029.

- Clementi, E., Raimond, D. L., and Reinhardt, W. P. (1967). Atomic Screening Constants from SCF Functions. II. Atoms with 37 to 86 Electrons . *Journal of Chemical Physics*, 47 (4), 1300-1307.
- Colmenares, J., Aramendia, M., Marinas, A., Marinas, J., and Urbano, F. (2006). Synthesis, characterization and photocatalytic activity of different metal-doped titania systems. *Applied Catalysis A: General*, 306, 120-127.
- Dejohn, P., and Hutchins, R. (1976). Treatment of Dye Wastes with Granular Activated Carbon. *Journal Textile Chemist and Colorist*, 8 (4), 34-38.
- Diebold, U. (2003). The surface science of titanium dioxide. *Surface Science Reports*, 48, 53-229.
- Dogu, D. (2012). *The photocatalytic activity of praseodymium doped titanium dioxide*. PhD Thesis, Middle East Technical University, Micro and Nanotechnology, Ankara, Turkey
- El Goresy, A., Chen, M., Dubrovinsky, L., Gillet, P., and Graup, G. (2001). An ultradense polymorph of rutile with seven-coordinated titanium from the Ries Crater. *Science*, 293, 1467-1470.
- El Goresy, A., Chen, M., Gillet, P., Dubrovinsky, L., and Graup, G. (2001). A natural shock-induced dense polymorph of rutile α -PbO₂ structure in the suevite from the Ries Crater in Germany. *Earth and Planetary Science Letters*, 192 (4), 485-495.
- Ersoz, I. T. (2009). *Application of semiconductor films over glass/ceramic surfaces and their low temperature photocatalytic activity*. Master's Thesis, Middle East Technical University, Chemical Engineering, Ankara, Turkey.

- Etacheri, V., Seery, M., Hinder, S., and Pillai, S. (2011). Oxygen rich titania: A dopant free, high temperature stable, and visible-light active anatase photocatalyst. *Advanced Functional Materials*, 21, 1-9.
- Fujishima, A., and Honda, K. (1972). Electrochemical photolysis of water at a semiconductor electrode. *Nature*, 238, 37-38.
- Fujishima, A., and Tryk, D. A. (1999). Photoelectrochemical Conversion. In K. Honda, *Functionality of Molecular Systems* (pp. 196-224). Tokyo: Springer.
- Fujishima, A., Rao, T. N., and Tryk, D. A. (2000). Titanium dioxide photocatalysis. *Journal of Photochemistry and Photobiology C: Photochemistry Reviews*, 1, 1-21.
- Fujishima, A., Zhang, X., and Tryk, D. A. (2008). TiO₂ photocatalysis and related surface phenomena. *Surface Science Reports*, 63 (12), 515-582.
- Geng, H., Yin, S., Yang, X., Shuai, Z., and Liu, B. (2006). Geometric and electronic structure of boron-doped photocatalyst TiO₂. *Journal of Physics: Condensed Matter*, 18, 87-96.
- Ghows, N., and Entezari, M. H. (2011). Exceptional catalytic efficiency in mineralization of the reactive textile azo dye (RB5) by a combination of ultrasound and core-shell nanoparticles (CdS/TiO₂). *Journal of Hazardous Materials*, 195, 132-138.
- Gorska, P., Zaleska, A., Kowalska, E., Klimczuk, T., Sobczak, J. W., Skwarek, E., et al. (2008). TiO₂ photoactivity in vis and UV light: The influence of calcination temperature and surface properties. *Applied Catalysis B: Environmental*, 84, 440-447.
- Gouma, P. I., and Mills, M. J. (2001). Anatase-to-rutile transformation in titania powders. *Journal of American Ceramic Society*, 84 (3), 619-622.

- Grabowska, E., Zaleska, A., Sobczak, J. W., Gazda, M., and Hupka, J. (2009). Boron-doped TiO₂: Characteristic and photoactivity under visible light. *Procedia Chemistry*, *1*, 1553-1559.
- Greenwood, N. N., and Earnshaw, A. (1997). *Chemistry of Elements*. Elsevier Science Ltd.
- Guillen-Santiago, A., Mayen, S., Torres-Delgado, G., Castanedo-Perez, R., Maldonado, A., and Olvera, M. (2010). Photocatalytic degradation of methylene blue using undoped and Ag-doped TiO₂ thin films deposited by a sol-gel process: Effect of the ageing time of the starting solution and the film thickness. *Materials Science and Engineering B*, *174*, 84-87.
- Gupta, S. M., and Tripathi, M. (2011). A review of TiO₂ nanoparticles. *Chinese Science Bulletin*, *56*, 1639-1657.
- Hahn, T. (2005). *International Table for Crystallography Volume A: Space-Group Symmetry*. Chester, England: The International Union of Crystallography.
- Hashimoto, K., Irie, H., and Fujishima, A. (2005). TiO₂ photocatalysis: a historical overview and future prospects. *Japanese Journal of Applied Physics*, *44*, 8269-8285.
- Heller, A. (1981). Conversion of sunlight into electric power and photoassisted electrolysis of water in photoelectrochemical cells. *American Chemical Society*, *14* (5), 154-162.
- Hermann, J. (1999). Water treatment by heterogeneous photocatalysis. In F. Jansen, and R. van Santen, *Environmental Catalysis* (pp. 171-194). London: Imperial College.
- Hirano, M., Nakahara, C. H., Ota, K., Tanaike, O., and Inagaki, M. (2003). Photoactivity and phase stability of ZrO₂-doped anatase-type TiO₂ directly formed as nanometer-sized particles by hydrolysis under

hydrothermal conditions. *Journal of Solid State Chemistry*, 170 (1), 39-47.

- Hoffmann, M., Martin, S., Choi, W., and Bahnemann, D. (1995). Environmental applications of semiconductor photocatalysis. *Chemical Reviews*, 95 (1), 69-96.
- Houas, A., Lachheb, H., Ksibi, M., Elaloui, E., Guillard, C., and Herrmann, J.-M. (2001). Photocatalytic degradation pathway of methylene blue in water. *Applied Catalysis B: Environmental*, 31, 145-157.
- Hu, Y., Tsai, H. -L., and Huang, C. -L. (2003). Phase transformation of precipitated TiO₂ nanoparticles. *Materials Science and Engineering A*, 344, 209-214.
- Huang, F., Chen, L., Wang, H., and Yan, Z. (2010). Analysis of the degradation mechanism of methylene blue by atmospheric pressure dielectric barrier discharge plasma. *Chemical Engineering Journal*, 162, 250-256.
- Ichihashi, Y., Yamashita, H., and Anpo, M. (1997). Relationship Between the Local Structures of Titanium Oxide Photocatalysts and their Reactivities - XAFS, UV, Photoluminescence and Photoreaction Investigations. *Supplement au Journal de Physique III d'avril*, 2, 883-885.
- Isley, S. L., and Penn, R. L. (2008). Titanium dioxide nanoparticles: effect of sol-gel pH on phase composition, particle size, and particle growth mechanism. *Society*, 112 (12), 4469-4474.
- Jung, K. Y., Park, S. B., and Anpo, M. (2005). Photoluminescence and photoactivity of titania particles prepared by the sol-gel technique: effect

of calcination temperature. *Journal of photochemistry and photobiology A: Chemistry*, 170, 247-252.

- Kapusuz, D., Park, J., and Ozturk, A. (2011). Preparation and photocatalytic activity of boron or zirconium doped titania. *SET2011, 10th International Conference on Sustainable Energy Technologies*. Istanbul.
- Kapusuz, D., Park, J., and Ozturk, A. (2013). Sol-gel synthesis and photocatalytic activity of B and Zr co-doped TiO₂. *Journal of Physics and Chemistry of Solids*, 74, 1026-1031.
- Kasuga, T., Oyamada, K., Hiramatsu, M., and Hoson, A. (1997). Improvement of photocatalytic property of sol-gel derived TiO₂-SiO₂ powders by chemical treatment. In L. C. Klien, E. J. Pope, S. Sakka, and J. L. Woolfrey, *Sol-Gel Processing of Advanced Materials* (pp. 365-368).
- Kingery, W. D., Bowen, H. K., and Uhlmann, D. R. (1976). *Introduction to Ceramics*. New York: Wiley.
- Kuo, W., and Ho, P. (2001). Solar photocatalytic decolorization of methylene blue in water. *Chemosphere*, 45, 77-83.
- Lakshmi, S., Renganathan, R., and Fujita, S. (1995). Study on TiO₂-mediated photocatalytic degradation of methylene blue. *Journal of Photochemistry and Photobiology A: Chemistry*, 88, 163-167.
- Larson, A. C., and Von Dreele, R. B. (2004). General structure analysis system (GSAS). *The Regents of the University of California*. California, USA.
- Lee, J., and Gouma, P. I. (2012). Sol-gel processed oxide photocatalysts. In M. A. Aegerter, and M. Prassas, *Advances in Sol-Gel Derived Materials and Technologies* (pp. 217-237). New York: Springer.

- Li, Y., White, T. J., and Lim, S. H. (2004). Low-temperature synthesis and microstructural control of titania nano-particles. *Journal of Solid State Chemistry*, 177, 1372-1381.
- Linsebigler, A. L., Lu, G., and Yates Jr., J. T. (1995). Photocatalysis on TiO₂ surfaces: principles, mechanisms, and selected results. *Chemical Reviews*, 95, 735-758.
- Livage, J., Henry, M., and Sanchez, C. (1988). Sol-gel chemistry of transition metal oxides. *Progress in Solid State Chemistry*, 18, 259-341.
- Lukac, J., Klementova, M., Bezdicka, P., Bakardjieva, S., Subrt, J., Szatmary, L., et al. (2007). Influence of Zr as TiO₂ doping ion on photocatalytic degradation of 4-chlorophenol. *Applied Catalysis*, 74, 83-91.
- Maira, A. J., Yeung, K. L., Soria, J., Coronado, J. M., Belver, C., and Lee, C. Y. (2001). Gas-phase photo-oxidation of toluene using nanometer-size TiO₂ catalysts. *Applied Catalysis B Environmental*, 29 (4), 327-336.
- Maldotti, A., Molinari, A., and Amadelli, R. (2003). Photocatalysis with organized systems for the oxofunctionalization of hydrocarbons by O₂. *ChemInform*, 102 (10).
- Manik, S. K., Bose, P., and Pradhan, S. K. (2003). Microstructural characterization and phase transformation kinetics of ball-milled prepared nanocrystalline Zn₂TiO₄ by rietveld method. *Materials Chemistry and Physics*, 82, 837-847.
- Mills, A., and Hunte, A. J. (1997). An overview of semiconductor photocatalysis. *Journal of Photochemistry and Photobiology A Chemistry*, 108 (1), 1-35.

- Mohammadi, M., Fray, D., and Mohammadi, A. (2008). Sol-gel nanostructured titanium dioxide: Controlling the crystal structure, crystallite size, phase transformation, packing and ordering. *Microporous and Mesoporous Materials*, 112, 392-402.
- Moore, A., Vira, A., and Fogel, S. (1989). Biodegradation of trans-1,2-dichloroethylene by methane-utilizing bacteria in an aquifer simulator. *Environmental Science and Technology*, 23 (4), 403-406.
- Nakata, K., and Fujishima, A. (2012). TiO₂ photocatalysis: Design and applications. *Journal of Photochemistry and Photobiology C: Photochemistry Reviews*, 13 (3), 169-189.
- Nakata, K., Ochiai, T., Murakami, T., and Fujishima, A. (2012). Photoenergy conversion with TiO₂ photocatalysis: New materials and recent applications. *Electrochimica Acta*, 84, 103-111.
- Namratha, K., and Byrappa, K. (2012). Novel solution routes of synthesis of metal oxide and hybrid metal oxide nanocrystals. *Progress in Crystal Growth and Characterization of Materials*, 58, 14-42.
- Nguyen, T. B., Hwang, M. J., and Ryu, K. S. (2012). High adsorption capacity of V-doped TiO₂ for decolorization of methylene blue. *Applied Surface Science*, 278, 7299-7305.
- Nguyen-Phan, T. D., Song, M. B., Yun, H., Kim, E. J., Oh, E. S., and Shin, E. W. (2011). Characterization of vanadium-doped mesoporous titania and its adsorption of gaseous benzene. *Applied Surface Science*, 257, 2024-2031.
- Patil, K. C. (2008). Nano-Titania and Titanates. In K. C. Patil, *Chemistry of Nanocrystalline Oxide Materials: Combustion, Synthesis, Properties and Applications* (pp. 179-211).

- Patil, S., and Shinde, V. (1988). Biodegradation studies of aniline and nitrobenzene in aniline plant wastewater by gas chromatography. *Environmental Science and Technology*, 22 (10), 1160-1165.
- Pecharsky, V. K., and Zavalij, P. Y. (2008). *Fundamentals of Powder Diffraction and Structural Characterization of Materials* (2nd Edition ed.). New York: Springer.
- Pelaez, M., Nolan, N. T., Pillai, S. C., Seery, M. K., Falaars, P., Kontos, A. G., et al. (2012). A Review on the visible light active titanium dioxide photocatalysts for environmental applications. *Application Catalysis B: Environmental*, 125, 331-349.
- Pham, T. H., and Brindley, G. W. (1970). Methylene blue absorption by clay minerals. Determination of surface areas and cation exchange capacities. *Clays and Clay Minerals* , 18, 203-212.
- Pierre, A. C. (1998). *Introduction to Sol-Gel Processing*. USA: Kluwer Academic Publishers.
- Po, H. N., and Senozan, N. M. (2001). The Henderson-Hasselbalch Equation: Its History and Limitations. *Journal of Chemical Education*, 78, 1499.
- Rahaman, M. N. (2007). *Ceramic Processing*. Boca Raton, FL, USA: Taylor and Francis Group.
- Raj, K. J. A., Viswanathan, B. (2009). Effect of surface area, pore volume and particle size of P25 titania on the phase transformation on anatase to rutile. *Indian Journal of Chemistry*, 48A, 1378-1382.
- Ramaswamy, V., Jagtap, N., Vijayanand, S., Bhange, D., and Awati, P. (2008). Photocatalytic decomposition of methylene blue on nanocrystalline titania prepared by different methods. *Materials Research Bulletin*, 43, 1145-1152.

- Rehman, S., Ullah, R., Butt, A. M., and Gohar, N. D. (2009). Strategies of making TiO₂ and ZnO visible light active. *Journal of Hazardous Materials*, 170, 560-569.
- Reidy, D. J., Holmes, M. D., and Morris, M. A. (2006). The critical size mechanism for the anatase to rutile transformation in TiO₂ and doped-TiO₂. *Journal of European Ceramic Society*, 26 (9), 1527-1534.
- Rouquerol, F., Rouquerol, J., Sing, K. S., Llewellyn, P., and Maurin, G. (2014). *Adsorption by Powders and Porous Solids: Principles, Methodology and Applications*. San Diego: Academic Press.
- Salah, N., Habib, S. S., Khan, Z. H., Memic, A., Azam, A., Alarfaj, E., et al. (2011). High-energy ball milling technique for ZnO nanoparticles as antibacterial material. *International Journal of Nanomedicine*, 6, 863-869.
- Seabra, M. P., Miranda Salvado, I. M., and Labrincha, J. A. (2011). Pure and (zinc or iron) doped titania powders prepared by sol-gel and used as photocatalyst. *Ceramics International*, 37, 3317-3322.
- Shannon. (2012). *PaveMaintenance*. Retrieved December 15, 2013, from <http://pavemaintenance.wikispaces.com/TiO2+Photocatalys+-+Shannon>
- Shannon, R. D. (1976). Revised effective ionic radii and systematic studies of interatomic distances in halides and chalcogenides. *Acta Crystallographic Section A Crystal Physics, Diffraction, Theoretical and General Crystallography*, 32, 751-767.
- Shannon, R. D., and Prewitt, C. T. (1969). Effective ionic radii in oxides and fluorides. *Acta Crystallographia B*, 25, 797-858.
- Sivula, K., Formal, F. L., and Gratzel, M. (2009). WO₃-Fe₂O₃ Photoanodes for water splitting: A host scaffold, guest absorber approach. *Chemical Materials*, 21 (13), 2862-2867.

- Slokar, Y., and Le Marechal, A. (1998). Methods of decoloration of textile wastewaters. *Dyes and Pigments*, 37, 335-356.
- Stengl, V., Bakardjieva, S., and Murafa, N. (2009). Preparation and photocatalytic activity of rare earth doped TiO₂ nanoparticles. *Materials Chemistry and Physics*, 114, 217-226.
- Stengl, V., Houskova, V., Bakardjieva, S., and Murafa, N. (2009). Photocatalytic activity of boron-modified titania under UV and visible-light illumination. *Applied Materials and Interfaces*, 2 (2), 575-580.
- Su, C., Hong, B.-Y., and Tseng, C.-M. (2004). Sol-gel preparation and photocatalysis of titanium dioxide. *Catalysis Today*, 96 (5), 119-126.
- Suresh, C., Biju, V., Mukundan, P., and Warriar, K. (1998). Anatase to rutile transformation in sol-gel titania by modification of precursors. *Polyhedron*, 17 (18), 3131-3135.
- Suryanarayana, C. (2001). Mechanical alloying and milling. *Progress in Materials Science*, 46 (1-2), 1-184.
- Teh, C. M., and Mohamed, A. R. (2011). Roles of titanium dioxide and ion-doped titanium dioxide on photocatalytic degradation of organic pollutants (phenolic compounds and dyes) in aqueous solutions: A review. *Journal of Alloys and Compounds*, 509, 1648-1660.
- Tokmakci, T. (2013). *Preparation of boron-zirconium co-doped photocatalytic titanium dioxide powder*. MS Thesis, Middle East Technical University, Department of Metallurgical and Materials Engineering, Ankara, Turkey
- Tokmakci, T., Ozturk, A., and Park, J. (2013). Boron and zirconium co-doped TiO₂ powders prepared through mechanical ball milling. *Ceramics International*, 39 (5), 5893-5899.

- Venz, P. A., Bartlett, J. R., Frost, R. L., and Woolfrey, J. L. (1998). Electrokinetic studies on titania hydrolysates derived from a chemically-modified titanium alkoxide. *Sol-Gel Processing of Advanced Materials* (pp. 47-54). Ohio: The American Ceramic Society.
- Venz, P. A., Bartlett, J. R., Frost, R. L., and Woolfrey, J. L. (1998). Crystallization of titania hydrolysates during peptisation. *Sol-Gel Processing of Advanced Materials* (pp. 35-46). Ohio: The American Ceramic Society.
- Vereb, G., Manczinger, L., Bozso, G., Sienkiewicz, A., Forro, L., Mogyorosi, K., et al. (2013). Comparison of the photocatalytic efficiencies of bare and doped rutile and anatase TiO₂ photocatalysts under visible light for phenol degradation and E.coli inactivation. *Applied Catalysis B: Environmental*, 129, 566-574.
- Vorontsov, A., Altyinnikov, A., Savinov, E., and Kurkin, E. (2001). Correlation of TiO₂ photocatalytic activity and diffuse reflectance spectra. *Journal of Photochemistry and Photobiology A; Chemistry*, 144, 193-196.
- Wang, C. C., and Ying, Y. J. (1999). Sol-gel synthesis and hydrothermal processing of anatase and rutile titania nanocrystals. *Chemical Materials*, 11 (11), 3113-3120.
- Wang, R., Hashimoto, K., Fujishima, A., Chikuni, M., Kojima, E., and Kitamura, A. (1997). Light-induced amphiphilic surfaces. *Nature*, 388, 431-432.
- Watson, S. S., Beydoun, D., Scott, J. A., and Amal, R. (2003). The effect of preparation method on the photoactivity of crystalline titanium dioxide particles. *Chemical Engineering Journal*, 95, 213-220.

- Weirich, T. E., Winterer, M., Seifried, S., Hahn, H., and Fuess, H. (2000). Rietveld analysis of electron diffraction data from nanocrystalline anatase TiO₂. *Ultramicroscopy*, 81, 263-270.
- Wikipedia. (2014, March 13). *Wikipedia The Free Encyclopedia*. Retrieved April 13, 2014, from http://en.wikipedia.org/wiki/Visible_light
- Woolfrey, J. L., and Bartlett, J. R. (1998). Processing colloidal powders, sols and gels. *Sol-Gel Processing of Advanced Materials* (pp. 3-20). Ohio: The American Ceramic Society.
- Wright, J. D., and Sommerdijk, A. J. (2001). *Sol-Gel Materials Chemistry and Applications*. London, Great Britain: Taylor and Francis Books Ltd.
- Wu, Y., Xing, M., Zhang, J., and Chen, F. (2010). Effective visible light-active boron and carbon modified TiO₂ photocatalyst for degradation of organic pollutant. *Applied Catalysis B: Environmental*, 97, 182-189.
- Xu, N., Shi, Z., Fan, Y., Dong, J., Shi, J., and Hu, M.-C. (1999). Effect of particle size of TiO₂ on photocatalytic degradation of methylene blue in aqueous suspensions. *Industrial and Engineering Chemistry Research*, 38, 373-379.
- Xue, X., Wang, Y., and Yang, H. (2013). Preparation and characterization of boron-doped titania nano-materials with antibacterial activity. *Applied Surface Science*, 264, 94-99.
- Yang, J., and Ferreira, J. M. (1998). On the titania phase transition by zirconia additive in a sol-gel derived powder. *Materials Research Bulletin*, 33 (3), 389-394.
- Yao, J., and Wang, C. (2010). Decolorization of methylene blue with TiO₂ sol via uv irradiation photocatalytic degradation. *International Journal of Photoenergy*, 1-6.

- Yoldas, B. E. (1986). Hydrolysis of titanium aioxide and effects of hydrolytic polycondensation parameters. *Journal of Materials Science*, 21, 1087-1092.
- Zaleska, A., Grabowska, E., Sobczak, J. W., Gazda, M., and Hupka, J. (2009). Photocatalytic activity of boron-modified TiO₂ under visible light: The effect of boron content, calcination temperature and TiO₂ matrix. *Applied Catalysis B: Environmental*, 89, 469-475.
- Zaleska, A., Sobczak, J. W., Grabowska, E., and Hupka, J. (2008). Preparation and photocatalytic activity of boron-modified TiO₂ under UV and visible light. *Applied Catalysis B: Environmental*, 78, 92-100.
- Zhang, H., and Banfield, J. F. (1998). Thermodynamic analysis of phase stability of nanocrystalline titania. *Journal of Material Chemistry*, 8, 2073-2076.
- Zhang, W., Yang, B., and Chen, J. (2012). Effects of calcination temperature on preparation of boron-doped TiO₂ by sol-gel method. *International Journal of Photoenergy*, 2012.
- Zhang, X., and Liu, Q. (2008). Visible-light induced degradation of formaldehyde over titania photocatalyst co-doped with nitrogen and nickel. *Applied Surface Science*, 254 (15), 4780-4785.
- Zhang, Z., Wang, C.-C., Zakaria, R., and Ying, J. Y. (1998). Role of particle size in nanocrystalline TiO₂-based photocatalysts. *Journal of Physical Chemistry B*, 102, 10871-10878.
- Zhao, J., and Yang, X. (2003). Photocatalytic oxidation for indoor air purification: a literature review. *Building and Environment*, 38 (5), 645-654.